Study of IR un-cooled micro-bolometer arrays based on thin films deposited by plasma

by

M.C. Mario Moreno Moreno

A thesis submitted in partial fulfillment of the requirements for the degree of

Doctor in Science with Specialty in Electronics

at

Instituto Nacional de Astrofísica, Óptica y Electrónica

Puebla, México

Supervised by:

Dr. Andrey Kosarev and Dr. Alfonso Torres

RESUMEN

La tecnología de micro-maquinado superficial para películas delgadas en conjunto con la tecnología de fabricación de circuitos integrados en silicio, han permitido un importante desarrollo de sistemas de visión nocturna de bajo costo basados en arreglos de detectores de radiación infrarroja. Entre los detectores empleados en esos sistemas, el bolómetro es uno de ellos.

Las aplicaciones de los sistemas infrarrojos están en continuo crecimiento, algunas de las más importantes son seguridad, lucha contra el fuego, biomedicina, mantenimiento preventivo y visión nocturna para automóviles entre otras. La tecnología infrarroja tiene un camino amplio que cubrir y todavía hay un importante campo de estudio de esta tecnología para satisfacer las necesidades de sistemas infrarojos de bajo costo y alto desempeño.

En la actualidad existen arreglos de micro-bolómetros comerciales grandes (640 x 380 píxeles), los cuales contienen diferentes materiales termo-sensores, como óxido de vanadio (VO_x), metales, semiconductores policristalinos y amorfos. Estos materiales presentan buenas características pero también presentan desventajas. Los metales son compatibles con la tecnología CMOS en silicio, sin embargo presentan un coeficiente de temperatura de resistencia (TCR) pequeño, el cual es el cambio de resistencia debido a la absorción de radiación IR. El VO_x es un material que tiene un TCR alto pero no es compatible con la tecnología CMOS en silicio.

Silicio amorfo es un material compatible con la tecnología de silicio, presenta un TCR alto, sin embargo tiene una alta resistencia, lo que produce incompatibilidad de impedancia con los circuitos de lectura. Así pues ninguno de los materiales utilizados como película termo-sensora es el óptimo.

En el trabajo previo realizado en el INAOE, se han utilizado películas de silicio germanio amorfo, como elemento termo-sensor en micro-bolometros, ya que presenta una energía de activación alta ($E_a = 0.34$ eV) y por consecuencia un valor de TCR alto.

Algunas de las características de desempeño de estos dispositivos son comparables con las de dispositivos comerciales, sin embargo también presentan algunas desventajas, las cuales son tiempo de respuesta grande, resistencia de celda alta y bajo yield al término del proceso de fabricación.

El trabajo realizado en la presente tesis tiene dos direcciones principales. La primera esta enfocada al estudio de celdas de micro-bolómetros para mejorar sus características de desempeño. La segunda está enfocada en el estudio de arreglos de micro-bolómetros.

Aleaciones de silicio-germanio-boro han sido estudiadas para incorporarlas como películas termo-sensoras en micro-bolómetros no enfriados para reducir la resistencia alta indeseable, la cual esta presente en micro-bolómetros con película intrínseca de silicio-germanio.

Una configuración tipo sándwich la cual emplea película intrínseca ha sido propuesta, para reducir la resistencia de la celda sin una reducción en otras características como lo es la energía de activación E_a y TCR.

Parte de este trabajo esta relacionado con el estudio, diseño fabricación y caracterización de arreglos de micro-bolómetros y el estudio de características específicas de arreglos como es crosstalk y obtención de imágenes en una dimensión.

ABSTRACT

Surface micro-machining technology for thin films in conjunction with the silicon IC fabrication technology have allowed an important development on low cost and reliable night vision systems based on thermal detectors arrays. Among the thermal detectors of choice for these systems, the bolometer is one of them.

The applications of IR systems are in continuous growth, some of the most important applications are security, fire fighting, biomedical, preventive maintenance, and driving night vision. IR technology has a wide road to cover and still there is an important field of study in this technology in order to satisfy the need of low cost and high performance IR imaging systems.

In the present time there are commercially available large micro-bolometer arrays (640 x 380 pixels), which contain different thermo-sensing materials, such as vanadium oxide (VOx), metals, and amorphous and polycrystalline semiconductors.

Those materials present good characteristics but also have some disadvantages. Metals are compatible with the standard IC fabrication technology, but have low TCR values. VOx has a high TCR but it is not a standard material in IC technology. Amorphous silicon (a-Si:H) has a high TCR value and is compatible with the silicon technology, however possesses a very high resistance which results in a mismatch with the input impedance of the CMOS read-out circuits. As a consequence none of the commercially arrays contain an optimum pixel with an optimum thermo-sensing material.

In previous works performed at INAOE, amorphous silicon-germanium films obtained by PECVD were employed in the fabrication of un-cooled micro-bolometers, providing high activation energy (E_a = 0.34 eV) and consequently a high value of TCR.

Some of the performance characteristics of these devices are comparable with those of the commercially available micro-bolometers, however they have some drawbacks, which are a slow thermal response time, a still high cell resistance, and a low yield at the end of the fabrication process.

The work performed in the present thesis has two main directions. The first is focused on the study of the micro-bolometer cells in order to improve their performance characteristics. The second direction is focused in the study of micro-bolometer arrays.

The study of the micro-bolometer cells consist mainly in the study of the layout and process flow of the previously fabricated micro-bolometers (labeled planar structure), and make some changes in their structures in order to improve their yield at the end of the fabrication process, and also improve the performance characteristics, such as fast response time and moderated cell resistance.

Amorphous silicon–germanium–boron alloys are also studied for the incorporation of them as thermo-sensing film in un-cooled micro-bolometers, in order to reduce the undesirable high cell resistance, which is presented in the intrinsic amorphous silicon –germanium films.

A sandwich configuration micro-bolometer employing an intrinsic thermo-sensing film is proposed, in order to reduce the cell resistance, without a reduction in other characteristics of the device, such as the activation energy, E_a and TCR.

Part of the thesis work is related to the study, design, fabrication and characterization of micro-bolometer arrays, and the study of specific characteristics of arrays, such as the obtaining of one dimensional images, and crosstalk.

AGRADECIMIENTOS

Durante el tiempo que trabaje en la tesis de doctorado recibí ayuda de muchas personas e instituciones a las que quiero agradecer:

- ☺ Mis padres Mario y Cristina† por todo su amor y apoyo durante mi vida.

- ☺ Mi esposa Rosayleci por su comprensión, amor y paciencia.

- ☺ Mis hermanos Nancy, Jesús y Michelle y mi sobriono Luigi por sus animos y estar siempre conmigo.

- ☺ Mis suegros David Armas y Alfonsa Rodríguez y mi cuñado David Armas, por su apoyo.

- ☺ Mis asesores de tesis el Dr. Andrey Kosarev y el Dr. Alfonso Torres por lo que me han enseñado durante estos años de trabajo.

- ☺ Los técnicos del laboratorio de micro-electrónica: Pablo Alarcón, Ignacio Juárez, Netzahualcoyotl Carlos, Mauro Landa, Adrian Izcoyotl, Rosa Técuatl y Leticia Tecuapetla.

- ☺ Los doctores del grupo de microelectrónica del INAOE: Carlos Zuñiga, Javier Wade, Edmundo Gutierrez, Wilfrido Calleja, por sus enseñanzas.

- ☺ Mis amigos y compañeros del INAOE, Roberto Ambrosio, Karim Monfil, Maria de la Luz, Alfredo Morales, Alberto Luna, Liborio Sanchez.

☺ Al Instituto Nacional de Astrofísica Optica y Electrónica (INAOE) y a su valioso personal.

☺ Al Consejo Nacional de Ciencia y Tecnología (CONACYT) por ser una gran institución y por la beca otorgada durante mis estudios de doctorado No. 166011.

DEDICADA A MI FAMILIA:

MI ESPOSA ROSAYLECI,

MIS PADRES MARIO Y CRISTINA✝,

MIS HERMANOS NANCY, MICHELLE, JESUS Y MI SOBRINO LUIGI

MIS SUEGROS DAVID Y ALFONSA

MI CUÑANDO DAVID Y MI SOBRINA FERNANDA

CONTENT

LIST OF ACRONYMS

1-D	One dimensional
2-D	Two dimensional
IR	Infrared
MWIR	Medium Wavelength Infrared
LWIR	Long Wavelength Infrared
CMOS	Complementary Metal Oxide Semiconductor Technology
Si	Silicon
Ge	Germanium
In	Indium
Al	Aluminum
Ti	Titanium
SiGe	Silicon Germanium
GaAs	Gallium Arsenide
InSb	Indium Antimony
PbSnTe	Lead Tin Telluride
HgCdTe	Mercury Cadmium Telluride
LITa	Lithium Tantalite
BaSrTiO	Barium Strontium Titanate
VO_x	Vanadium Oxide
LF	Low Frequency
PECVD	Plasma Enhanced Chemical Vapor Deposition
CVD	Chemical Vapor Deposition
RF	Radio Frequency
NETD	Noise Equivalent Temperature Difference
IRFPA	Infrared Focal Plane Array
IC	Integrated Circuit
ROIC	Read Out Integrated Circuit
TCR	Thermal Coefficient of Resistance

DC	Direct Current
LETI/CEA	Laboratorie d'Electronique de Technologie de l'Information
MEMS	Micro Electro Mechanical Systems
SEM	Scanning Electron Microscope
RIE	Reactive Ion Etching
FTIR	Fourier Transform Infrared Spectroscopy
SIMS	Secondary Ion Mass Spectroscopy
NSD	Noise Spectral Density
ZnSe	Zinc Selenide
DIP	Dual Inline Package

LIST OF SYMBOLS

Symbol	Name	Units
α	Temperature coefficient of resistance	K^{-1}
λ	Wavelength	μm
Δf	Frequency bandwidth	Hz
R_U	Voltage responsivity	VW^{-1}
R_I	Current responsivity	AW^{-1}
ρ	Electrical resistivity	Ω cm
σ	Electrical conductivity	Ω^{-1} cm^{-1}
σ_0	Prefactor of the films	Ω^{-1} cm^{-1}
σ_{RT}	Room temperature conductivity	Ω^{-1} cm^{-1}
τ_{th}	Thermal response time	s
A_{cell}	Micro-bolometer area	μm^2
C_{th}	Thermal capacitance	JK^{-1}
G_{th}	Thermal conductance	WK^{-1}
R_{th}	Thermal resistance	KW^{-1}
T	Temperature	K
T_s	Substrate temperature	K
T_{cell}	micro-bolometer temperature	K
f	Frequency	Hz
D*	Detectivity	$cmHz^{1/2}W^{-1}$
ΔI	Increment in current	A
ΔU	Increment in voltage	V
A_{pad}	Metal pad area	μm^2
A_A	Array area	μm^2
E_a	Activation Energy	eV
Q	Gas flow rates	sccm
U	Bias voltage	V
I	Current	A

L	length of active area of a micro-bolometer	μm
W	width of active area of a micro-bolometer	μm
K	Wave number	cm^{-1}
I_0	Intensity of the IR source	Wcm^{-2}
$P_{incident}$	IR incident power in the device surface	W
I_{noise}	Noise spectral density	$AHz^{-1/2}$
V_N	Total noise	V
V_j	Johnson noise	V
V_{TF}	Temperature fluctuation noise	V
V_{BF}	Background fluctuation noise	V
$V_{1/f}$	Low frequency noise	V
R_{cell}	Cell resistance	Ω
C_{cable}	Cable capacitance	pF
I_{Dark}	Dark current	A
I_{IR}	Infrared current	A
$\overline{R}$	mean responsivity	VW^{-1} or AW^{-1}
R_L	Load resistor	Ω
τ_{elec}	Electrical time	s
P	Power	W

CHAPTER 1. INTRODUCTION

1.1 Historical overview on IR technology

The first notion of IR detection date from thousands of years ago when man was capable of identified the place were the extinguished fire was located by placing his hand palms at some distance over the warm black carbon.

However the existence of IR radiation was discovered until 1800 by Sir F. W. Herschel with his famous experiment in which he made pass sunlight through a glass prism and it was decomposed into the visible colors of the spectrum. He measured the amount of heat in each color of the spectrum with a thermometer and found that the heat increased from the blue color to the red color and moreover the heat was higher in the part not visible of the spectrum beyond the red color, this part of the spectrum is called infrared from the Latin word “infra” which means below.

The development of IR detectors started with the construction of thermal detectors. In 1821 Thomas J. Seebeck discovered the thermoelectric effect, which is the direct conversion from a temperature difference into voltage, this is the basics for the thermocouple, in 1829 Leopoldo Nobili constructed the first thermopile with the connection in series of several thermocouples and in 1878 Samuel P. Langley constructed the first resistive bolometer made of platinum stripes.

Modern development on IR detectors started at the end of 1920s with the comprehension of photoemission and the construction of the first photocathode, which was used in the first military night vision image intensifier, that device used the silver-oxygen-caesium compound (Ag-O-Cs) since it shows a response in the near IR range; such systems had a low quantum efficiency, there was no internal amplification of the photoemitted electrons and required a near IR source to illuminate the target [1.1].

The development of intensifiers continued and, at the beginning of 1960s the limitations were overcome with the second and third generation of intensifiers with the discovery of the gallium arsenide (GaAs) compound and its incorporation on

photocathodes, which have a spectral response around 1.1 μm [1.2], those devices did not require active illumination sources but they needed the moon light reflected from targets, in fact the main disadvantage of those devices was the incapacity to work well on moonless nights.

In the same decade there were significant advances in photon detectors with the discovery of narrow bandgap semiconductors, one of the first used materials was the indium antimony (InSb) a III-V binary compound, also ternary compounds were introduced such as lead tin telluride ($Pb_{1-x}Sn_xTe$) a IV-VI compound, and mercury cadmium telluride ($Hg_{1-x}Cd_xTe$) a II-VI compound [1.3]. Those materials provided a degree of freedom in the design of infrared detectors without precedent. For first time it was possible to tailor the bandgap and consequently the spectral response of a material for a specific application, in addition narrow gap semiconductors show high optical absorption coefficient and high electron mobility.

During the last 40 years ternary materials have been used in the development of photovoltaic and photoconductive detectors. The HgCdTe alloy has been the most important material used for middle and long wavelength IR detection. The main reason is that this alloy presents an extremely flexibility, its gap can be tailored (from 0.2 eV to 1.5 eV) in order to optimize the detection at any region of the whole IR spectrum without a significant change in its lattice parameter (just the 0.2%) [1.4].

In order to suppress thermal excitation of free carriers at ambient temperature and thus have low dark current, photon detectors need to be cooled at cryogenic temperatures, for example the $Hg_{0.8}Cd_{0.2}Te$ photon detectors operating in the 8-12 μm spectral range need to be cooled to 77 K, the liquid nitrogen temperature.

Those devices have been used in the development of scanner linear arrays with a high performance with very low noise. However photon detectors need additional expensive equipment in order to work at low temperatures and therefore, are not convenient for portable and low cost applications.

All of that have motivated the development of IR detectors that could provide images arising from thermal emission of terrestrial objects like people, animals and vehicles, with the capability to work at ambient temperature and consequently

without the necessity of cryogenic cooler equipments. Those low-cost devices are called un-cooled thermal detectors. There are three main categories of thermal detectors, thermoelectric detectors, pyroelectric / ferroelectric detectors and resistive bolometers.

The development of thermal detectors started in the 1980s, mainly under classified military contracts in United States sponsored by the US Army Night Vision Laboratories and the Defence Advanced Projects Agency (DARPA) [1.2]. In 1983 Honeywell Inc. started with the development of un-cooled thermal detectors using silicon micromachining techniques, they based their efforts in the production of monolithic thin film bolometer arrays based on Vanadium Oxide (VO_x), and in 1989 demonstrated an array of 64 x 128 pixels. At the same time a division of Texas Instruments Inc. that later was acquired by Raytheon developed hybrid pyroelectric and ferroelectric bolometer arrays. The work became unclassified in 1992 revealing their outstanding results in the field, however there was no divulgation in their manufacturing technologies, even at the present.

Currently amorphous silicon a-Si:H is employed also as thermo sensing film in micro-bolometers [1.2, 1.3], 640x480 arrays inside IR Cameras are commercially available in United States and several countries have developed their own un-cooled thermal imaging arrays, including France [1.3]. The state of the art in thermal imaging arrays will be discussed later, in section 2.7.

1.2 Background and Justification

As it was discussed in the previous section, there exists an important development in IR imaging systems based on un-cooled thermal detectors arrays. Even at the present there are commercially available large micro-bolometer arrays, none of them can be considered to contain an optimum pixel fabricated with the best materials.

The civilian applications of IR systems are in continuous growth and every day appear new ones, some of the most important applications are biomedical, fire fighting, security, industrial maintenance and driving night vision.

IR technology has a wide road to cover and still there is an important field of study in this technology in order to satisfy the need of low cost, high performance and portable IR imaging systems.

The increasing use of thermal detectors in IR imaging systems is not a coincidence, there are several factors that have influenced the development of them. Thermal detectors have several advantages over photon detectors, the most important are listed below:

- Photons detectors have a principal limitation in the wavelength at which will respond, dictated by the energy band gap, E_g. Thus, in order to respond to larges wavelengths, the E_g must be very small. However a small E_g implies a large number of carriers thermally generated, which is traduced in large noise currents.
- In order to suppress noise currents in photon detectors, cryogenic refrigerators at 77 K or 4 K are employed, which increase significantly the cost of the thermal imaging devices.
- Thermal detectors have no limitations on E_g, since their operation is based on the change in some property due to the absorption of IR or any radiation.
- Thermal detectors can work at room temperature, therefore do not need any cryogenic equipment, which reduce their cost significantly and make it possible to build with them compact imaging systems.

A bolometer is one of many different kinds of thermal detectors. In a micro-bolometer, the absorption of incident IR radiation increases the temperature of its thermo-sensing material. The change in temperature causes a change in its electrical resistance.

The main requirements for the thermo-sensing materials used in micro-bolometers are the following: a high value of the temperature coefficient of resistance, TCR (α), moderate resistivity, low noise and compatibility with standard silicon IC fabrication processes.

Several materials have been used as thermo-sensing elements in micro-bolometers; the most employed are VO_x, amorphous and polycrystalline semiconductors, and some metals [1.5-1.11]. Those materials have shown good characteristics but also some disadvantages. VO_x presents a relatively high value of TCR ($\alpha = 0.021\ K^{-1}$), but it is not a standard material in IC technology. Metals as titanium, Ti, are compatible with the standard IC fabrication technology, present low resistance but have low values of TCR.

Hydrogenated intrinsic amorphous silicon (a-Si:H) prepared by PECVD is a material commonly used in micro-bolometers as thermo-sensing film, for room temperature operation. It is compatible with the silicon IC technology, presents a high value of TCR ($\alpha \approx 0.039\ K^{-1}$) when is prepared by PECVD [1.8-1.9], however it also presents a high undesirable resistivity, which often cause a mismatch with the input impedance of the read-out circuits.

In order to reduce the a-Si:H high resistance, boron doping has been employed. The B doped a-Si:H films present a significant reduction in its resistivity, however a reduction in TCR is obtained also.

In the previous work performed at INAOE [1.12], amorphous silicon-germanium films, a-Si_xGe_y:H, deposited by PECVD have been employed as thermo-sensing films in micro-bolometers; since a-Si_xGe_y:H presents a high value of TCR ($\alpha = 0.043\ K^{-1}$) and improved, but still high resistivity, when is compared with a-Si:H.

At this stage, the design of the micro-bolometer cells has been not optimized, resulting in low yield devices at the end of the fabrication process, without optimal performance characteristics; such as fast thermal response time, high responsivity, high detectivity and low noise.

In order to initiate a development of micro-bolometer arrays at INAOE, it is necessary first, to improve the yield and the performance characteristics of those devices. For that propose, two approximations are followed:

- A study of the cell design and process flow of the micro-bolometers, taking into account the key factors during the fabrication process, that influences directly on the yield and performance characteristics. With the knowledge obtained, modifications will be made in the cell design.
- A study of the a-Si_xGe_y:H the thermo-sensing film in order to reduce its high resistivity, specifically on studying of the effect of boron incorporation during the deposition of the a-Si_xGe_y:H film, and its influence in the micro-bolometer performance characteristics.

With the cells optimized, the design and fabrication of micro-bolometer arrays will be performed. In order to characterize the arrays an experimental read-out circuit must be designed. In the next section the objectives of the thesis work are presented and the tasks that must to be performed in order of achieve those objectives.

1.3 Objectives and tasks

The main objective of the present thesis work is the study of fabrication of un-cooled micro-bolometers, their performance and concrete characteristics; the development of fabrication technology and new device configurations with emphasis on arrays.

In order to achieve the objective it is necessary to perform the following tasks:

- To study the work previously realized at INAOE on micro-bolometers [3.1 – 3.2] based on thin films deposited by plasma, for the selection of the most

suitable micro-bolometer cell (among several designed) for the development of arrays. The cell selection must be done in terms of its performance characteristics and yield at the end of the fabrication process.

- To perform an analysis of the micro-bolometers previously fabricated at INAOE, and make the proper changes on it, for improving their yield and performance characteristics.
- To study the effect of boron incorporation during the deposition of the a-Si_xGe_y:H film, and its influence in the micro-bolometer performance characteristics.
- To design the lay-out and the process flow of the micro-bolometer arrays, taking into account the previous results and the minimum dimensions allowed by the silicon CMOS technology existing in the micro-electronics laboratory of INAOE.
- To fabricate the arrays containing the modified micro-bolometer cells, in the laboratory of micro-electronics of INAOE.
- To study the performance characteristics of the modified single cell micro-bolometers and of the micro-bolometer arrays.
- To study the key issues in the fabrication process of arrays in order to increase the yield at the end of the fabrication process.

1.4 Thesis organization

The organization of the present work is as follows. In chapter 2 the analysis of literature concerned with infrared technology and the state-of-the-art of micro-bolometer arrays is presented. The different infrared detectors are described with the bolometer as one of them. Figures of merit, noise and requirements for high performance characteristics of single cell micro-bolometers and micro-bolometer arrays are discussed.

In chapter 3 the methodological part followed in the thesis is described. A study of micro-bolometers based on a-Si_xGe_y:H films developed at INAOE is

performed, improvements and variations proposed in those devices are studied also. The design of micro-bolometer arrays is described and the methodology for their characterization is discussed.

Chapter 4 describes the experimental results obtained from the fabrication process and the characterization of the micro-bolometers as single cells and micro-bolometer arrays.

Discussion of the results obtained from the fabrication process and characterization of the micro-bolometer arrays are presented in chapter 5. Finally, chapter 6 presents the conclusions of this thesis work.

1.5 References of chapter 1

[1.1] Paul Wan Kruse, "Uncooled focal plane arrays", Proceedings of the Ninth IEEE International Symposium on Applications of Ferroelectrics, pp. 643-646, 1994.

[1.2] R. A. Wood, C. J. Han, and P. W. Kruse, "Integrated Uncooled Infrared Detector Imaging Arrays", Solid-State Sensor and Actuator Workshop, 1992, 5th Technical Digest., IEEE, pp. 132 -135, 1992.

[1.3] Antoni Rogalski, "Heterostructure infrared photovoltaitic detectors", Infrared physics & technology, Vol. 41, pp. 213 – 238, 2000.

[1.4] Joezf Pitrowski, Antoni Rogalski, "New generation of infrared photodetectors", Sensors and actuators, A.67, pp.146-152, 1998.

[1.5] B. Cole, R. Horning, B. Johnson, K. Nguyen, P. W. Kruse and M. C. Foote, "High Performance Infrared Detector Arrays using Thin Film Microstructures", Proceedings of the Ninth IEEE International Symposium on Applications of Ferroelectrics, .ISAF '94., pp. 653-656, 1994.

[1.6] B. E. Cole, R.E. Higashi, and R. A Wood, "Monolithic Arrays of Micromachined Pixels for Infrared Applications", International Electron Devices Meeting, 1998. IEDM '98 Technical Digest., pp.459 – 462, 1998.

[1.7] B. E. Cole, R.E. Higashi, and R. A Wood, “Micromachined Pixel Arrays Integrated with CMOS for Infrared Applications”, 2000 IEEE/LEOS International Conference on Optical MEMS, pp. 63-64, 2000.

[1.8] C. Trouilleau, A. crastes, J.L. Tissot, J.P. Chatard, “Low cost amorphous silicon based 160 x 120 uncooled microbolometers 2D arrays for high volume applications”, Infrared Technology and Applications XXIX. Edited by Andresen, Bjorn F.; Fulop, Gabor F. Proceedings of the SPIE, Volume 5074, pp. 511-517, 2003.

[1.9] Bruno Fieque, Arnaud Crastes, Jean-Luc Tissot, Jean Pierre Chatard, Sebastián Tinnes, “320x240 uncooled microbolometer 2D array for radiometric and process control applications”, Detectors and Associated Signal Processing. Edited by Chatard, Jean-Pierre; Dennis, Peter N. J. Proceedings of the SPIE, Volume 5251, pp. 114-120, 2004).

[1.10] E. Iborra, J. Sangrador, M. Clement, J. Pierre, “Ge:Si:O evaporated alloys as thermosensitive layer for large area bolometers”, Thin solid films, Vo. 337, pp. 253-256, 1999.

[1.11] Mukti M. Rana, Donald P. Butler, “Radio Frequency $Si_{1-x}Gex$ and $Si_{1-x}Ge_xO_y$ thin films for uncooled infrared detectors” Thin solid films, Vol. 514, pp. 355 -360, 2006.

[1.12] R. Ambrosio “Research on fabrication process for un-cooled microbolometers based on plasma deposited films” PhD. Thesis, INAOE, 2005.

CHAPTER 2. ANALYSIS OF LITERATURE

2.1 Introduction

This chapter presents an analysis of infrared (IR) radiation technology available in literature paying special interest to un-cooled micro-bolometers and un-cooled micro-bolometer arrays. The chapter begins with a brief overview of infrared technology, followed with a revision of the different types of IR detectors which are divided in two main groups: photon detectors and thermal detectors where is included the bolometer.

The requirements for high performance micro-bolometers, figures of merit, performance characteristics and noise in micro-bolometers are presented also. Finally a discussion on micro-bolometer arrays, read-out circuits for arrays and the state of the art in this kind of devices is presented.

2.2 Infrared radiation and detectors

This section presents a short description in basic concepts of IR technology and the different types of IR detectors available with advantages and disadvantages, finally the applications of them are described.

2.2.1 Infrared detection background

Figure 2.1 shows the electromagnetic spectrum (based on [2.1]), the infrared region is located between the visible region, beyond the red, and the microwave region. IR region has been divided in four regions: near IR (0.77 – 1.5 μm), medium IR (1.5 – 6 μm), far IR (6 – 40 μm) and extreme IR (40 – 1000 μm). All objects emit electromagnetic radiation in the IR region, except those which are at absolute zero. The wavelength of radiation is a function of the temperature of the object.

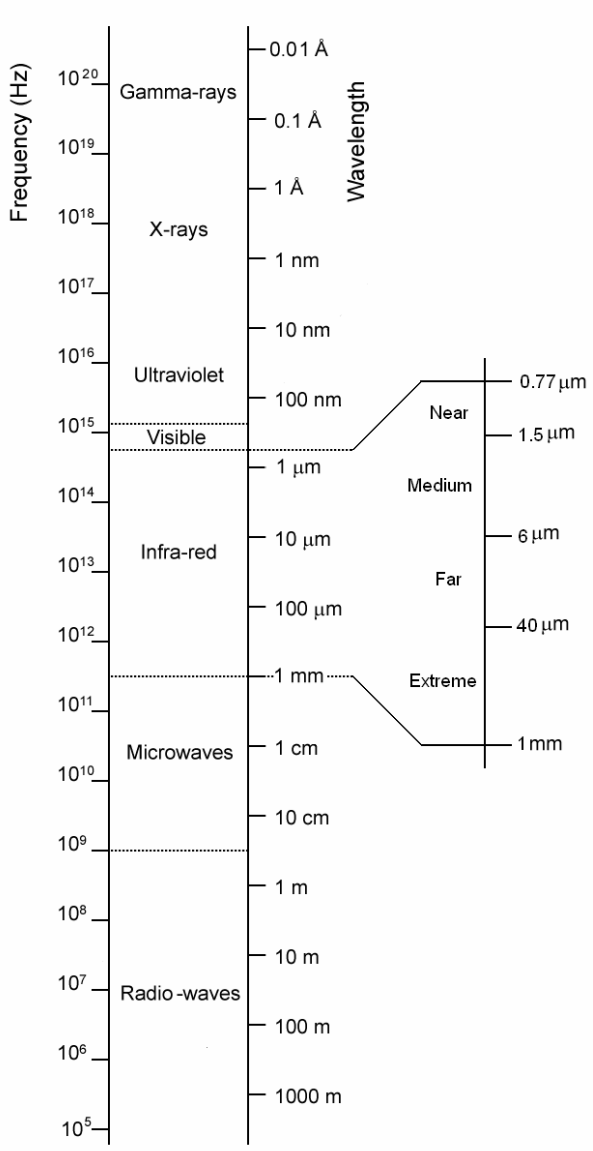

Figure 2.1. Electromagnetic spectrum.

Figure 2.2 shows the spectral dependence of radiation with temperature [2.2]. Objects with high temperatures have the peak of emission at short wavelengths while objects with low temperatures have the peak of emission at longer wavelengths. For example the sun has a temperature around 5900 K and its peak wavelength of emission is 0.53 μm, however it emits energy from the ultraviolet region to the far IR region.

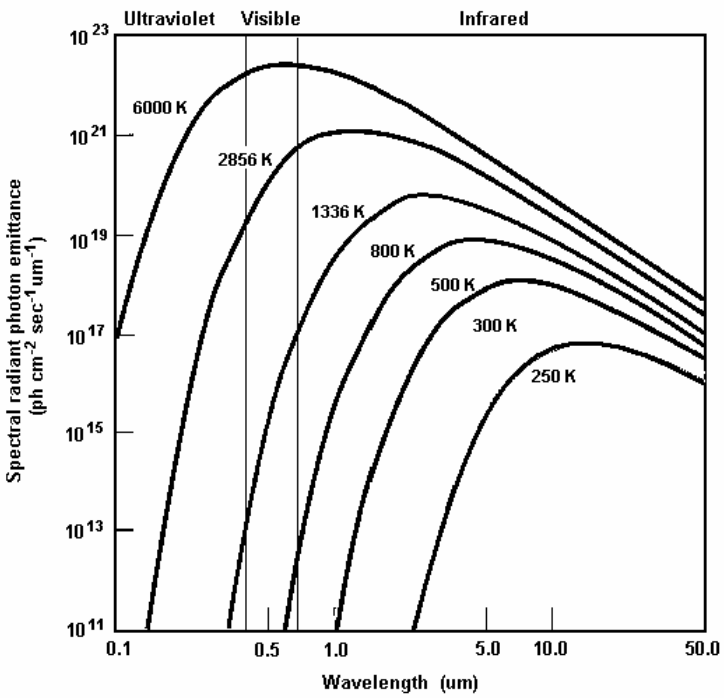

Figure 2.2. Spectral dependence of radiation.

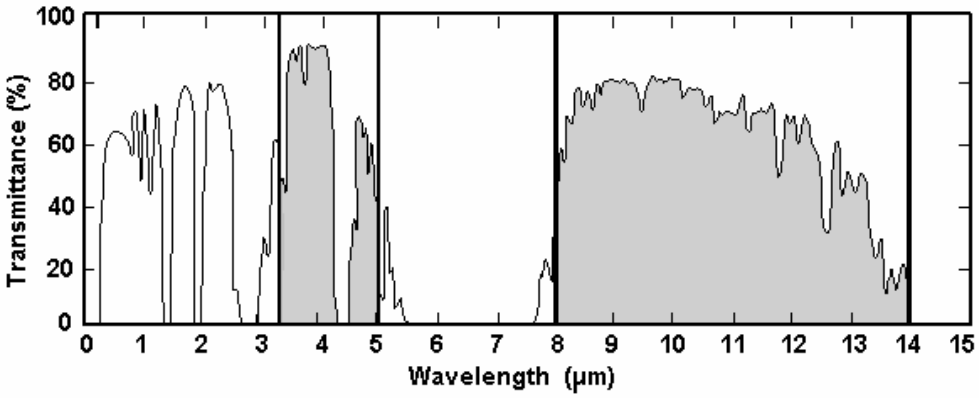

Figure 2.3. Atmospheric transmission.

IR radiation is absorbed or scattered while it propagates in the atmosphere by water vapor or CO_2. Figure 2.3 shows the atmospheric transmission characteristics from 0 to 15 μm. There are two principal IR transmission windows: The medium wavelength IR (MWIR) band, which is in the range 3.3 -5 μm, and the long wavelength IR (LWIR) band, which is the range 8 – 14 μm. The transmission

windows are selected based on the nature of the expected object to be detected. Objects at room temperature (300 K) emit in the range 3 – 14 μm, with the peak wavelength of emission at 10 μm.

2.2.2 Photon detectors for IR radiation

There are two fundamental methods for detecting IR radiation, photon detectors and thermal detectors [2.3-2.4]. Those detectors are made from semiconductor materials, and convert the IR absorbed radiation into an electrical signal which is measurable by a change of some physical property. The photon detectors can work in photoconductive or photo voltaic mode.

In photoconductive detectors the electrons can make a transition from the valence band to the conduction band in the material by the absorption of photons, resulting in a change in the detector conductivity. In order to make possible the transition, the energy of the photons must to be larger than the energy of the forbidden band gap, E_g. However there is a limit on the wavelength at which the detector will respond, dictated by Equation 2.1.

$$\lambda = hc = \frac{1.24}{E_g} \qquad (2.1)$$

Where λ is the photon wavelength, h is Planck constant, and c is the speed light. In order to increase the wavelength at which the device will respond, the energy of the forbidden band gap can be tailored by adding impurity atoms (extrinsic detectors) or fabricating complex alloys; however those devices must be cooled at cryogenic temperatures (77 – 4K) in order to avoid the thermal generation of carriers, which is the main source of noise current. Photovoltaic detectors (commonly called photo diodes) are p-n junctions, in which an absorption of a photon creates a electron – hole pair across the junction, in these devices a current is generated without an external bias.

Table 2.1 Comparison of photon IR detectors [2.4-2.5].

Photon detectors	**Materials**	**Advantages**	**Disadvantages**
Intrinsic	IV-VI: PbS, PbSe, PbSnTe	Easy to prepare, stable materials	Very high thermal expansion coefficient
	II-VI: HgCdTe	Band gap tailoring, well developed theory, multicolor detector	Non-uniformity over large area, High cost in growth and processing
	III-V: InGaAs, InAs, InAsSb	Possible monolithic integration, advanced technology	Heteroepitaxy with large lattice mismatch
Extrinsic	Si:Ga, Si:As, Ge:Cu, Ge:Hg	Very long wavelength operation	High thermal generation, extremely low temperature operation
Free carriers	PtSi, Pt_2Si, IrSi	Low cost, high yield, large 2.D arrays	Low quantum efficiency, low temperature operation
Quantum wells	Type I: GaAs/AlGaAs, InGaAs/AlGaAs	Good uniformity over large area, multicolor detector	High thermal generation, complicated design and growth
	Type II: InAs/InGaSb, InAs/InAsSb	Easy wavelength control	Complicated design and growth
Quantum dots	InAs/GAAs, InGaAs/InGaP	Low thermal generation	Complicated design and growth

At the present there are several kinds of photon detectors fabricated with different materials. Table 2.1 shows the advantages and disadvantages of these devices [2.4-2.5].

2.2.3 Thermal detectors for IR radiation

The basic operation of thermal detectors is a two step process:

A) The absorption of IR radiation raises the temperature of the detector sensing layer.
B) The increment in temperature causes a change in some temperature-dependent parameter of the device, such as resistance; that change is measured by an external circuit.

A thermal detector consists of three main parts:

A) IR absorber.

B) Thermo-sensing element.

C) Element for providing thermo isolation.

Depending on its operation, thermal detectors can be divided in three groups: thermoelectric detector (thermopile or thermocouple), pyroelectric / ferroelectric detectors and bolometers.

A thermo-electric detector is formed by the junction of two dissimilar materials (metals or semiconductors). If we consider two junctions A-B (where A and B are dissimilar materials), connected by one point (B-B) and the temperature in the junctions is the same, thus no voltage will be measured between the terminals non-connected (A, A); however if the temperature is different in the junctions, then a voltage will be measured in the terminals (Seebeck effect) [2.6]. This is the basic operation in thermo-electric detectors. In order to have high sensitivity in these detectors, the used materials must have high Seebeck coefficients. The combination aluminum/polycrystalline silicon, which is compatible with the CMOS technology show a high Seebeck coefficient (around 65 μV/K).

The pyroelectric effect is presented by some materials, they exhibit spontaneous electric polarization. Pyroelectric detectors operate unbiased and are built with materials (generally dielectrics) that change their polarization, when they are subjected to changes of temperature. These devices work with a chopper system in order to generate a modulation in their polarization and therefore in its current, which is monitored by an external circuit [2.7]. Ferroelectric detectors operate in a similar way as pyroelectric devices, however they need a bias. Lithium Tantalite (LiTa), Barium Strontium Titanate ($Ba_xSr_{1-x}TiO_3$) are pyroelectric materials commonly employed in thermal detectors.

Micro-bolometers are thermal detectors, in which the absorption of IR radiation causes a change on its resistance. The change in resistance is measured by an external circuit [2.7]. Some materials commonly employed in micro-bolometers are vanadium oxide (VO_x) and high resistive hydrogenated amorphous silicon (a-Si:H).

Table 2.2. Thermal detectors with common materials employed.

Thermal detectors	**Materials**	**Characteristics**	**Advantages over photon detectors**
Bolometers	Vanadium oxide (VO_x), Poly-SiGe, Poly-Si, a-Si:H	High responsivity, Bias required, DC response	Work without refrigeration, No limitation on wavelength, Low cost 2-D arrays fabrication, Portable applications
Thermopiles	Bi/Sb, Al/Poly-Si	Low responsivity, No Bias required, DC response	
Pyroelectric / Ferroelectric	Lithium tantalite (LiTa) Barium strontium titanate ($Ba_xSr_{1-x}TiO_3$)	High responsivity, No Bias required, Chopper required	

In comparison with photon detectors, thermal detectors operate at room temperature, reducing significantly the cost of operation and have not limitation on the wavelength at which they will respond, however its response time is in the range of milliseconds, which is larger than that of photon detectors.

Table 2.2 shows the different thermal detectors as well as the common materials that are used in its fabrication.

2.3 Un-cooled micro-bolometers

As was mentioned in the previous section, the operation of a micro-bolometer is based on the temperature rise of its thermo-sensing material by the absorption of

the incident IR radiation. The change in temperature causes a change on its electrical resistance, which is measured by an external circuit. Micro-bolometers based on a-Si:H or a-Ge:H have advantages over other types of thermal detectors, including micro-bolometers that use another kind of thermo-sensing materials.

The advantages are mainly technological, since these micro-bolometers are fully compatible with silicon CMOS fabrication technology, there is no need of additional fabrication equipment in a CI production line. Are relatively of simple fabrication and can be processed at relatively low temperature by PECVD. Which make them ideal for a post-process fabrication over a CMOS read-out circuit.

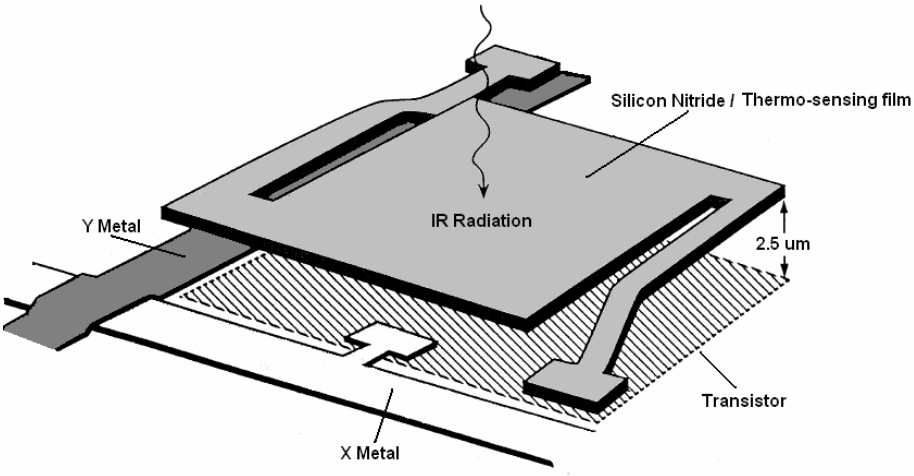

Figure 2.4. Micro-bolometer scheme [2.8].

Figure 2.4 shows a scheme of one micro-bolometer [2.8]; as was discuss for thermal detectors, it is built on a membrane. Over the membrane is deposited the thermo-sensing material and the IR absorber material.

2.3.1 Thermal insulation (configurations and materials)

There are three mechanism of heat transfer that occur in a thermal detector, they are conduction, convection and radiation. Conduction mechanisms occur when the heat flows from the thermo-sensing area along the supporting legs to the

substrate. Conduction is critical when the pixels are very close, since the heat can flow from one pixel to a neighbor pixel. Convection occurs when the heat flows in the presence of a surrounding atmosphere, this mechanism is not very important if the detector is encapsulated in a vacuum package. Radiation mechanism is presented by the fact that the detector radiates to its surroundings and the surroundings radiate to it.

When the micro-bolometers are encapsulated in an evacuated package, with an IR transmitting window, convection and radiation mechanism are minimized. Thus the main loss of heat mechanism is conduction from the thermo-sensing material to the substrate through the supporting structure.

The supporting structure is a very important part of thermal detectors, it provides three functions, mechanical support, electrical conducting path and thermal conducting path. In order to avoid heat losses in micro-bolometers, it is necessary to improve the thermal insulation. In micro-bolometers there are two main thermal insulation configurations: single-level and two-level, these configurations are shown in Figure 2.5.

Single level configuration consist in deposit a membrane over the silicon (Si) substrate and after that, open a hole in the Si substrate, employing bulk micro-machining techniques. Bulk micro-machining consumes area, since the Si substrate is etched with a side wall angel of 54.9 degrees. The electronic circuit (which forms part of the read out) is fabricated next to the pixel, consuming area also. That result in a 20% fill factor.

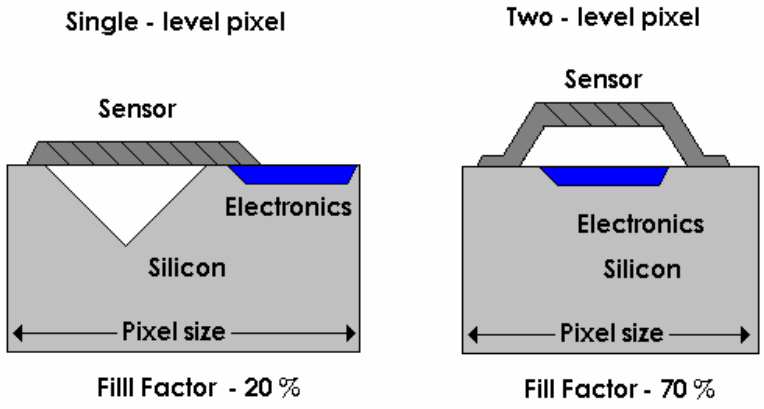

Figure 2.5. One and two level micro-bolometer configurations.

Figure 2.6 shows a SEM picture of one single-level micro-bolometer [2.9]. The two-level configuration allows the fabrication of the electronics circuit in the substrate and after that, the fabrication of the micro-bolometer in a low temperature post processing over the electronics, by using the surface micro-machining techniques. With this configuration is saved substrate area, achieving a fill factor of 70%. Figure 2.7 shows a SEM picture of a two-level micro-bolometer [2.10].

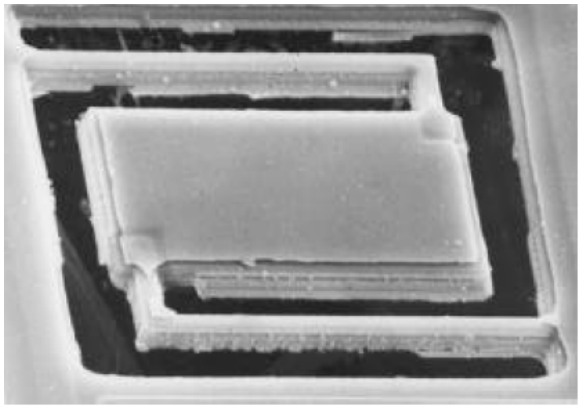

Figure 2.6. One- level micro-bolometer SEM image [2.9].

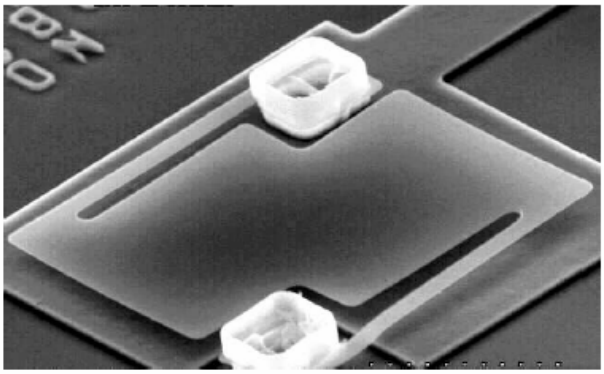

Figure 2.7. Two- level micro-bolometer SEM image [2.10].

Two-level micro-bolometers have several advantages over the one-level devices, due to their higher fill factor, therefore these are more suitable for the development of 2D arrays. Table 2.3 shows the most common combinations of

materials employed for supporting \ sacrificial films, fabricated by surface micro-machining techniques.

Table 2.3 Common combinations of materials employed for supporting \ sacrificial films, fabricated by surface micro-machining techniques.

Deposition Process	**Supporting layers / Deposition Temp.**	**Sacrificial layers / Deposition Temp. / Re-flow**	**Sacrificial Etchant**
LPCVD	Poly-Si / 900 ^{o}C	Oxide, PSG / 400 ^{o}C / 900 ^{o}C	HF
	Si_3N_4 / 700 ^{o}C	1. Oxide, PSG / 400 ^{o}C / 900 ^{o}C 2. Poly-Si / 700 – 900 ^{o}C	1. HF 2. KOH
PECVD	SiC / 400 ^{o}C	1. Oxide, PSG / 400 ^{o}C / 900 ^{o}C 2. Polymide /200 ^{o}C / 400 ^{o}C	1. HF 2. Dry etching (O_2)
	SiN_x / 350 – 400 ^{o}C	Polymide /200 ^{o}C / 400 ^{o}C	Dry etching (O_2)
	SiO_2 / 400 ^{o}C	Polymide /200 ^{o}C / 400 ^{o}C	Dry etching (O_2)

In order to fabricate thermal sensors in a post process, over a wafer surface, containing an IC circuit; it is necessary to use low temperatures, during the fabrication process. By employing Plasma Enhanced Chemical Vapor deposition (PECVD) it is possible to deposit thin films at relatively low temperatures (~ 350 – 400 ^{o}C), as is shown in Table 2.3.

2.3.2 Infrared absorber films

An absorber element is a very important part in un-cooled IR micro-bolometers, its role is based in the absorption of IR radiation and the transfer of heat to the thermo-sensing material.

The main requirements of absorbing materials for un-cooled micro-bolometers are: A high absorbance coefficient in the range $\lambda = 8 – 12$ μm, simple fabrication and compatibility with the silicon CMOS technology.

The IR absorption can be improved employing a resonant micro-cavity, where the thermo-sensing film is separated from the substrate by a gap equivalent to one quarter of the wavelength at which it will be operating. A mirror (Al or Ti) is deposited over the substrate surface, under the thermo-sensing material. In this configuration the radiation that was not absorbed by the thermo-sensing film will resound inside the cavity and will be re-absorbed by the thermo-sensing element.

Terrestrial objects have temperatures around of 300K, with IR emission centered in 10 μm. Thus un-cooled micro-bolometers employed for detection of objects at room temperature, should have a gap from the substrate of 2.5 μm, for the fabrication of the resonant micro-cavity.

Several materials have been employed as absorbing films in micro-bolometers, which are deposited over the thermo-sensing film. Among the most employed are some metals, such as gold black film [2.11], which has a very high absorption coefficient of IR radiation (more than 90 %), however it is not a standard material in CMOS technology. SiN_x films are employed commonly as absorber films in micro-bolometers [2.9, 2.12-2.13], since its absorption coefficient can be tuned by the deposition parameters and is a standard material in CMOS technology.

2.3.3 Thermo-sensing films (materials, fabrication processes)

The thermo-sensing material is perhaps the most important element in a micro-bolometer. As was discussed in section 2.2.3, the increment in temperature in the sensing material causes a change in some temperature-dependent parameter. In the case of a micro-bolometer that parameter is the resistance.

The thermo-sensing material should have a large temperature coefficient of resistance, TCR (α(T)), which is defined by Equation 2.2, where E_a is the activation energy, K is the Boltzman constant and T is temperature.

$$\alpha(T) = \left(\frac{1}{R}\right)\left[\frac{dR}{dT}\right] \approx \frac{E_a}{KT^2} \qquad (2.2)$$

A large TCR means that a small change in temperature in the sensing material will result in a large change in resistance. Equation 2.2 shows that the TCR and E_a are directly related, thus a high E_a in the material is desired.

For un-cooled micro-bolometers vanadium oxide, VO_x, was the first thermo-sensing element employed [2.14-2.16], since it has a relatively high TCR, $\alpha(T) \approx 0.021\ K^{-1}$, however it is not a standard material in silicon CMOS technology. Some metals have been employed also, which are compatible with Si-CMOS technology, however they have low values of TCR (Pt, $\alpha(T) \approx 0.0015\ K^{-1}$).

Hydrogenated amorphous silicon (a-Si:H) prepared by PECVD is a material commonly used in micro-bolometers as thermo-sensing film, for room temperature operation [2.10]. It is compatible with the IC technology, has a high activation energy, $E_a \approx 0.30$ eV and high value of TCR, $\alpha(T) \approx 0.039\ K^{-1}$, however it also has a high undesirable resistivity, which often cause a mismatch with the input impedance of the read-out circuits. In order to reduce the a-Si:H high resistance, boron doping has been employed. The B doped a-Si:H films present a significant reduction in its resistivity, however a reduction in E_a and TCR is obtained also, Ea ≈ 0.22 eV and TCR ≈ $0.028\ K^{-1}$ [2.10].

Table 2.4 Common materials employed as thermo-sensing films in micro-bolometers.

Material	**TCR (K^{-1})**	**Ea (eV)**	**σ_{RT} $(\Omega\ cm)^{-1}$**	**Reference**
VO_x	0.021	0.16	$2x10^{-1}$	[2.14-1.16]
a-Si:H (PECVD)	0.039	0.30	~ $1x10^{-9}$	[2.9,2.17]
a-Si:H,B (PECVD)	0.028	0.22	$5x10^{-3}$	[2.10]
a-SiGe:H (PECVD)*	0.043	0.34	$1.6x10^{-6}$	[2.17-2.18]
Poly-SiGe	0.024	0.18	$9x10^{-2}$	[2.12-2.13]
$Ge_xSi_{1-x}O_y$	0.042	0.32	$2.6x10^{-2}$	[2.19-2.21]
YBaCuO	0.033	0.26	$1x10^{-3}$	[2.22-2.25]

* INAOE works.

In previous works performed at INAOE [2.17-2.18], amorphous silicon – germanium, a-Si_xGe_y:H, deposited by PECVD has been employed as thermo-sensing films in un-cooled micro-bolometer, obtaining high activation energy, E_a= 0.34 eV, consequently a high value of TCR = 0.043 K^{-1} and improved but still high resistivity. Table 2.4 shows the most common materials employed as thermo-sensing films in micro-bolometers. As can be seen in Table 2.4, there are available several materials which can be used as thermo-sensing films in micro-bolometers. Intrinsic amorphous silicon, a-Si:H and amorphous silicon –germanium, a-SiGe:H, show the largest TCR values and are fully compatible with the silicon CMOS technology, however they have also the smallest values of room temperature conductivity, σ_{RT}.

2.4 IR focal plane arrays (IRFPAs)

The development of infrared cooled detectors started in 1959 with the identification of the intrinsic semiconductor material: mercury cadmium telluride (HgCdTe), which is a photoconductor that require cooling of 77 K [2.7]. In the decade of 1960s began the development of IR cooled imaging arrays based on HgCdTe photoconductor detectors. Since then, several architectures for IR imaging arrays have been proposed. In the following sections are described the most important architectures employed in IR imaging systems.

2.4.1 IRFPA architectures

Two main architectures of IR imaging system have been used [2.4]. The first architecture, which is the simplest, consisted of a one dimensional (1-D) array. In order to create an image, the scene is scanned at standard video frame rates employing a mechanical scanner. These kinds of systems are called scanning linear IRFPAs [2.4], were the first generation of imaging systems consisted of cooled photoconductive detectors based on HgCdTe, PbSe, etc. Figure 2.8 shows a diagram of a scanning IR FPA. The second architecture used in IR imaging systems are called

staring IRFPAs, which consisted in two dimensional arrays (2-D) of thermal detectors. In these devices the pixels (detectors) are scanned electronically, employing a readout circuit (ROIC), which consist of multiplexers, switches and preamplifiers.

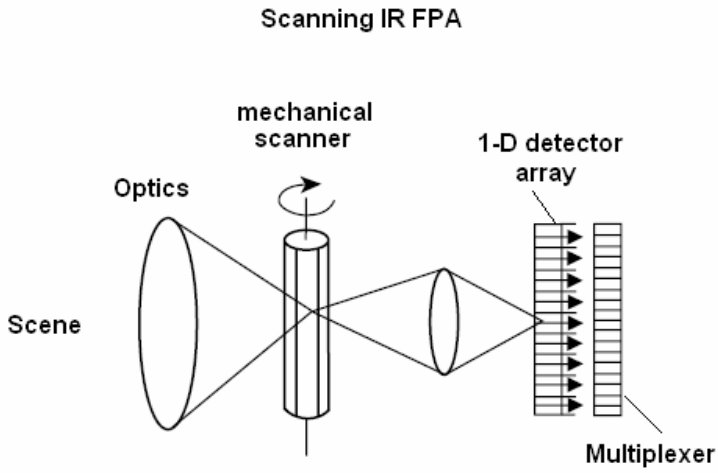

Figure 2.8. Diagram of a scanning IR FPA [2.4].

Staring systems are considered the second generation of imaging systems and contain mainly un-cooled thermal detectors, such as thermopiles, pyroelectric detectors and micro-bolometers. Figure 2.9 shows a diagram of a staring IRFPA system.

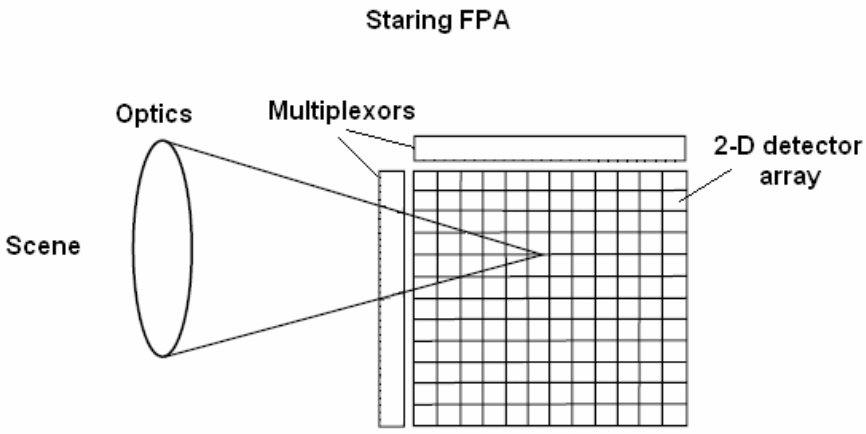

Figure 2.9. Diagram of a staring IR FPA [2.4].

Staring IRFPAs have several advantages over scanning systems, they are cheaper systems, since do not need additional equipment for refrigeration, the fabrication process can be compatible with the CMOS technology, reducing significantly the production costs and can be used for low weight-portable applications. Among staring IRFPAs there are two main configurations, which are hybrid and monolithic, these configurations are described in the following sections.

2.4.2 Hybrid technology

At the end of 1970s it was started the development of un-cooled IRFPAs mainly in the US. Two main approximations were followed by two companies. Texas Instruments started the work with un-cooled micro-bolometer arrays employing pyroelectric / ferroelectric detectors, based on $Ba_xSr_{1-x}TiO_3$. They employed the hybrid technology, where the IR array is fabricated in one substrate and the ROIC in another substrate, then both parts are joined together employing a special bonding method called "flip chip binding or bump-bond" [2.4,2.7], where is employed indium (In) for bonding. Figure 2.10 shows the hybrid technology.

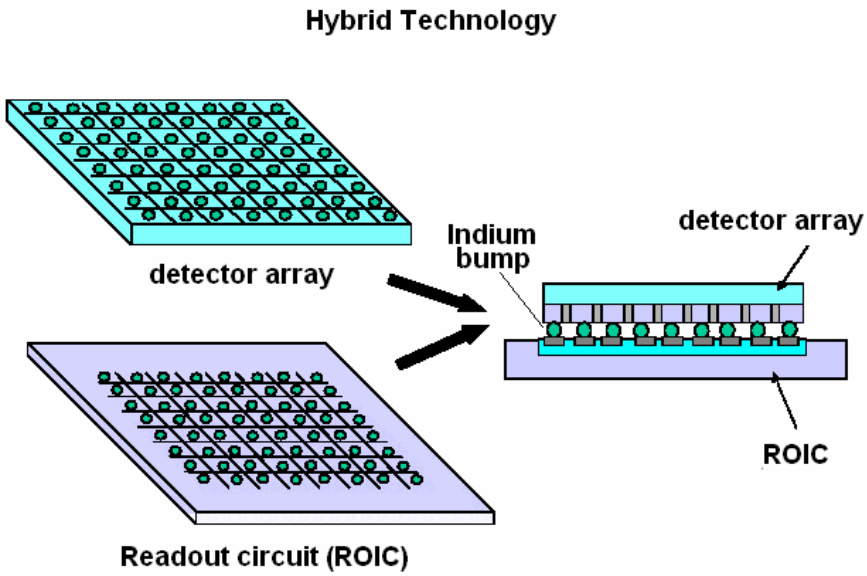

Figure 2.10. Hybrid technology for IRFPAs.

Hybrid technology has some advantages, it is possible to optimize the detector array and the ROIC separately and the fill factor is very large, near to 100%. However is more complex to work with two substrates and join them together, it implies more process steps and the indium bump technique is not a standard process in Si CMOS technology.

2.4.3 Monolithic technology

The second approximation for un-cooled imaging arrays is the monolithic technology, developed by Honeywell in 1983. It consisted in the fabrication of the ROIC circuit in a Si wafer and over it fabricate the detector array in the wafer surface employing surface micro-machining techniques, at lower temperatures than those employed for the ROIC fabrication. They employed micro-bolometers based on VO_x films in the arrays, however it is possible to use any kind of thermo-sensing material. Figure 2.11 shows a top picture of a monolithic IRFPA [2.9], while Figure 2.12 shows a part of a monolithic array of micro-bolometers based on a-Si:H developed by Sillayos (Raytheon) [2.10].

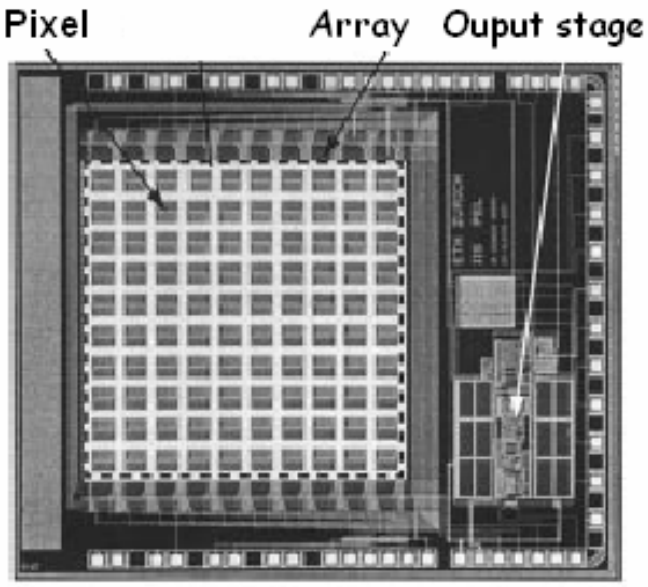

Figure 2.11. Monolithic technology IRFPAs [2.9].

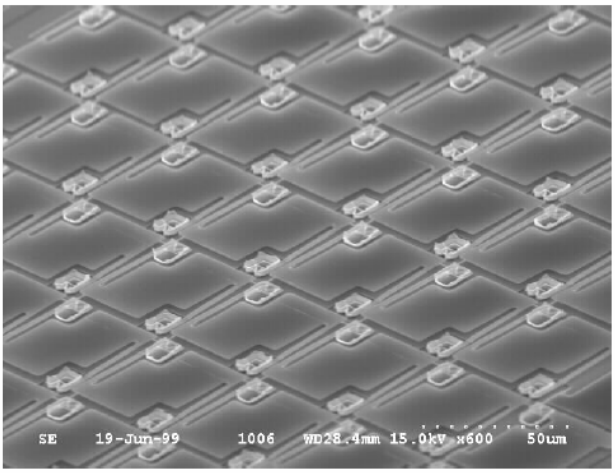

Figure 2.12. Monolithic IRFPA [2.10].

At the present time monolithic technology is widely used, since it is possible to provide higher thermal isolation to the thermo-sensing materials by the structures fabricated with silicon micro-machining. This technology is simple, since the detector array and ROIC are fabricated in the same substrate, giving as a result a reduction in fabrication costs.

2.5 Figures of merit of micro-bolometers and micro-bolometer arrays

In this section the different figures of merit of a micro-bolometer, such as thermal characteristics, responsivity, detectivity and noise equivalent temperature difference (NETD) are presented. The different types of noise in micro-bolometer are described also.

2.5.1 Thermal capacitance, C_{th}, thermal conductance, G_{th} and thermal response time, τ_{th}

A simple representation of a micro-bolometer is shown in Figure 2.13, the detector has a thermal capacitance, C_{th}, and it is coupled to the substrate which is a heat sink, by a thermal conductance, G_{th}.

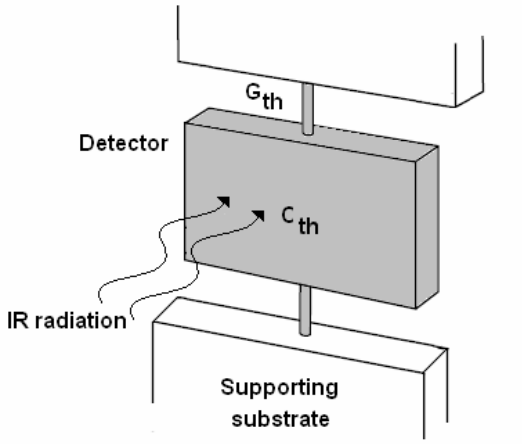

Figure 2.13. Micro-bolometer representation.

When the detector receives modulated IR radiation, the rise in temperature is found by solving the balance equation, Equation 2.3; where C_{th} (expressed in JK^{-1}) is the thermal capacitance of the supporting membrane containing the thermo sensing film, G_{th} (expressed in WK^{-1}) is the thermal conductance of the legs, which is considered the main heat loss mechanism, ΔT is the temperature difference of the hot and reference junctions. A_{cell} is the detector area, β is the fill factor, which is the radio of the thermo-sensing film area to the total cell area, η is the optical absorption coefficient, defined as the fraction of the radiant power falling on the thermo-sensing area, which is absorbed by that area. P_o is the intensity of the IR modulated radiation, ω is the angular modulation frequency and t is time [2.6].

$$C_{th}\frac{d(\Delta T)}{dt}+G_{th}(\Delta T)=\eta\beta A_{cell}P_o\exp(j\varpi t) \qquad (2.3)$$

The solution of the balance equation is shown in Equation 2.4:

$$\Delta T=\frac{\eta\beta A_{cell}P_o}{G\left(1+\varpi^2\tau_{th}^{\,2}\right)^{1/2}} \qquad (2.4)$$

Where, τ_{th} (expressed in seconds) is the thermal response time of the micro-bolometer, it is defined by Equation 2.5, which establishes a relation between τ_{th}, C_{th} and G_{th}. Typical values of thermal time constant are in the range of milliseconds, which are much longer than the typical time of photon detectors.

$$\tau_{th} = \frac{C_{th}}{G_{th}} \qquad (2.5)$$

For unmodulated radiation Equation 2.4 can be reduced to:

$$\Delta T(\varpi = 0) = \frac{\eta \beta A_{cell} P_o}{G_{th}} \qquad (2.6)$$

Equation 2.6 shows that the increment of temperature, ΔT, in the detector is inversely proportional to the thermal conductance G_{th} of its legs. In order to achieve a high performance micro-bolometers ΔT should be as high as possible and G_{th} as small as possible, it can be done by making very thin the detector legs.

2.5.2 Responsivity.

Responsivity, *R*, is defined as the ratio of the pixel (cell) output signal to the incident radiant power (in Watts) falling on the pixel [2.6-2.7]. The output signal is an electrical signal that can be voltage or current, thus *R* can be expressed in Volts/Watts (voltage responsivity, R_u) or Amps/Watts (current responsivity, R_I). In order to obtain *R*, we can use the simplest model, where it is assumed that there is no heating due the electrical bias in the detector (Joulean heating), and also it is assumed a constant electrical bias to the detector. When the micro-bolometer is current biased, the output signal is voltage, V_s, given by Equation 2.7, where I_b is the bias current, R_{cell} is the electrical resistance of the micro-bolometer, α is the TCR, described by Equation 2.2 and ΔT is the increment of temperature in the detector, obtained in Equation 2.6.

$$V_s = I_b \alpha R_{cell} \Delta T \quad (2.7)$$

Voltage responsivity, R_v, is obtained by combining Equations 2.4 and 2.7, and dividing by $P_o A_{cell}$, which is the incident radiant power, the result is shown in Equation 2.8.

$$R_V = \frac{\eta \beta I_b \alpha R_{cell}}{G\left(1 + \varpi^2 \tau_{th}^{\ 2}\right)^{1/2}} \quad (2.8)$$

$$R_V = \frac{\eta \beta I_b \alpha R_{cell}}{G} \quad (2.9)$$

For unmodulated radiation, ω = 0, Equation 2.8 is simplified in Equation 2.9, which is the DC responsivity. When the micro-bolometer is voltage biased Equations 2.8 and 2.9 are transformed to Equations 2.10 and 2.11 respectively, where R_I is current responsivity.

$$R_I = \frac{\eta \beta V_b \alpha}{G R_{cell}\left(1 + \varpi^2 \tau_{th}^{\ 2}\right)^{1/2}} \quad (2.10)$$

$$R_V = \frac{\eta \beta V_b \alpha}{G R_{cell}} \quad (2.11)$$

2.5.3 Noise in micro-bolometers.

There are four main sources of noise in micro-bolometers [2.6], which are Johnson noise, 1/f noise, temperature fluctuation noise and background fluctuation noise, these noise types are uncorrelated and are described in the following subsections.

A. Johnson noise.

The Johnson noise component, V_j, is described by Equation 2.12, where k is the Boltzmann constant, T_{cell} is the bolometer temperature, R_{cell} is the bolometer resistance and Δf is the bandwidth of the integration time.

$$V_j = \left(4kT_{cell}R_{cell}\Delta f\right)^{1/2} \qquad (2.12)$$

B. 1/f noise.

The 1/f noise is characterized by a spectrum that depends inversely on frequency and is described by Equation 2.13, where V is the product of the bias current, I_b and the electrical resistance of the micro-bolometer, R_{cell}, f is the frequency at which the noise is measured and n is the 1/f noise parameter, which depend on the material detector.

$$V_{1/f} = \left(\frac{V^2 n}{f}\right)^{1/2} \qquad (2.13)$$

1/f noise is the dominant noise at low frequencies and falls below the Johnson noise at higher frequencies, the transition is commonly called the “knee”.

C. Temperature fluctuation noise.

A thermal detector which is in contact with its enviroment (by conduction and radiation), exhibits random fluctuations in temperature, since the interchange of heat with its surrondings has a ststistical nature; this is known as temperature fluctuation noise.

The mean square temperature fluctuation noise voltage is given by the equation 2.14 [2.6].

$$\overline{V_{TF}}^2 = \frac{4kT_{cell}{}^2\Delta f}{G\left(1+\varpi^2\tau_{th}{}^2\right)^{1/2}}V^2\alpha^2 \qquad (2.14)$$

D. Background fluctuation noise.

When the heat exchange by conduction between the detector and its surroundings is negligible, in comparison with the radiation exchange, the temperature fluctuation noise will be identified as background fluctuation noise.

The mean square background fluctuation noise is given by Equation 2.15, where T_{cell} is the detector temperature and T_B is the background temperature.

$$\overline{V_{BF}}^2 = 8A_{cell}\eta\sigma k\left(T_{cell}{}^5 + T_B{}^5\right)R_{cell}{}^2 \qquad (2.15)$$

The total noise voltage is obtained by adding the 4 noise contributions as is shown in Equation 2.16.

$$\overline{V_N{}^2} = \overline{V_j{}^2} + \overline{V_{1/f}{}^2} + \overline{V_{TF}{}^2} + \overline{V_{BF}{}^2} \qquad (2.16)$$

The noise obtained in Equation 2.16 is the total mean square noise voltage. In order to obtain the noise current it is possible to divide the voltage noise by the bolometer resistance, R_{cell}, as is shown in Equation 2.17.

$$\overline{I^2}_N = \frac{\overline{V_N{}^2}}{R_{cell}} = \frac{\overline{V_j{}^2}}{R_{cell}} + \frac{\overline{V_{1/f}{}^2}}{R_{cell}} + \frac{\overline{V_{TF}{}^2}}{R_{cell}} + \frac{\overline{V_{BF}{}^2}}{R_{cell}} \qquad (2.17)$$

2.5.4 Detectivity.

Detectivity, D^* (expressed in $cmHz^{1/2}Watt^{-1}$), is a figure of merit for all types of detectors, it is defined as the pixel output signal to noise ratio per unit of incident radiant power falling on the detector, measured in a 1Hz bandwidth [2.7]. In other words, D^* is the normalized signal to noise ratio in the detector and is shown in Equation 2.18.

$$D^* = \frac{R_V \left(A_{cell}\Delta f\right)^{1/2}}{V_N} \qquad (2.18)$$

In Equation 2.18 R_v is the voltage responsivity, A_{cell} is the detector area, Δf is the frequency bandwidth and V_N is the contribution of the four noises described in section 2.5.3. It is clear that in order to achieve a high D^* the responsivity should be as high as possible and the noise as small as possible.

The fundamental limit to sensitivity of any thermal detector is set by random fluctuations in the temperature of the detector due to fluctuations in the radiant power exchange between the detector and its surroundings. The highest possible value of D^* of a thermal detector operated at room temperature is $D^* = 1.98 \times 10^{10}$ $cmHz^{1/2}W^{-1}$ [2.4].

2.5.5 Noise equivalent temperature difference (NETD).

The Noise equivalent temperature difference, NETD, is defined as the change in a blackbody temperature that cause a change in signal to noise ratio of unity in the electrical output of a thermal detector. Equation 2.19 shows the NETD expression [2.6, 2.25].

$$NETD = \frac{(4(f/D)^2 + 1)V_N}{\tau_0 A_{cell} R_V \left(\Delta P/\Delta T\right)_{\lambda_1-\lambda_2}} \qquad (2.19)$$

For voltage biasing Equation 2.19 is transformed to Equation 2.20.

$$NETD = \frac{(4(f/D)^2 + 1)I_N}{\tau_0 A_{cell} R_I (\Delta P / \Delta T)_{\lambda_1 - \lambda_2}} \qquad (2.20)$$

In the expression of NETD f is the focal length of the optics, D is the diameter of the optics, (f/D) is the focal ratio of the optics, R_v is the voltage responsivity (R_I is the current responsivity), A_{cell} is the detector area, V_N is the total noise within the system bandwidth (I_N is the total current noise within the system bandwidth), τ_0 is the transmittance of the optics. $(\Delta P/\Delta T)_{\lambda 1-\lambda 2}$ is a black body function, which gives the change in power per unit area, radiated by a blackbody at temperature T, with respect to T, measured from λ_1 to λ_2. If it is assumed an operation in the spectral interval λ=8-12 μm, and a 300 K temperature of the scene, then $(\Delta P/\Delta T)_{\lambda 1-\lambda 2} = 2.62$ WK^{-1}.

2.6 Readout integrated circuit (ROIC) for micro-bolometer arrays

In the development of IRFPAs, the read-out circuit electronics is an important issue in the IR detector array. Read-out electronics is designed to support a good interface between IR detectors and the following signal processing stage.

In this section the operation of a readout integrated circuit (ROIC) is discussed. Since the development of ROIC is a special serious task being out of the goals of the present work, only a brief description of a ROIC basic operation is described.

The basic function of the read-out circuit operating with an array is to convert an optical signal in to an electrical, by means of applying a short bias pulse to each bolometer in the array, while simultaneously measuring the signal (V or I) from each micro-bolometer [2.6-2.7, 2.26].

The general circuit principle is shown in Figure 2.14. Row and column conductors are fabricated in the underlying Si, with an on-off electronic pixel switch

lying at each intersection of the rows and columns, with the objective of bias one micro-bolometer a time.

Peripheral circuits are placed in the Si substrate in order to control the voltage on each row and column. The control voltages on each row and column are used to open and close the electronic pixel switches at each micro-bolometer, allowing a bias pulse to be applied to any selected micro-bolometer(s). The resulting signal, current or voltage are routed to an output signal line [2.6].

A small array of dimensions 64 x 64 with a frame rate of 30 Hz implies a pixel time of 1 / (64 x 64 x 30) = 8.1 μsec. If a single micro-bolometer is read out at any instant (called a fully serial read-out), each micro-bolometer can be biased a pulse of duration t = 8.1 μsec. A suitable circuit is shown in Figure 2.15. In this circuit, each micro-bolometer is biased "on" for 8.1 μsec by application of a bias voltage V_b between the appropriate row and column metallization. The diode connected to each micro-bolometer acts as a self-closing pixel switch, which only conducts when the proper voltage is applied.

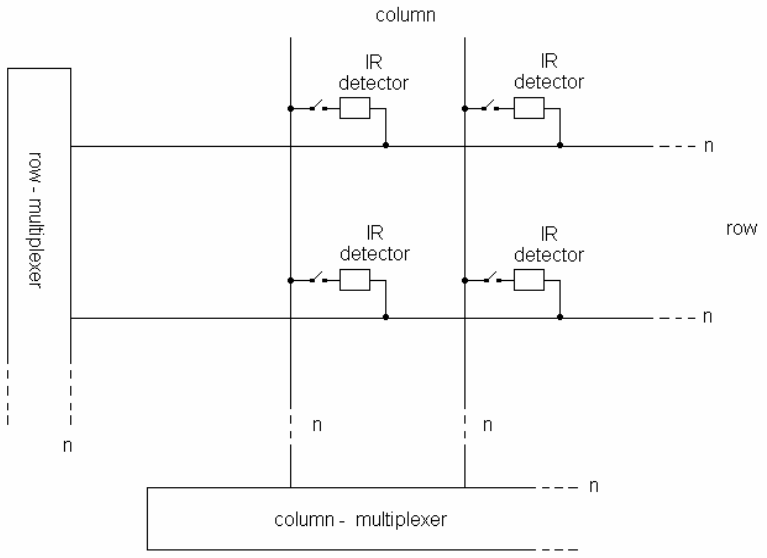

Figure 2.14. General operation of a ROIC.

The column metallization of the selected micro-bolometer is held at ground potential by the action of the preamplifier, which integrates the micro-bolometer

current on capacitor C during the interval of each pulse. At the end of each 8.1 μsec interval, the charge on C is discharged by momentarily closing switch S. The column and row multiplexers are part of the electronics employed for biasing independently each micro-bolometer in the array. In the current ROICs the diodes switches have been replaced by CMOS switches and the multiplexers have been replaced with shift registers, which make the similar operation, Figure 2.16 shows a typical ROIC employed for micro-bolometer IRFPAs [2.27].

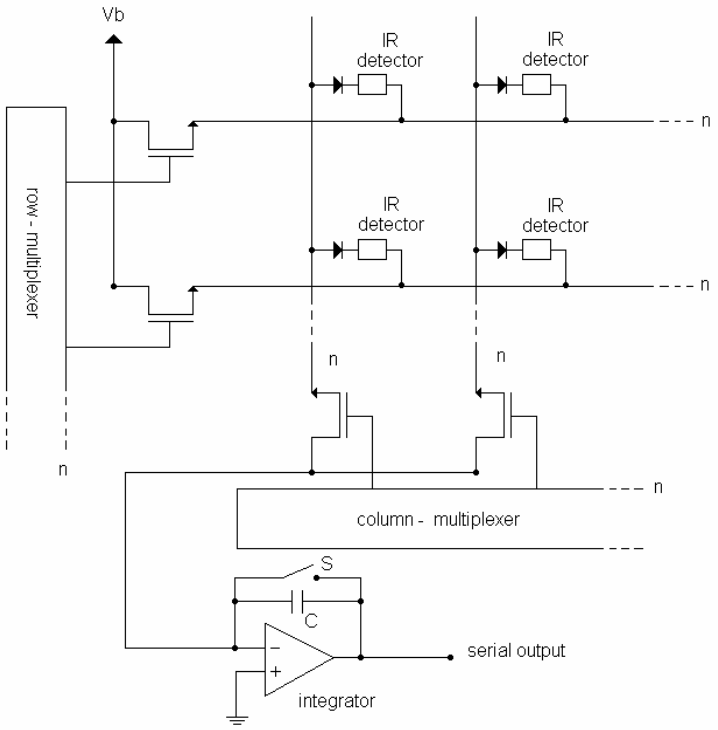

Figure 2.15. Serial ROIC.

In most of the current ROICs, the unit cell contains the micro-bolometer, the on-off pixel switch and the preamplifier. In some circuits the preamplifier is out of the cell and is shared by all the micro-bolometers, as shown in Figure 2.16.

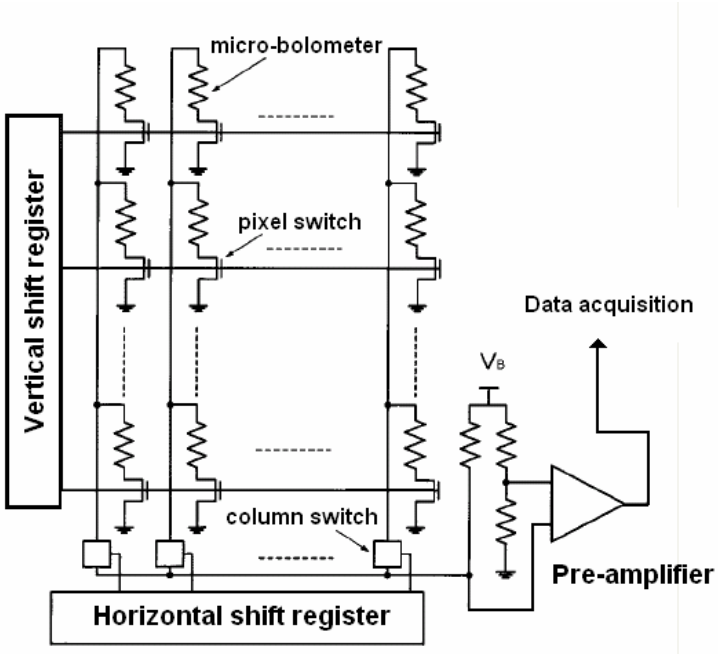

Figure 2.16. A typical ROIC [2.27].

There exist several techniques employed for the readout circuit for every cell in the array, it means that every cell in the array has its own preamplifier circuit and switch. Among the most employed techniques are the source follower per detector (SFD), direct injection (DI) and buffered direct injection (BDI) [2.28-2.29].

2.7 State of the art in micro-bolometers and micro-bolometer IRFPAs

In this section are presented the more recently achievements and advances in the field of micro-bolometer IRFPAs. At the present time two technologies of un-cooled micro-bolometer IRFPAs are presented in US, these are based in the development carried out in the decade of 1980 by two main companies: Texas instruments and Honeywell.

Vanadium oxide technology, VO_x, previously developed by Honeywell, is now continued under development by three main companies: Raytheon Infrared Operation, BAe systems and DRS technologies.

Meanwhile Amorphous silicon technology previously developed by Texas instruments and later by Raytheon Commercial Infrared, is now in development by L-3 communications / infrared products, (which acquired Raytheon Commercial Infrared in 2004).

In Europe, specifically in France, at ULIS (CEA/LETI), there is an important development in micro-bolometers arrays based on amorphous silicon technology.

The information related to un-cooled micro-bolometer IRFPAs is not completely open and some performance characteristics of micro-bolometers are not available. In the following paragraphs the information of the technology found in literature and in web sites is presented.

Table 2.5 shows the performance characteristics of Raytheon micro-bolometers IRFPAs based on VO_x [2.4, 2.30]. Among the main characteristics in these devices, is the array size of 320 x 240 and 640 x 480 pixels, the pixel size is 25 x 25 μ^2 and the pixel voltage responsivity is around $R_v > 2.5 \times 10^7$ VW^{-1}. However the larger array is already in development and is not available commercially.

Table 2.5. Performance characteristics of Raytheon VO_x IRFPAs [2.4, 2.30].

Performance parameter	**Capability (f/1 and 300 K scene)**		
Array dimensions	320 x 240	320 x 240	640 x 480
Pixel size (μm^2)	50 x 50	25 x 25	25 x 25
Spectral response (µm)	8 – 14	8 – 14	8 – 14
Responsivity (V/W)	> 2.5 x 10^7	> 2.5 x 10^7	> 2.5 x 10^7
NETD at f/1 (mK)	<20	<50	<50
Pixel operability (%)	> 98	> 98	> 98
Operating temperature (^oC)	25	25	25

The other two companies which develop IRFPAs based on VO_x films, BAe systems and DRS technologies do not show completely information in their devices.

Table 2.6 show some characteristics in the IRFPAs fabricated by BAe systems [2.31] while Table 2.7 shows the information obtained from DRS technologies [2.32].

Table 2.6. Performance characteristics of BAe VO_x IRFPAs [2.31].

Performance parameter	**Capability (f/1 and 300 K scene)**		
Array dimensions	320 x 240	640 x 480	640 x 480
Pixel size (μm^2)	28 x 28	28 x 28	28 x 28
Spectral response (µm)	7.5 – 14	7.5 – 14	7.5 – 14
Responsivity (V/W)	-	-	-
NETD at f/1 (mK)	-	-	-
Frame rate (Hz)	60	30	30
Operating temperature (^oC)	-46 to +49	-46 to +49	-46 to +52

Table 2.7. Performance characteristics of DRS VO_x IRFPAs [2.32].

Performance parameter	**Capability (f/1 and 300 K scene)**		
Array dimensions	320 x 240	640 x 480	320 x 240
Pixel size (μm^2)	25.4 x 25.4	25.4 x 25.4	51 x 51
Spectral response (µm)	8 – 12	8 – 12	8 – 12
Responsivity (V/W)	-	-	-
NETD at f/1 (mK)	-	-	-
Frame rate (Hz)	60	30	60
Operating temperature (^oC)	-20 to +49	-20 to +49	-10 to +45

Table 2.8 shows the main characteristics of the IRFPAs based on amorphous silicon (a-Si:H,B) technology developed by L-3 communications. At the present time there are commercially available micro-bolometer arrays with a maximum size of 320 x 240 pixels, however not much information about the micro-bolometer performance is available [2.33-2.34]. In Table 2.8 some performance micro-bolometer characteristics reported in 2000 by Raytheon (A. J. Syllaios) before to be acquired by L-3 communications are also included [2.10].

Table 2.8. Performance characteristics of L-3 com. a-Si:H,B IRFPAs [2.33-2.34].

Performance parameter	**Capability (f/1 and 300 K scene)**		
Information year	2000	2007	2007
Array dimensions	160 x 120	160 x 120	320 x 240
Pixel size (μm^2)	48 x 48	-	-
Pixel resistance (MΩ)	30	-	-
Pixel thermal resistance (KW^{-1})	4×10^7		
Spectral response (μm)	5 - 14	7 - 14	7 - 14
Responsivity (V/W)	1×10^6	-	-
NETD at f/1 (mK)	<100	50	< 50
Thermal time constant (ms)	11	-	-

As was discussed at the beginning of the section, ULIS (CEA/LETI) in France is developing IRFPAs based on amorphous silicon, they are working on large arrays, with a maximum size of 640 x 480 pixels and a pixel size or pitch (distance between the centers of adjacent micro-bolometers within an array) of 25 μm^2 [2.35-2.37].

Table 2.9. Performance characteristics of ULIS a-Si:H IRFPAs [2.35-2.37].

Performance parameter	**Capability (f/1 and 300 K scene)**		
Array dimensions	160 x 120	384 x 288	640 x 480
Pixel pitch (μm^2)	35	35	25
Pixel resistance (MΩ)	-	-	-
Spectral response (μm)	8 – 14	8 – 14	8 – 14
Responsivity (V/W)	-	-	-
NETD at f/1 (mK)	85	85	85
Frame Rate (Hz)	60	60	60
Thermal time constant (ms)	7	7	7
Pixel operability (%)	> 99.9	> 99.9	> 99.9
Operating temperature (^oC)	-30 - +60	-30 - +60	-30 - +60

ULIS micro-bolometers have showed the shorter thermal time constant which is in the range of 7 ms. Table 2.9 shows the main characteristics of ULIS micro-bolometers. Finally Table 2.10 shows the performance characteristics for the three main micro-bolometer IRFPAs which available commercially. Information about D^* and ROIC is not showed by these companies.

Table 2.10. Performance characteristics in the main micro-bolometer IRFPAs commercially available [2.4, 2.30, 2.33-2.34, 2.35-2.37].

Performance parameter	**Capability (f/1 and 300 K scene)**		
Manufacturer	Raytheon	L-3 Communications	ULIS
Thermo-sensing material	VO_x	a-Si:H,B	a-Si:H
Array dimensions	640 x 480	320 x 240	640 x 480
Pixel pitch (μm^2)	50 x 50	48 x 48	25
Pixel resistance (MΩ)	-	30	-
Spectral response (µm)	8 – 14	5 - 14	8 – 14
Responsivity (V/W)	$> 2.5 \times 10^7$	1×10^6	-
NETD at f/1 (mK)	50	50	85
Frame Rate (Hz)	-	-	60
Thermal time constant (ms)	-	11	7
Pixel operability (%)	> 98	-	> 99.9
Operating temperature (^oC)	25	-	-30 - +60

As it can bee seen in Table 2.10, there is an important advance in the development of un-cooled micro-bolometer IRFPAs. The tendency is clear, an increment in the number of pixels, a reduction in the pixel pitch and an improvement in the pixel performance characteristics, such as the reduction in the thermal time constant, a reduction in the NETD and an increment in detectivity, D^*.

2.8 Applications of un-cooled micro-bolometer arrays.

Un-cooled micro-bolometer arrays are used mainly in thermal imaging system with different applications; some of the more important civilian applications are described below:

- Biomedical applications.

  One of the recent applications of IR imaging systems is in biomedicine, where IR imaging systems are being applied in blood vessel flow scan [2.38], in order to observe a vasoconstriction in the blood flow, which in some body parts can be unhealthy.
- Preventive industrial maintenance.

  IR imaging systems are now been employed for predictive maintenance, in order to prevent failures where heating is avoided.
- Driver vision.

  Another application of low cost IR systems is the automotive industry. In the future most of cars will have an IR camera for night driving vision.
- Electrical maintenance.

  Preventive maintenance in the electrical and telephone lines is another application of IR systems, in order to avoid failures caused by over heating.
- Fire safety.

  For fire safety, IR cameras have an important use, either for domestic use or for forest fire prevention.
- Security (intrusion/parking).

  Security is one of the most employed applications of IR imaging systems, since it is possible to obtain an image of a scene in complete darkness.

2.8 Conclusions

In the present chapter an analysis of literature in the field of micro-bolometers and micro-bolometer arrays, IRFPAs, has been performed. From the reviewed issues we can conclude the following:

- There are several advantages of thermal detectors over photon detectors. Thermal detectors work at room temperature, which implies a lower operation cost, since they do not need cryogenic refrigerators and are suitable for low weight portable applications. Photon detectors have a limitation in the wavelength at which they work, dictated by the material band gap, E_g , that limitation is not presented in thermal devices.
- The advantages of micro-bolometers over other thermal detectors, is their capability to work without a chopper which reduce the weight of the system and have demonstrated higher performance characteristics.
- At the present two main technologies of un-cooled micro-bolometer arrays are available: VO_x and a-Si:H. VO_x based micro-bolometers are not compatible with the Si CMOS technology, while a-Si:H based micro-bolometers do, which reduces the fabrication cost and make it possible fabricate a-Si:H based IRFPAs in every standard silicon wafer fab.
- At the present time, there exist an important development in a-Si:H based micro-bolometer IRFPAs, with large arrays (640 x 480 pixels) available commercially, with a small pixel size (25 x 25 μm^2) and thermal response time of the pixels around τ_{th}=7 ms.
- Even at the present, there are commercially available large arrays, none of them contain an optimum pixel in terms of performance chracateristics, such as D^* and $\tau_{th.}$
- Data related to D^* and ROIC of micro-bolometer arrays is not published by the leader companies, such as L-3 communications, Raytheon and ULIS.

- At the present time there exist several applications of un-cooled thermal imaging systems and continuously are appearing more applications.

Therefore, there is a necessity of low cost un-cooled IR systems, for the increasing civilian market. Some of the key factors in order to continue the development of IRFPAs are: compatibility with the Si CMOS standard technology, larger number of pixels in the arrays, reduction in the pixel size, reduction in the thermal response time and in general, an improvement of the pixels performance characteristics.

2.9 References

[2.1] S. M. Sze, "Semiconductor Devices, Physics and Technology", John Wiley and Sons, pp. 258-266, 1985.

[2.2] http://www.cctv-information.co.uk/isg/thermal.html

[2.3] F.I. Crawford, "Electro optical sensors overview", Digital Avionics Systems Conference, 1997. 16th DASC., AIAA/IEEE, Vol. 1, pp. 5.1-7-14, 1997.

[2.4] Antoni Rogalski, "Infrared detectors: status and trends", Progress in Quantum Electronics, Vol. 27, pp. 59-210, 2003.

[2.5] Jozef Piotrowski, Antoni Rogalski, "New generation of IR photodetectors", Sensor and Actuators A, Vol. 67, pp. 146-152, 1998.

[2.6] Paul W. Kruse, "Uncooled thermal Imaging, arrays systems and applications", Tutorial text in optical engineering, Volume TT51, SPIE Press, 2001.

[2.7] Paul W. Kruse, David D. Skatrud, "Uncooled Infrared Imaging Arrays and Systems", Semiconductors and semimetals, Vol. 47, Academic Press, 1997.

[2.8] B. E. Cole, R. E. Higashi, and R. A. Wood, "Monolithic Two-Dimensional Arrays of Micromachined Microstructures for Infrared Applications", Proceedings of the IEEE, Vo. 86, No. 8, pp. 1679 - 1686, 1998.

[2.9] Andri Schaufelbühl, N. Schneeberger, Ulrich Münch, Marc Waelti, Oliver Paul, Oliver Brand, Henry Baltes, Christian Menolfi, "Uncooled Low-Cost

Thermal Imager Based on Micromachined CMOS Integrated Sensor Array", Journal of Microelectromechanical systems, Vol. 10, No. 4, pp. 503-510, December 2001.

[2.10] A. J. Syllaios, T. R. Schimert, R. W. Gooch, W. L. Mc.Cardel, B. A. Ritchey, J. H. Tregilgas, "Amorphous silicon microbolometer technology", Materials Research Society Symposium Proceedings . 609 A14.4.1, 2000.

[2.11] M Hirota and S. Morita, "Infrared sensors with precisely patterned Au-black absorption layer", SPIE Proc. Vol. 3436, pp. 623-634, 1998.

[2.12] S. Sedky, P. Fiorini, M. Caymax, C. Baert, L. Hermans and R. Mertens, "Characterization of Bolometers Based on Polycrystalline Silicon Germanium Alloys", IEEE Electron Device Letters, Vol. 19, No. 10, pp. 376- 378, 1998.

[2.13] Sherif Sedky, Paolo Fiorini, Kris Baert, Lou Hermans and Robert Mertens, "Characterization and optimization of Infrared Poly SiGe Bolometers", IEEE Transactions on Electron Devices, Vol. 46, No. 4 pp. 675 - 682, 1999.

[2.14] B. E. Cole, R.E. Higashi and R. A. Wood, "Monolithic Arrays of Micromachined Pixels for Infrared Applications", International Electron Devices Meeting, IEDM '98 Technical Digest., pp. 459 – 462, 1998.

[2.15] B. E. Cole, R.E. Higashi and R. A. Wood, "Micromachined Pixel Arrays Integrated with CMOS for Infrared Applications", IEEE International Conference on Optical MEMS, pp.63 – 64, 2000.

[2.16] Yong-Hee Han, In-Hoon Choi, Ho-Kwan Kang, Jong-Yeon Park, Kun-Tae Kim, Hyun-Joon Shin, Sung Moon, "Fabrication of vanadium oxide thin film with high temperature coefficient of resistance using $VO_2/V/V_2O_5$ multilayers for uncooled microbolometers", Journal of Thin Solid Films, Vol. 425, pp. 260-264, 2003.

[2.17] R. Ambrosio, A. Torres, A. Kosarev, A. Illinski, C. Zúñiga, A.S. Abramov, "Low frequency plasma deposition and characterization of $Si_{1-x}Ge_x$:H,F Films " J. Non-Cryst. Solids, vol. 338-340, pp. 91-96, 2004.

[2.18] A. Torres, A. Kosarev, M. L. García Cruz, R. Ambrosio, "Un-cooled micro-bolometers Based on Amorphous Germanium Film " *J. Non-cryst. Solids*, vol. 329, no.1-3, pp. 179 – 183, 2003.

[2.19] Enrique Iborra, Marta Clement, Lucía Vergara Herrero and Jesús Sangrador, "IR uncooled bolometers based on amorphous $Ge_xSi_{1-x}O_y$ on Silicon Micromachined structures", Journal of Microelectromechanical Systems, Vol. 11, No. 4, pp. 322- 329, 2002.

[2.20] A.H.Z. Ahmed and R. Niall Tait, "Characterization of amorphous $GE_xSi_{1-x}O_y$ microbolometer for thermal imaging applications", IEEE Transactions on Electron Devices, Vol. 52, No. 8, pp. 1900-1906, 2005.

[2.21] A. Ahmed, R.N. Tait, "Noise behavior of amorphous $Ge_xSi_{1-x}O_y$ for micro-bolometer applications", Journal of Infrared Physics & technology, Vol. 46, pp. 468-472, 2005.

[2.22] Agha Jahanzeb, Christine M. Travers, Zeynep Celik Butler, Donald P Butler and Stephen G. Tan, "A Semiconductor YBaCuO Micro-bolometer for Room Temperature IR Imaging", IEEE transactions on Electron devices, Vol. 44 No. 10, pp. 1795- 1801, 1997.

[2.23] Christine M. Travers, Agha Jahanzeb, Donald P Butler and Zeynep Celik Butler, "Fabrication of Semiconducting YBaCuO Surface-Micromachined Bolometer Arrays", Journal of Microelectromechanical Systems, Vol. 6, No. 3, pp. 271- 276, 1997.

[2.24] J. Delerue, A. Gaugue, P. Testé, E. Caristan, G. Klisnick, M. redon and A.Kreisler, "YBCO Mid-Infrared Bolometer Arrays", IEEE Transactions on Applied Superconductivity, Vol. 13, No. 2, pp. 176-179, 2003.

[2.25] Ali Yildiz, Zeynep Celik-Butler, and Donal P. Butler, "Microbolometers on a Flexible Substrate, for Infrared Detection", IEEE Sensors Journal, Vol. 4, No. 1, pp. 112-117 , 2004.

[2.26] Dean A. Scribner, Melvin R. Kruer, and Joseph M. Killiany, "Infrared Focal Plane Array Technology", Proceedings of the IEEE, Vol. 79. No. 1, pp. 65-85, January, 1991.

[2.27] X. He, G. Karunasiri, T. Mei, W,.J. Zeng, P. Neuzil and U. Sridhar, "Performance of Micro-bolometer Focal Plane Arrays Under Varying Pressure", IEEE Electron devices Letters, Vol. 21 No. 5, pp. 233-235, 2000.

[2.28] Chich-Cheng Hsieh, Chung-Yu Wu, Far-Wen Jih and Tai Ping Sun, "Focal-Plane-Arrays and CMOS Readout Techniques of Infrared Imaging Systems", IEEE Transactions on Circuits and Systems For VideoTechnology, Vo. 7 No.4, pp. 594-605, August 1997.

[2.29] Tsung-Hsin Yu, Chung-Yu Wu, Yung-Chung Chin, Pei-Yen Chen, Fa-Wen Chi, Jiunn-Jye Luo, Cheng Der Chiang and Ya-Tung Cherng, "A New CMOS readout circuit for uncooled bolometric infrared focal plane arrays", ISCAS 2000 – IEEE International Symposium on Circuits and Systems, II-493 – II-496, 2000.

[2.30] http://www.raytheon.com/products/320ufe/ (November 2007).

[2.31] www.baesystems.com/ (November 2007).

[2.32] http://www.drsinfrared.com/ (November 2007).

[2.33] http://www.l-3com.com/ (November 2007).

[2.34] http://www.thermal-eye.com/ (November 2007).

[2.35] http://www.ulis-ir.com/ (November 2007).

[2.36] J.L. Tissot, B. Fièque, C. Trouilleau, P. Robert, A. Crastes, C. Minassian, O. Legras, "First demonstration of 640 x 480 Uncooled Amorphous Silicon IRFPA with 25 μm pixel-pitch", Infrared Technology and Application XXXII", edited by Bjorn F. Andresen, Gabor F. Fulop, SPIE Proc. Vol. 6206, 2006.

[2.37] Eric Mottin, Astrid Bain, Jean-Luc Martin, Jean-Louis Ouvrier-Buffet, Sylvette Bisotto, Jean-Jacques Yon, Jean-Luc Tissot, "Uncooled amorphous silicon technology enhancement for 25-μm pixel pitch achievement", Infrared Technology and Applications XXVIII, SPIE Proc., Vol. 4820, pp.200-207 (2003).

[2.38] http://www.x20.org/ (November 2007).

CHAPTER 3. METHODOLOGY AND EXPERIMENTAL TECHNIQUES

3.1 Introduction

In the present chapter the methodology it is described for the design, the study of fabrication and characterization of both single cell un-cooled micro-bolometers and micro-bolometer arrays. In Section 3.2 the process flow for the design and fabrication of a single cell micro-bolometer studied previously at INAOE [1.12, 3.1] is described. This is the base for further development of arrays, which will described in sections 4.3-4.4. Section 3.3 presents the techniques employed for the characterization of the thermo-sensing films used in micro-bolometers. Measurements of temperature dependence of conductivity in the films and determination of Activation Energy (E_a); Secondary Ion Mass Spectroscopy (SIMS) and Fourier Transform Infrared Spectroscopy (FTIR) are also described, for analysis of the films compositions and hydrogen bonds, respectively.

Section 3.4 describes the methodology for the characterization of un-cooled micro-bolometers, such as current – voltage characteristics, I(U), in dark and under IR condition; noise measurements; thermal characterization and response time, all used for the determination of the detector figures of merit such as responsivity, R, and detectivity, D*. Specific characterization performed on the micro-bolometer arrays using an experimental read-out circuit, is described in section 3.5 and finally the conclusions related to methodological approach are given.

3.2 Methodology for the design and fabrication of un-cooled micro-bolometers in order to be able to design micro-bolometer arrays.

3.2.1. Study of planar structure micro-bolometer and process flow.

Earlier at INAOE [1.12, 3.1-3.3], there were designed and fabricated around 22 different micro-bolometer cells, with some variations in their structure and size.

Figure 3.1 shows a transversal view of one of these micro-bolometers, which are labeled “planar structure micro-bolometers”. Those devices are fabricated with surface micro-machining techniques over a c-Si wafer employing thin films deposited by plasma.

A planar structure micro-bolometer consists of a SiN_x micro-bridge which acts as supporting film and provides thermo isolation to the thermo-sensing film. An amorphous silicon-germanium (a-Si_xGe_y:H) thermo-sensing film is deposited over the SiN_x micro-bridge and it is covered with an IR absorbing SiN_x film. Windows are opened in the absorbing film and an aluminum layer is deposited in order to form the contacts with the sensing film.

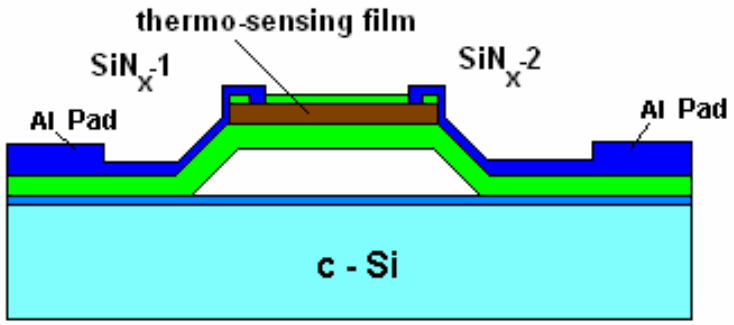

Figure 3.1. Planar structure micro-bolometer.

Figure 3.2 shows the design of the layout of a planar structure micro-bolometer. We can observe that for the micro-bolometer fabrication are needed 5 masks. Mask no. 1 is employed to pattern the sacrificial layer, mask no. 2 is employed for the SiN_x micro-bridge patterning, mask no. 3 is employed to pattern two films: the thermo-sensing film and the absorbing film. In order to open windows in the absorbing film the mask no. 4 is employed and, finally mask no. 5 is used for the metal contacts definition.

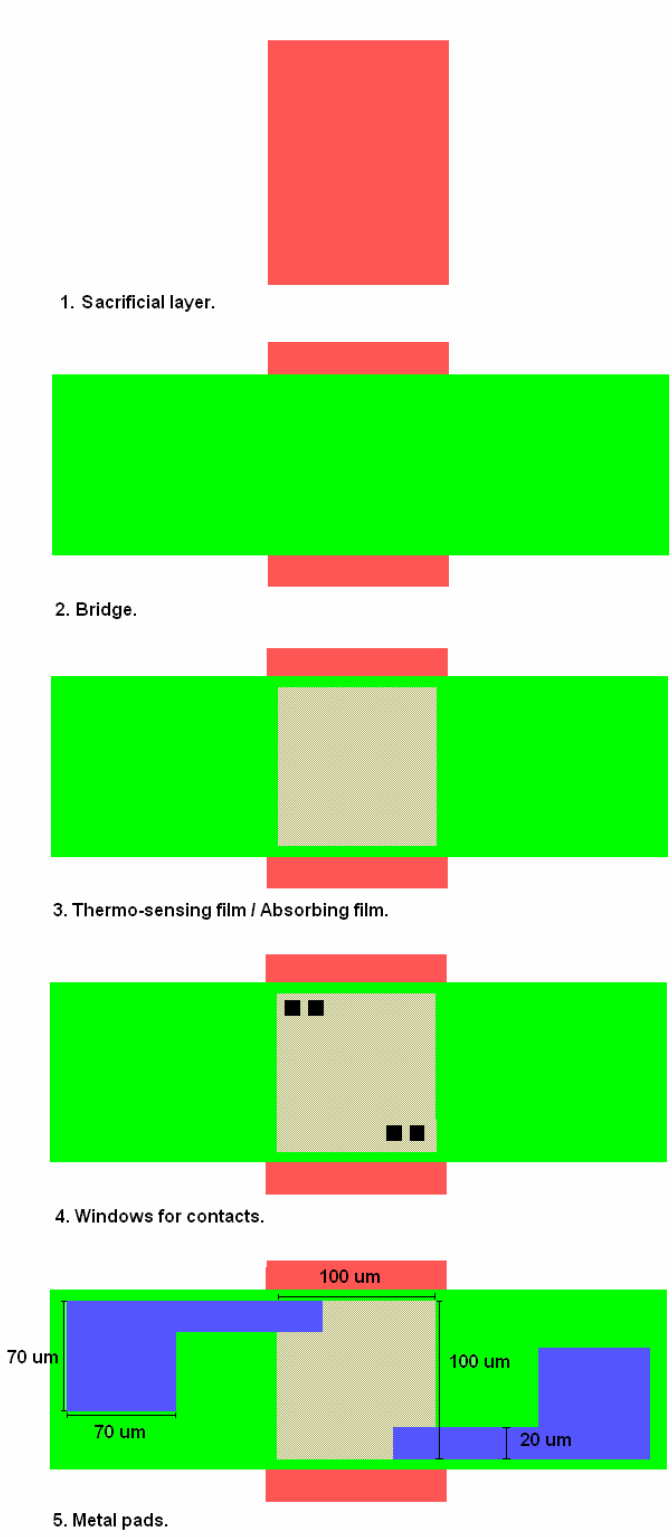

Figure 3.2 Design of the layout of a planar structure micro-bolometer.

The steps of the standard fabrication process of a micro-bolometer over a 2 inch c-Si wafer are the following:

1. A 0.3 μm – thick SiO_2 layer is deposited by CVD at T= 350 ^oC.
2. A 2.5 μm - thick aluminum (Al) layer is deposited by e-beam evaporation.
3. A lithographic and Al-etch steps are performed in order to pattern the Al sacrificial layer (mask no. 1).
4. A 0.8 μm - thick SiN_x film is deposited by low frequency plasma enhanced chemical vapor deposition (LF PECVD) over the Al pattern. A lithographic step and dry etching (RIE) are carried out in order to pattern the SiN_x micro-bridge (mask no. 2).
5. The Al sacrificial layer is removed with Al-etch and the micro-bridge is formed.
6. A 0.5 μm – thick a-Si_xGe_y:H thermo-sensing film is deposited by LF PECVD.
7. A 0.2 μm – thick absorbing SiN_x layer is deposited by LF PECVD.
8. A lithographic step and dry etching (RIE) are performed in order to pattern the active area (mask no. 3).
9. Windows are opened in the upper SiN_x layer for contacts, with a lithographic step and dry etching - RIE (mask no. 4).
10. Deposition of Al over the windows opened in order to form contacts with the a-Si_xGe_y:H thermo-sensing film. For that it is performed a lithographic step and e-beam evaporation (mask no. 5).

Figure 3.3 shows a scheme of the process flow described above, for the fabrication of a planar structure micro-bolometer. The micro-bolometer consists of 3 important films which are the SiN_x supporting film, the a-Si_xGe_y:H thermo-sensing film and the SiN_x absorbing film, those films have been deposited by LF PECVD. In the following sections these films are studied in detail.

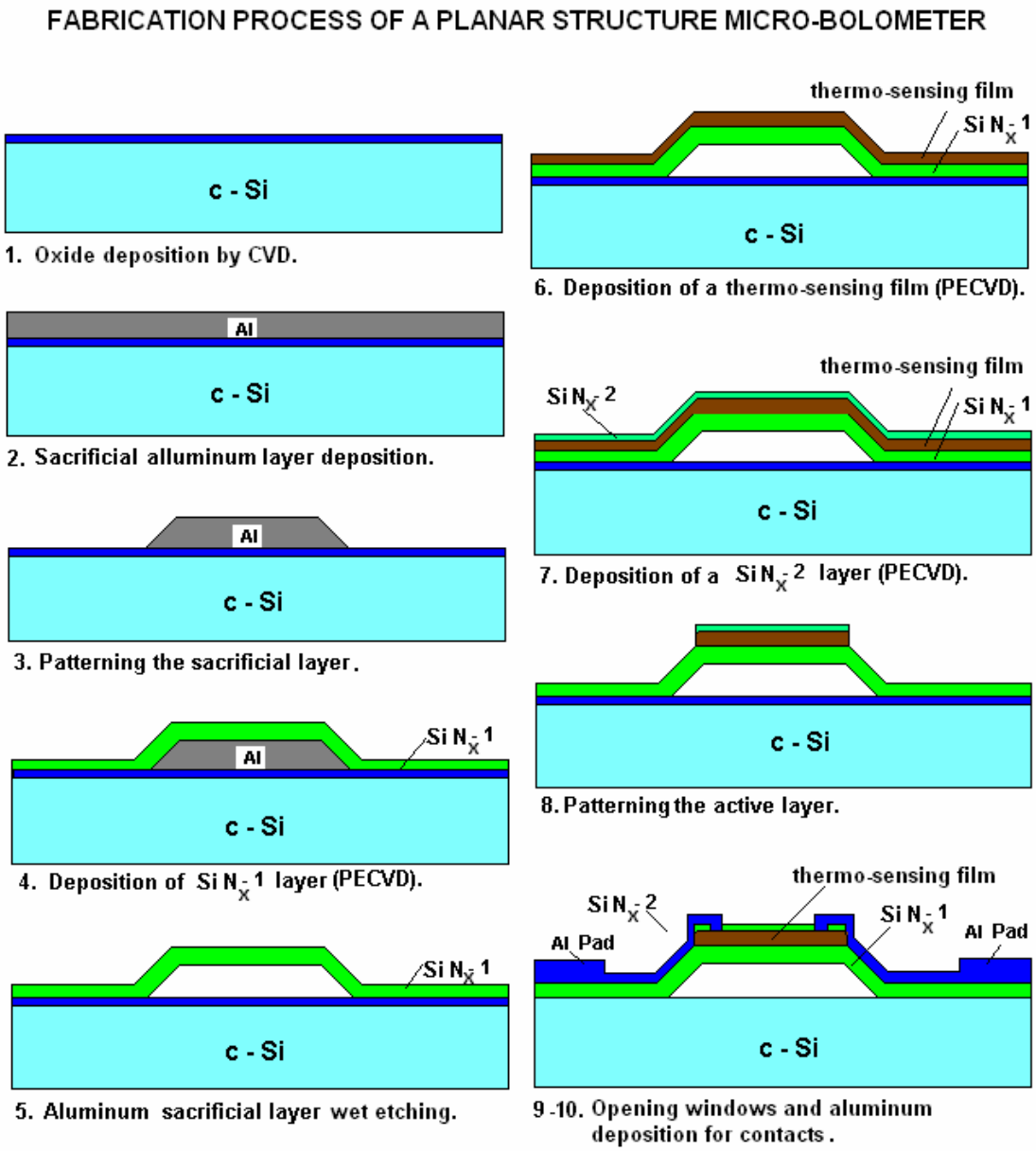

Figure 3.3. Previous process flow for the fabrication of a micro-bolometer at INAOE.

3.2.2 Deposition system

The system used for the deposition of thin films employed in the micro-bolometers, is a commercial low frequency PECVD (model AMP 3300 from Applied

Materials), Figure 3.4 shows the diagram of the LF PECVD system. The reactor consists of two 65 cm diameter parallel electrodes, separated by 5 cm; it can works at a variable RF power and variable frequency (f), but in this case a f = 110 KHz was used.

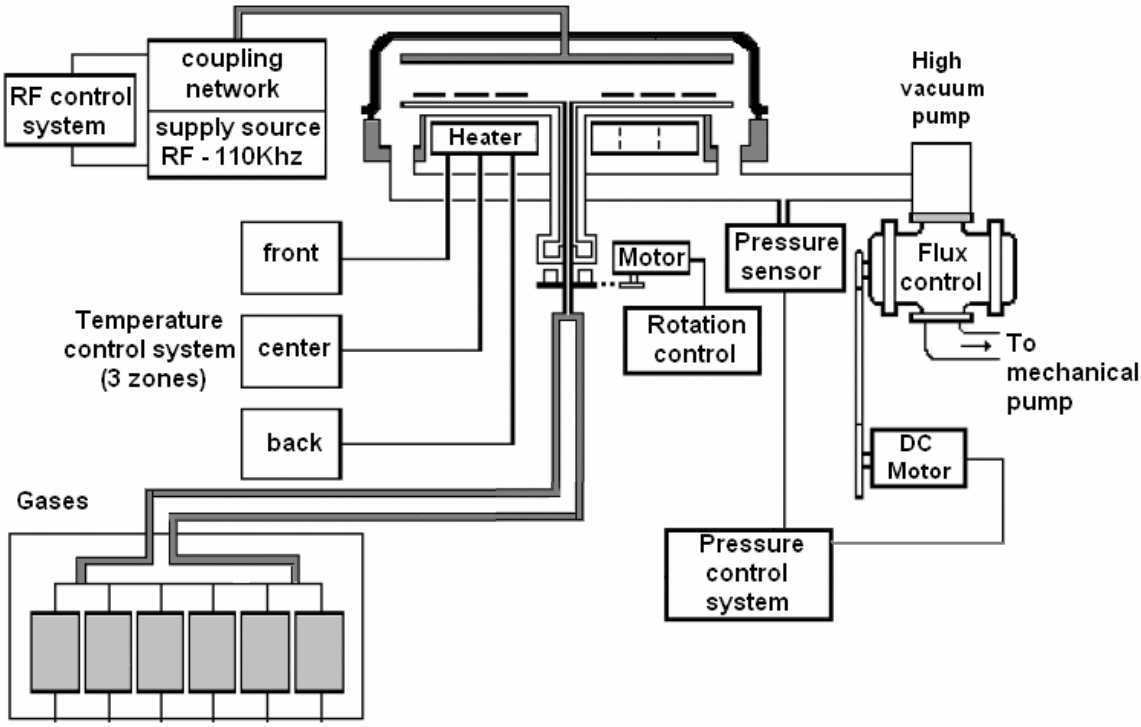

Figure 3.4. LF PECVD system employed for the deposition of thin films.

3.2.3 SiN_x supporting film.

Silicon nitride films obtained by LPCVD and PECVD are widely employed in MEMS technology due its mechanical properties. SiN_x films obtained by LPCVD from silane (SiH_4) and ammonia (NH_3) are stoichiometric (Si_3N_4), have low porosity, low hydrogen concentration and low etch rate, however they are deposited at relatively high temperatures (T = 700^{o}C) [1.12, 3.4 - 3.5].

For low temperature process SiN_x films deposited by PECVD are suitable since it can be deposited at temperatures as low as T = 350 ^{o}C, therefore they can be

employed in surface micro-machining for fabrication of MEMS structures over CMOS circuits. However, SiN_x films obtained by PECVD from SiH_4 and N_2, have larger porosity, higher etch rate and higher hydrogen concentration than those obtained by LPCVD and are not stoichiometric [1.12, 3.6].

In the work realized by R. Ambrosio [1.12] there were studied SiN_x films obtained by PECVD from SiH_4 and N_2 at different flow rates, SiH_4/N_2 = 0.5, 0.75 and 0.83 and there were studied their properties as refractive index, deposition rate and etch rate. In Table 3.1 are shown the deposition conditions of the SiN_x film (SiH_4/N_2 = 0.5) that will be employed as supporting film in the micro-bolometer arrays. In Table 3.2 are shown the properties of that film. The selection was made, taking into account the lowest etch rate and a refractive index n= 2.00, properties similar than those of the SiN_x films obtained by LPCVD.

Table 3.1. Deposition conditions of SiN_x films obtained by PECVD used as supporting film [1.12].

Process number	**Flow rates SiH_4/N_2 (sccm)**	**N_2 flow ratio, x**	**Substrate temperature T_d, (^oC)**	**Time (min.)**	**Thickness t_h, (µm)**	**Annealing time / temperature (min. / ^oC)**
386 [1.12]	100/100	0.5	350	30	0.8	30 / 300

Table 3.2. Properties of SiN_x films obtained by PECVD used as supporting film [1.12].

Process Number	**Deposition Rate, V_d, (Å/min.)**	**Etch rate in HF, V_e, (Å/min.)**	**Refractive index, n**	**[H] ($10^{22}cm^{-3}$)**
386 [1.12]	156	146	2.00	1.85

3.2.4 SiN_x absorbing film.

As IR absorbing film for micro-bolometers was employed also a SiN_x film. The deposition of this film over an a-Si_xGe_y:H film reduce their transmission

coefficient by a factor of 2, in the range of λ= 10-13 μm. In that range, the transmittance of the a-Si_xGe_y:H film is of 80%, while the transmittance in the a-Si_xGe_y:H + SiN_x is of 40% [1.12, 3.6]. Table 3.3 shows the deposition conditions of the SiN_x film (SiH_4/N_2 = 0.75) that will be employed as absorbing film in the micro-bolometer arrays, while Table 3.4 shows its properties.

Table 3.3. Deposition conditions of SiN_x films obtained by PECVD used as absorbing film in the micro-bolometer arrays [1.12, 3.6].

Process number	**Flow rates SiH_4/N_2 (sccm)**	**N_2 flow ratio, x**	**Substrate temperature T_d, (^oC)**	**Time (min.)**	**Thickness t_h, (μm)**	**Annealing time / temperature (min. / ^oC)**
387 [1.12]	100/300	0.75	350	10	0.2	30 / 300

Table 3.4. Properties of SiN_x films obtained by PECVD used as absorbing film [1.12, 3.6].

Process number	**Deposition Rate, V_d, (Å/min.)**	**Etch rate in HF, V_e, (Å/min.)**	**Refractive index, n**	**[H] ($10^{22}cm^{-3}$)**
387 [1.12]	252	189	2.16	1.29

3.2.5 a-Si_xGe_y:H thermo-sensing film.

In section 2.3.3 was described that intrinsic amorphous silicon (a-Si:H) prepared by PECVD is a material commonly used in micro-bolometers as thermo-sensing film. It presents a high activation energy, $E_a \approx 0.30$ eV and high value of temperature coefficient of resistance, TCR, $\alpha(T) \approx 0.039\ K^{-1}$, however it also presents a high undesirable resistivity.

Amorphous silicon-germanium (a-SiGe) films deposited by PECVD have been employed as thermo-sensing film in micro-bolometers [1.12, 2.17, 3.5, 3.7], due its high activation energy and consequently high TCR, and its relatively high room temperature conductivity, $\sigma_{RT,}$ in comparison with a-Si:H films.

In the a-SiGe films there is a compromise between E_a and room temperature conductivity, σ_{RT}. In the work performed by Y. Milagros [3.8] there were deposited several a-Si_xGe_y films obtained form SiH_4 and GeH_4 gas mixture, with different Ge gas content (x = 0.1, 0.2, 0.5 and 1) and different dilutions (Ar and H_2). From these films were extracted some parameters as E_a and σ_{RT} [1.12].

The larger activation energy was obtained in the a-SiGe:Ar (Ge_x = 0.1) films, $E_a \approx 0.6$ eV, however they also presented the smaller room temperature conductivity, $\sigma_{RT} \approx 5x10^{-8}\ \Omega^{-1}cm^{-1}$, while the a-Ge:Ar films presented the smaller $E_a \approx 0.21$ eV and the larger $\sigma_{RT} \approx 1.3x10^{-1}\ \Omega^{-1}cm^{-1}$.

From these results we selected one film with a relatively high E_a and σ_{RT}. Our choice for the film which will be employed in the micro-bolometer arrays as thermo-sensing is an a-SiGe:H (x= 0.5) film, its deposition parameters and some properties are shown in Table 3.5.

Table 3.5. Deposition parameters and properties of the a-SiGe film. that will be employed as thermo-sensing film in the micro-bolometer arrays [1.12, 3.8].

Dilution	**Process number**	**SiH_4/GeH_4 Flow ratio**	**Substrate temperature T_d, (^oC)**	**Time (min.)**	**Thickness t_h, (µm)**	**σ_{RT} ($\Omega^{-1}cm^{-1}$)**	**E_a (eV)**
a-SiGe:H	189 [3.8]	0.5	300	30	0.5	$2.1x10^{-3}$	0.29

With the information reviewed in this section, it is possible to improve the single cell micro-bolometers and design micro-bolometer arrays. The design of the modified cell micro-bolometers and arrays will be presented in chapter 4, section 4.3.

3.3. Methodology for characterization of thermo-sensing films

In this section it is described the characterization of thermo-sensing films included temperature dependence of electrical conductivity and estimation of the Thermal coefficient of resistance, TCR, compositional analysis by Secondary Ion

Mass spectroscopy, SIMS, and hydrogen bonding structure by Fourier Transform Infrared spectroscopy, FTIR.

3.3.1 Characterization of temperature dependence of conductivity in the films and estimation of Thermal coefficient of resistance, TCR.

Figure 3.5 shows the installation used for the characterization of the thermo-sensing films, it is a microprobe system (model LTMP-2, from "MMR technologies Inc."), which consist of a vacuum chamber, with a pump and micro-probes for characterization directly on the wafers. A temperature controller is used in order to vary the temperature in the wafer. The micro-probes are connected to an electrometer (model 6517-A, from "Keithley"). We employed this system for the estimation of the temperature dependence of conductivity in the thermo-sensing films.

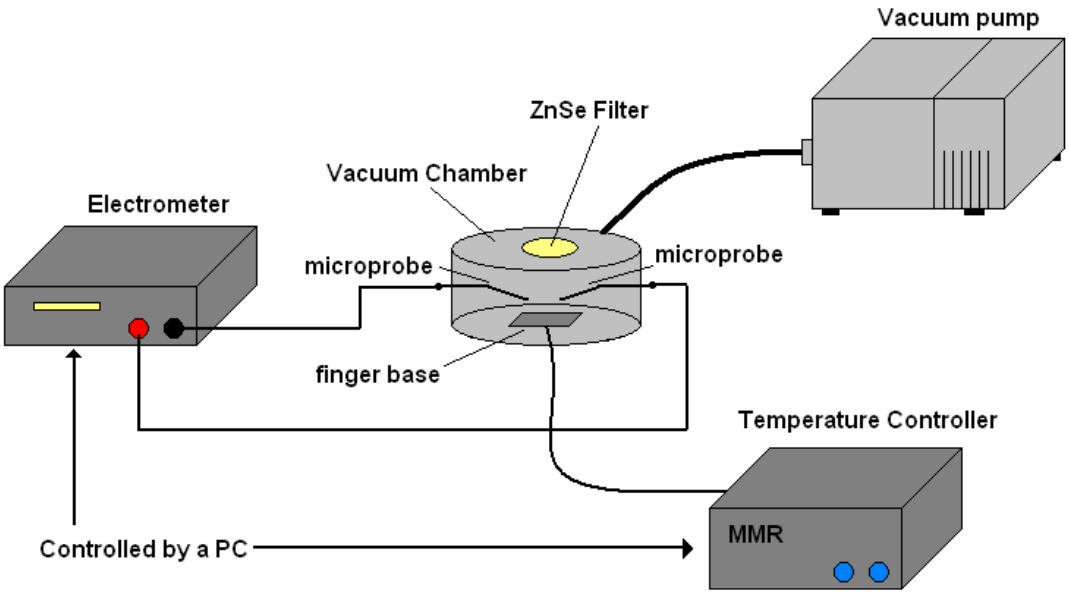

Figure 3.5 Installation for characterization of the thermo-sensing films.

The characterization consists of the measurement of current voltage I(U) characteristics in dark condition, in the thermo-sensing films at different

temperatures, employing an electrometer controlled by a PC and a temperature controller. The measurements were performed from T = 300 to 400 K.

In planar structures used for conductivity measurements we observed linear I(U) characteristics, suggesting that current is controlled by bulk properties rather than contacts. This allows us to use Ohm law to calculate resistivity. From I(U) measurements in the films we can calculate its conductivity, σ, by knowing its dimensions, L, W and thickness t_h, with Equation 3.1.

$$\sigma = \frac{J}{E} = \frac{\frac{I}{A_{Transversal}}}{\frac{V}{L}} = \frac{\frac{I}{W \cdot t_h}}{\frac{V}{L}} = \frac{I}{V} \cdot \frac{L}{W \cdot t_h} \qquad (3.1)$$

The conductivity is related to the activation energy E_a, by Equation 3.2, from this equation we can extract the E_a as is shown in Equation 3.3, which represents a line of the form y = a + bx. If the lnσ of the thermo-sensing film is plotted at different temperature values (T=300 – 400 K), then the E_a can be extracted by fitting a straight line and calculating its slope, as is shown in Figure 3.6.

$$\sigma = \sigma_o \exp\left(\frac{-E_a}{KT}\right) \qquad (3.2)$$

$$\ln\sigma = \ln\sigma_o - E_a \frac{1}{KT} \qquad (3.3)$$

The temperature coefficient of resistance is related with the E_a by Equation 3.4 (Equation 2.2 rewritten).

$$TCR = \alpha \approx -\frac{E_a}{KT^2} \qquad (3.4)$$

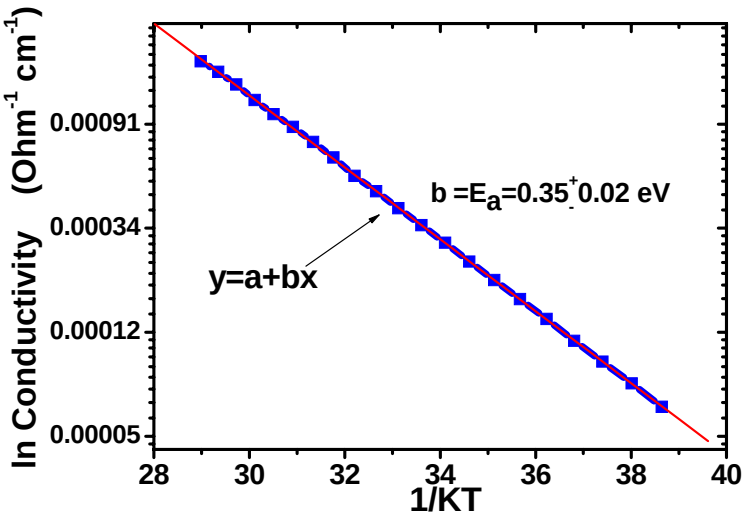

Figure 3.6. Conductivity dependence with temperature of an a-Si_xGe_y:H thermo-sensing film in a temperature range T= 300 - 400 K.

For the E_a = 0.35 eV obtained in the graph of Figure 3.6 the TCR calculates is $\alpha \approx -0.045$ (% K^{-1}).

3.3.2 Compositional analysis by Secondary Ion Mass Spectroscopy analysis (SIMS).

Secondary Ion Mass spectroscopy (SIMS) is a technique employed for the compositional analysis in solid materials, especially in thin solid films and semiconductors.

SIMS is performed by slowly sputtering the surface of a solid material by a primary ion beam (of few keV). The bombarding primary ion beam produces monoatomic and polyatomic particles of the sample material, along with electrons, photons and secondary particles: negative, positive and neutral charges with kinetic energies (from 0 to hundred eV) [3.9]. Primary beam species used in SIMS include Cs+, O, Ar+ and Ga+, at energies between 1 to 30 keV.

The secondary ions are analyzed by a mass spectrometer as is shown in Figure 3.7. The emission of the secondary ions supplies information of the elemental and molecular composition of the film uppermost atomic layers [3.10].

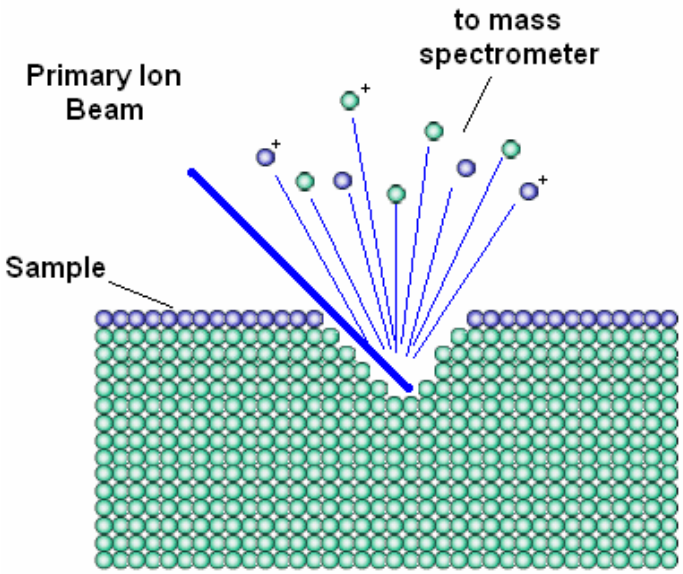

Figure 3.7. SIMS process.

There are two sputtering modes: Static SIMS occurs when the sputtering rate is extremely slow and the analysis can be performed in the firsts ten atomic monolayers, while Dynamic SIMS is employed for depth profiles, with a depth resolution between 1 to 20-30 nm.

The SIMS technique provides an extremely high sensitivity for all elements. This technique is destructive, since the material is sputtered, and it is applied to a variety of materials that can stay under vacuum, as metals, semiconductors and insulators.

The SIMS profiles of the a-Si_xGe_y films were measured with a Cameca IMS-6f ion microprobe. Sputtering during the SIMS process used a cesium ion beam with primary ion energy from 5 to 15 keV. The solid solution composition was analyzed with a special mode in which secondary ions CsM^+ (where M is the analyzed element), were monitored during cesium sputtering. Oxygen flooding was always

used with this mode in order to minimize the SIMS matrix effect found in SiGe compounds.

A SIMS profile of a sample composed of an a-Si_xGe_y:H film deposited over titanium (Ti) stripes is shown in Figure 3.8. The film was deposited by PECVD from SiH_4, GeH_4 and H_2 gas mixture. In Figure 3.7 we can see the time of sputtering and the density of atoms of different species as H_2, C, Si, Ti, Ge and B. Atoms of C and B were incorporated in the sample due to contamination in the chamber. From the atoms density values it can be calculated the percentage of the different atom species, calculating the total amount of atoms and then calculating the amount of each specie.

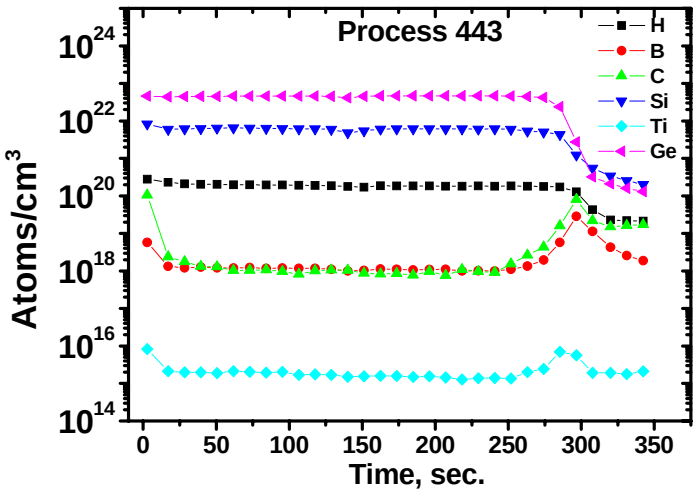

Figure 3.8. SIMS profile in an a-Si_xGe_y:H sample.

SIMS characterization in the films is performed by Dr. Y Kudriavtsev from CINVESTAV, Mexico DF.

3.3.3 Fourier Transform Infrared Spectroscopy (FTIR).

Fourier Transform Infrared Spectroscopy, FTIR, is a very useful technique in order to know the hydrogen bonding structure, as well as the hydrogen and oxygen

content in the thermo-sensing films. FTIR is a technique employed for the compositional analysis of materials organic or inorganic, in solid liquid and gas phase. This technique allows to identify and to quantify different types of chemical bonds in molecules of an unknown material mixture.

The FTIR operation is realized by passing a beam of IR light through the sample under study. The transmitted light is analyzed in order to reveal how much energy is transmitted or absorbed at each wavelength. By the use of a Fourier transform instrument is possible to produce an absorbance (or transmittance) spectrum, where the wavelengths at which the sample absorbs (or transmit) IR radiation are shown. The chemical bonds in a molecule can be determined, by interpreting the IR absorption spectrum. FTIR allows determine the Si-H and Ge-H bonds in the thermo-sensing a-Si_xGe_y:H films employed in the micro-bolometer arrays.

The films were analyzed with an FTIR (Model Vector 22, from Bruker). This equipment provides an absorbance (or transmittance) spectrum in arbitrary units in a data file, which can be processed with a specialized software. A complete guide of the obtaining of IR spectra in a-SiGe films, performed in our installation is found in reference [3.8].

3.4 Methodology for characterization of un-cooled micro-bolometers

As was described in section 2.3, a micro-bolometer is a resistor sensitive to temperature changes, its operation is based on the temperature increase of the thermo-sensing film by the absorption of the incident IR radiation. The change in temperature causes a change on its electrical resistance, which is measured by an external circuit. The methodology for characterization of un-cooled micro-bolometers is presented in this section.

3.4.1 I(U) measurements in dark and under Infrared radiation (IR).

In this section is described the procedure performed in order to obtain the current voltage I(U) characteristics of the micro-bolometers, from this measurement it is possible to determine the micro-bolometer electrical resistance and responsivity.

Figure 3.9 shows the installation used for the current voltage I(U) measurement in dark and under IR illumination conditions. The source of IR light is a SiC globar source (model LSH-GB GB from "Jobin Yvon"), which provides IR illumination in the range of λ=1 – 20 μm.

The samples were placed in a vacuum chamber at pressure P≈20 mTorr, at room temperature and illuminated through a zinc selenide window (ZnSe). The window has a 70% transmission in the range of λ=0.6 – 20 μm. The source of IR light is a SiC globar source, which provides intensity $I_0=5.3x10^{-2}$ W/cm^2 in the range of λ=1 – 20 μm.

The current was measured with an electrometer ("Keithley"- 6517-A) controlled by a PC (employing the LabView software) in dark and under IR illumination, from U=0 to 7 V.

The micro-bolometer electrical resistance can be calculated form Equation 3.5, where γ is the slope of the micro-bolometer I(U) characteristics, since the micro-bolometer it is not always an ohmic resistor resistor.

$$I = \frac{1}{R} V^{\gamma} \quad (3.5)$$

Figure 3.10 shows an I(U) curve obtained from an a-Si_xGe_y:H thermo-sensing film micro-bolometer. The insert in Figure 3.10 shows the same curve when plotted in a Log I (Log U) scale. Here we can see clearly the linear behavior of the micro-bolometer I(U) characteristics.

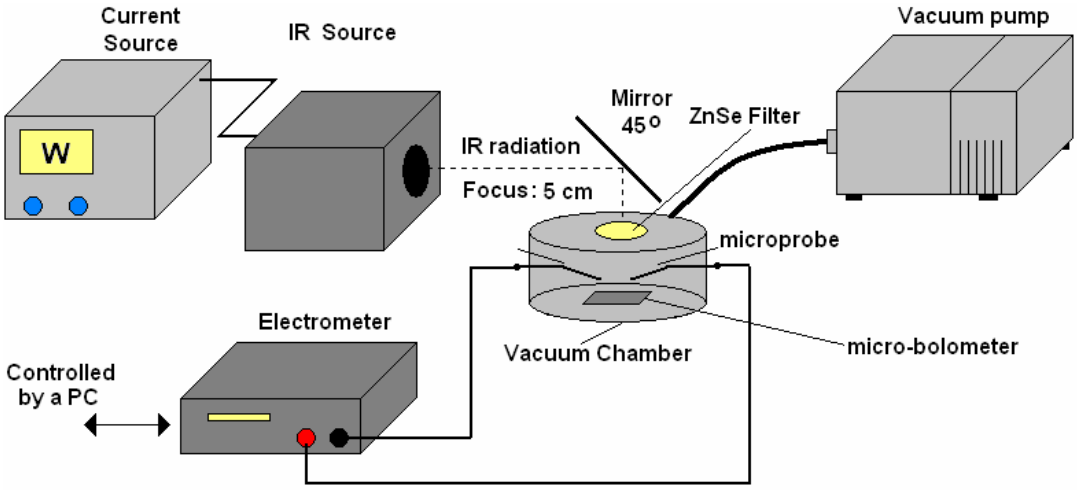

Figure 3.9. Installation employed for I(U) measurements in micro-bolometers.

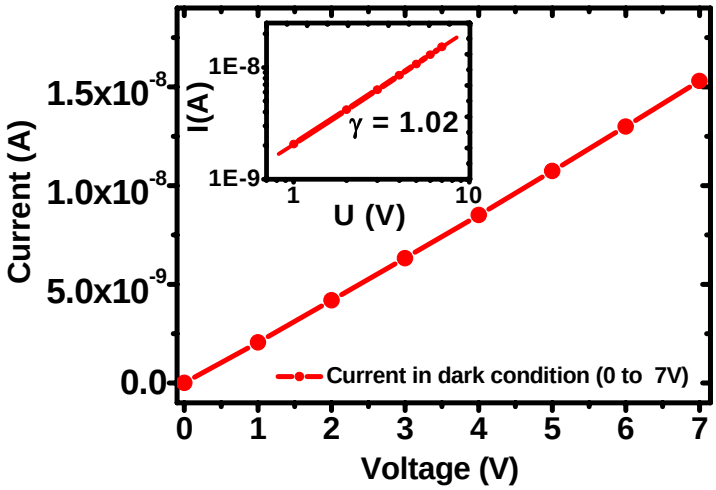

Figure 3.10. I(U) characteristics of a micro-bolometer (with an an a-Si_xGe_y:H).

3.4.2 Calculation of Responsivity.

The responsivity, *R*, is a figure of merit in detectors, it was defined in section 2.5.2 as the ratio between the output signal and the input signal. Under bias voltage, the output signal is the increment in current from dark condition to IR illumination

and the input signal is the incident radiant power on the detector surface. The set of Equations 3.6 – 3.8 describe how the current responsivity is calculated.

$$R_I = \frac{\Delta I}{P_{Incident}} \quad (3.6)$$

Where:

$$\Delta I = I_{IR} - I_{Dark} \quad (3.7)$$

$$P_{Incident} = A_{cell} \cdot I_0 \quad (3.8)$$

Equation 3.8 shows that the radiant power incident, $P_{incident}$, is equal to product of the micro-bolometer cell area, A_{cell}, by the IR source intensity, $I_{0.}$

I_0 was measured with a thermopile (Thermo "Oriel", model no.71938), which provides a transmission of 95% in the range of 0.13 to 11 μm. Equation 3.9 shows how I_0 was obtained, where R is the thermopile responsivity, R= 2.6x10^{-4} AW^{-1} and $A_{thermopile}$ is the thermopile area, $A_{thermopile}$ = 2.8 x10^{-3} cm^{-2}, data was taken from the thermopile data sheet. $I_{thermopile}$ is the thermopile current measured at a distance of 7cm form the IR source, $I_{thermopile}$ = 39x10^{-9} A, therefore I_0=5.3x10^{-2} Wcm^{-2}.

$$I_0 = \frac{I_{thermopile}}{R \cdot A_{thermopile}} \quad (3.9)$$

When the micro-bolometer operates under current bias, the output signal is the increment in voltage from dark condition to IR illumination, while the input signal is the incident radiant power on the detector surface. Equations 3.10 and 3.11 show the voltage responsivity, R_u.

$$R_U = \frac{\Delta U}{P_{Incident}} \quad (3.10)$$

$$\Delta U = U_{IR} - U_{Dark} \quad (3.11)$$

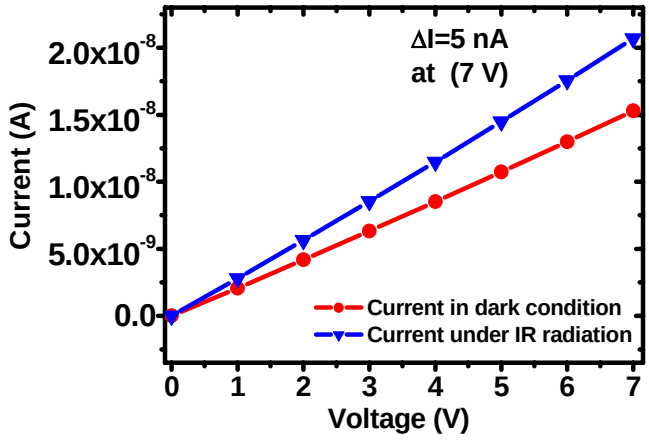

Figure 3.11. I(U) characteristics of a micro-bolometer (with an a-Si_xGe_y:H) in darkness and under IR illumination.

Figure 3.11 shows the I(U) characteristics in dark and under IR illumination in one micro-bolometer (with an a-Si_xGe_y:H film), where we can see the increment in current, ΔI.

3.4.3 Noise measurements.

In this section are presented the noise spectral density (NSD) measurements performed in the micro-bolometers. The NSD is defined as the noise per unit of bandwidth. Figure 3.12 shows the installation employed for noise measurements in the micro-bolometers. A lock-in amplifier ("Stanford Research Systems" - SR530) was used for this kind of measurements. The amplifier in the regime of noise measurements operates as true quadratic detector.

This equipment is used for measuring the voltage noise levels at different frequencies, for that purpose it has a reference input, where it is connected a sinusoidal function generator and also it contains a signal input, where the micro-

bolometer is connected. Since the micro-bolometer has a high resistance ($R_{bol} \approx 500$ MΩ), it was necessary the use of an impedance matcher, which is built of an operational amplifier (ultra low input current amplifier - model LMC6001) in a follower configuration (voltage gain ≈ 1).

The LMC6001 circuit has an ultra low input current noise of 0.13 fA/Hz$^{1/2}$, it can provide almost noiseless amplification of high resistance signal sources. It has a very high input impedance ($Z_{in} \approx 1$ TΩ) and a small output impedance, Z_{out}, compatible with the lock-in amplifier input impedance, Z_{in}. The micro-bolometer is in series with a load resistor R_L and is biased with a U=1.5 V battery.

The NSD of the system and the total NSD (system + cell) were measured separately, and a subtraction of both was made in order to obtain the micro-bolometer noise. Figure 3.13 shows the current noise spectral density in the system, $I_{system\ noise}$(f); in the system + the micro-bolometer (with an a-Si_xGe_y:H film), $I_{system\ +\ bolometer\ noise}$(f) and in the bolometer, $I_{bolometer\ noise}$ (f), which is obtained with Equation 3.12, taking into account the energetic addition of noise.

$$(I_{bolometer\ \ noise}(f))^2 = (I_{system+\ \ bolometer\ \ noise}(f))^2 - (I_{system\ \ noise}(f))^2 \qquad (3.12)$$

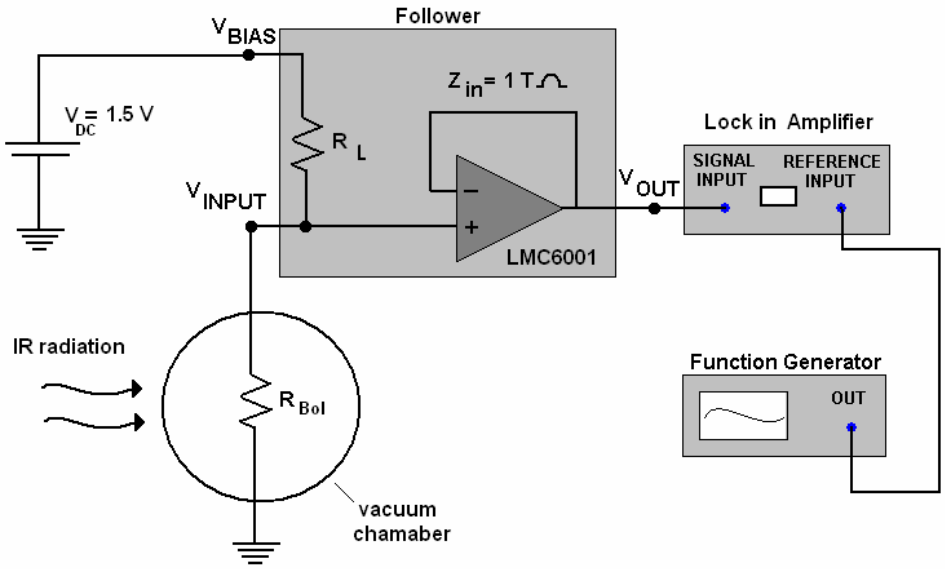

Figure 3.12. Installation for noise measurements in micro-bolometers.

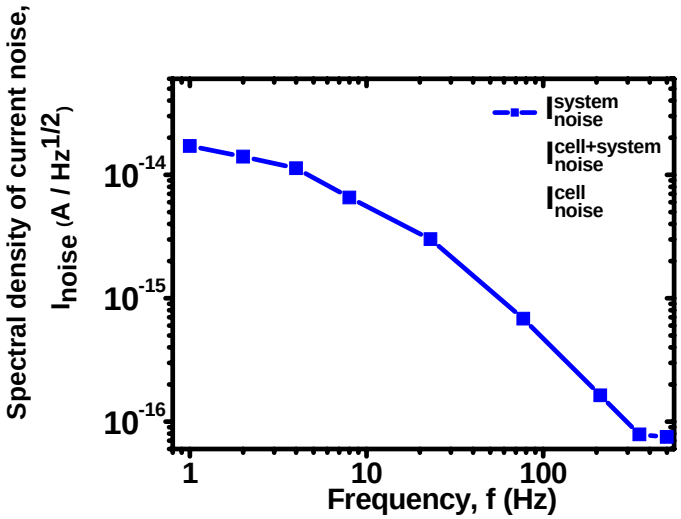

Figure 3.13. Spectral density of noise of one micro-bolometer (with an a-Si_xGe_y:H film).

The spectral density of current noise will be employed for the determination of detectivity.

3.4.4 Calculation of Detectivity.

Another figure of merit is the detecivity, D^*, which is shown in Equation 3.13, where R_I is the micro-bolometer current responsvity, A_{cell} is the micro-bolometer area, I_{noise} is the NSD in the micro-bolometer and Δf is the lock-in system bandwidth (set at $\Delta f = 1$). For the calculations the value of NSD used is at a frequency around 100 Hz.

$$D^* = \frac{R_I \cdot \sqrt{A_{cell}}}{I_{noise} / \sqrt{\Delta f}} \qquad (3.13)$$

The detectivity expresses one of the most important characteristics in detectors, which is the signal to noise ratio.

3.4.5 Thermal response time characterization.

The thermal time constant, τ_{th} of the micro-bolometer was determined employing the installation showed in Figure 3.14. A voltage pulse train is applied to the micro-bolometer by a function generator, through a load resistor, R_L, and the response current is measured by an oscilloscope. The impedance matcher circuit described in section 3.4.3 is employed in order to match the high micro-bolometer resistance with the oscilloscope input impedance.

Figure 3.15 shows a curve obtained from the thermal time measurements, we can observe a voltage pulse train, which is applied to the micro-bolometer and its response current, which has an increasing exponential behavior. The time necessary for achieve a steady state is the thermal time constant, in Figure 3.15 the thermal constant is around $\tau_{th} \approx 200$ msec.

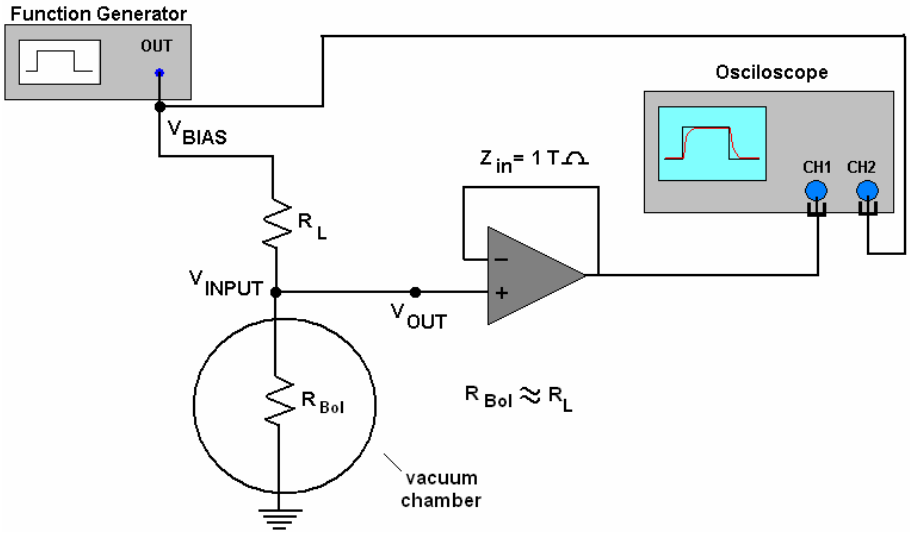

Figure 3.14. Installation for the micro-bolometer thermal time constant characterization.

The thermal time should be larger than the electrical time, τ_{elec}, which is the product of the coaxial cable capacitance ($C_{cable} \approx 10$ pF) used in the measurements, and the resistance of the micro-bolometer ($R_{cell} \approx 500$ MΩ). Therefore $\tau_{elec} \approx 5$ msec,

which is 2 orders smaller than the micro-bolometer thermal time, τ_{th}. In the case of micro-bolometers whit resistances as low as $R_{cell} \approx 100$ KΩ, the electrical time should be approximately $\tau_{elec} \approx 1$ μsec.

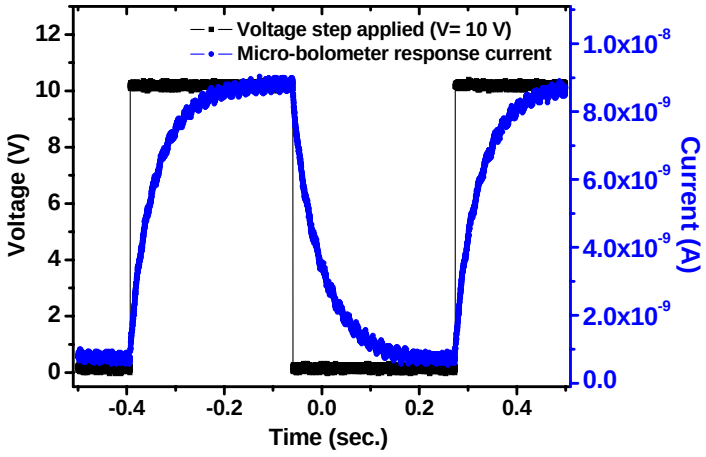

Figure 3.15. micro-bolometer thermal time constant

The thermal time constant, τ_{th}, is related with the thermal capacitance, C_{th} and the thermal conductance, G_{th}, by Equation 3.14 (Equation 2.5 rewritten).

$$\tau_{th} = \frac{C_{th}}{G_{th}} = C_{th} R_{th} \qquad (3.14)$$

In order to calculate C_{th} and G_{th}, the method described in the following section was used.

3.4.6 Thermal capacitance and conductance characterization.

We performed I(U) measurements in one micro-bolometer (with a-Si_xGe_y:H film) from U= 0 to 50 V, in order to see the self-heating in the device. Figure 3.16 shows the I(U) characteristics of that micro-bolometer. From I(U) measurements we re-plot resistance (U/I) vs. power (U*I) as is shown in Figure 3.17.

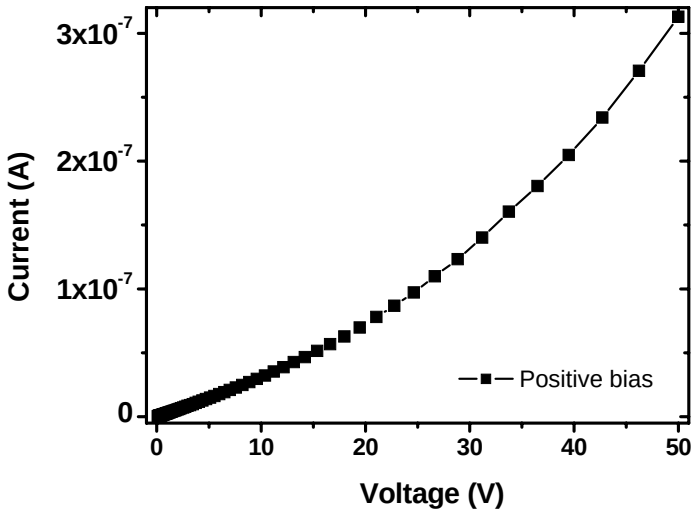

Figure 3.16. I(U) characteristic of the micro-bolometer from U= 0 to 50 V.

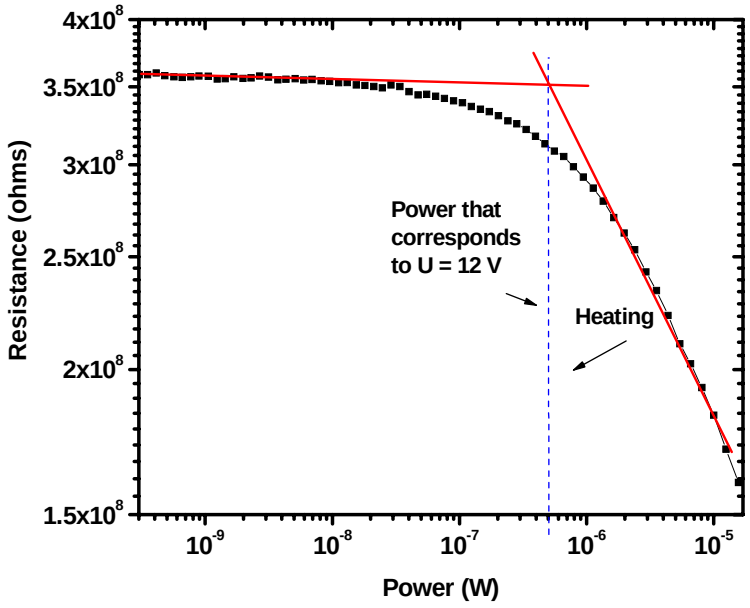

Figure 3.17. Resistance (U/I) vs. Power (U*I) of the micro-bolometer.

In Figure 3.17, the cone of the curve of resistivity vs. power corresponds to the power at which self heating will appear in the micro-bolometer due to the voltage

bias. The value of power P = 5x10^{-7} W corresponds to U=12 V, then with this bias (and larger) self-heating is present in the sample. If we take the I(U) experimental points before self-heating (i.e. points from 0 to 12 V) and plot I/U vs. I^2 , then we will get the curve shown in Fig. 3.18, If we fit this curve we will get a line in the form:

$$y = a + bx \qquad (3.14)$$

or:

$$\frac{I}{U} = \frac{1}{R_B} + \frac{E_a}{G_{th}} \cdot I^2 \qquad (3.15)$$

then:

$$a = \frac{1}{R_B} \quad \text{and} \quad b = \frac{E_a}{G_{th}} \qquad (3.16)$$

Where, R_B is the micro-bolometer resistance, G_{th} is its thermal conductance and E_a is the activation energy.

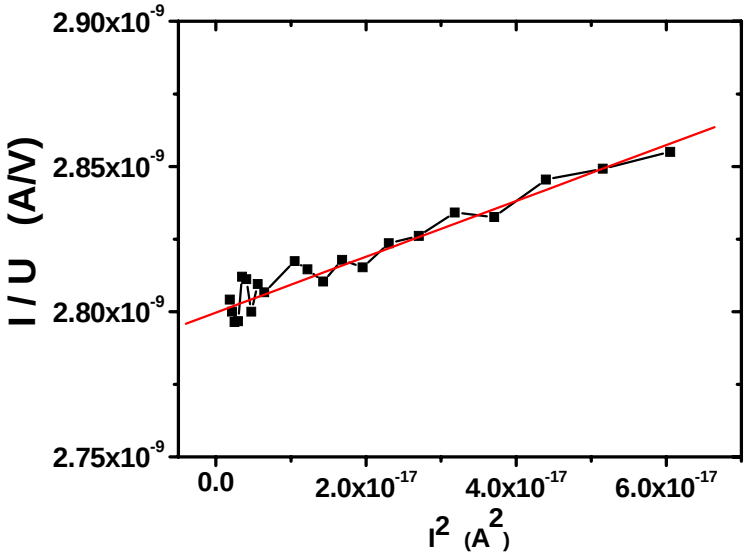

Figure 3.18. 1/Resistance (I/U) vs. Current^2 (I^2) of the micro-bolometer.

From the fitting of curve shown in Fig. 3.17 we got: $a = 2.7\text{x}10^{-9}$ and $b = 961265$. If the activation energy is $E_a = 0.34$ eV in this sample, it is possible to obtain the values of the G_{th} and R_{th}. In this particular case $G_{th} = E_a / b = 3.5\ \text{x}10^{-7}\ \text{WK}^{-1}$ and $R_B = 1/a = 370\text{x}10^6\ \Omega$.

From Equation 3.14 it is possible to obtain the thermal capacitance, C_{th}, knowing the thermal time constant, τ_{th}, and the thermal conductance, G_{th}. For example, if $\tau_{th} = 200$ msec. and $G_{th} = 3.5\ \text{x}10^{-7}\ \text{WK}^{-1}$ then the thermal conductance is $C_{th} = 7\text{x}10^{-8}\ \text{JK}^{-1}$. This method is relatively simple and its accuracy depends on how well the curves are fitting.

3.4.7 Temperature dependence of thermal resistance and calibration curve

In this section is presented the procedure followed in order to estimate the temperature dependence of thermal resistance in the micro-bolometers, this procedure is based on that performed in [3.5].

In the micro-bolometer, I(U) measurements are performed at different temperatures, as is shown in Figure 3.19. The linear part of these curves is used in order to obtain the electrical resistance in the micro-bolometers. With the data obtained is possible to graph the calibration curve of the device (Figure 3.20), which is a curve of the micro-bolometer resistance vs. temperature.

At high values of voltage bias, the increment of current in the micro-bolometer will result in a self heating of the device. From I(U) characteristics it is possible to extract the power, P (W), dissipated by the micro-bolometer.

By combining the data of the I(U) characteristics (Figure 3.19) and the calibration curve (Figure 3.20), it is possible to extract the increment in temperature (ΔT) by the power ($P=U*I$) applied to the micro-bolometer, for each temperature, as is shown in Figure 3.21.

The thermal resistance, R_{th}, is obtained as the slope of the ΔT vs. P curves, for each temperature. Figure 3.22 shows the dependence of R_{th} with temperature.

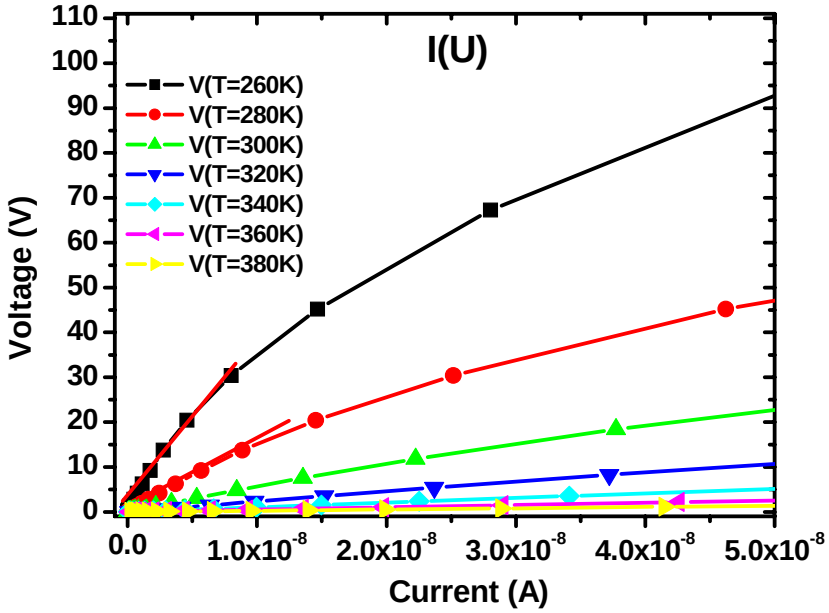

Figure 3.19. U(I) curves of one micro-bolometer at different temperatures.

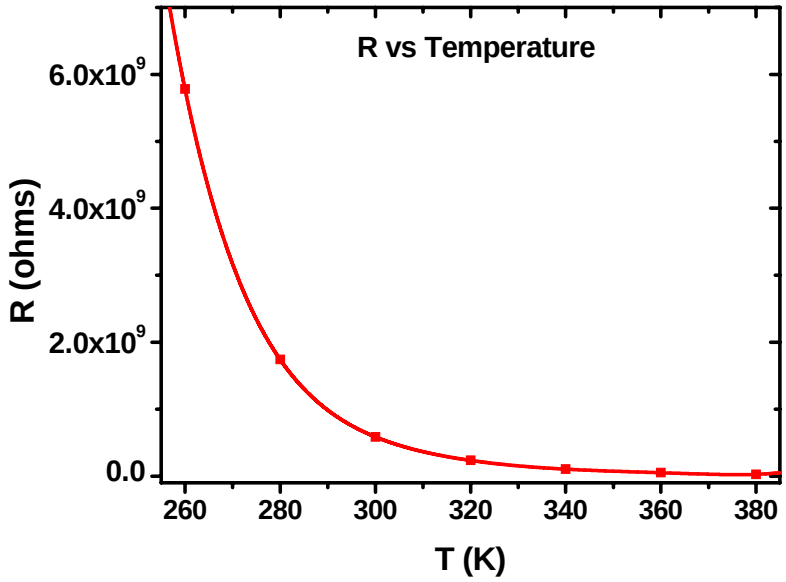

Figure 3.20. Calibration curve of one micro-bolometer.

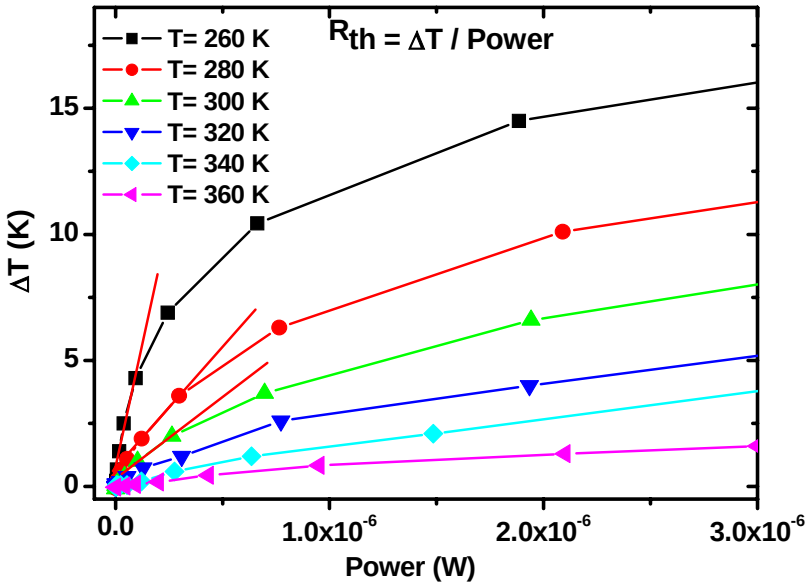

Figure 3.21. Thermal resistance extracted from ΔT vs Power curve.

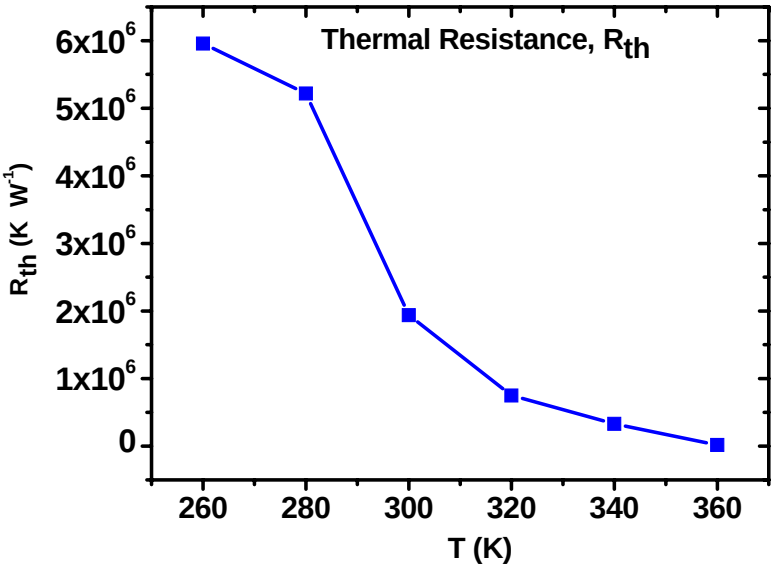

Figure 3.22. Thermal resistance of one micro-bolometer.

Figure 3.22 shows the temperature dependence of the R_{th} of the micro-bolometer, R_{th} decreases as the temperature of the micro-bolometer increases.

3.5 Methodology for characterization of un-cooled micro-bolometer arrays

In this section is presented the characterization performed in the arrays, which consisted of I(U) characterization in dark and under IR, in every cell in the arrays, employing an experimental readout described in section 3.5.1, also responsivity and detectivity values were determined in the cells of the arrays. The yield in the arrays was obtained from I(U) measurements.

3.5.1 Experimental Readout circuit for the arrays

For characterization, the 1-D arrays were encapsulated in a 40 legs Dual Encapsulated Package – DIP (Model CSB04075, from "Spectrum Semiconductor Materials"). For the encapsulation procedure we employed an "ultrasonic bonder" and a 20 μm diameter wire (silicon, magnesium - 1% alloy).

Figure 3.23 shows the installation used for the 1-D micro-bolometer arrays characterization. The arrays encapsulated were placed in a vacuum thermostat (Model MTD-150, from "LakeShore") special for IC DIPs (from 2 to 40 legs), where every leg has an external coaxial connection. The thermostat has a zinc selenide window (ZnSe) with a transmission of 70% in the range of λ=0.6–20 μm. Measurements were performed at pressure P≈20 mTorr and at room temperature. For the IR illumination we used a SiC globar source, with an intensity $I_0=5.3x10^{-2}$ W/cm^2 and spectrum in the range λ=1–20 μm.

We employed an experimental external readout circuit composed of a multiple switching matrix ("Keithley – 707"), an electrometer ("Keithley – 6517-A") and a PC.

The multiple switching matrix can contain up to 5 isolated coaxial matrix cards ("Keithley –7077"). Each coaxial matrix card has 8 rows (A to H) and 12 columns (1-12). Then the multiple switching matrix can contain 8 rows and 60 columns, each intersection of a column with a row is a switch, the equipment when is controlled by a computer can open and close those switches. Every row and column

has an external coaxial connection. Generally the columns are connected to the devices to be tested and the rows are connected to the equipment for polarization and measurements. In our installation the multiple switching matrix (707) contains 2 switching matrix cards (7077), therefore the multiple switching matrix can work with 8 rows (A – H) and 24 columns (1 – 24), this limit the number of cells in the micro-bolometer array that can be tested.

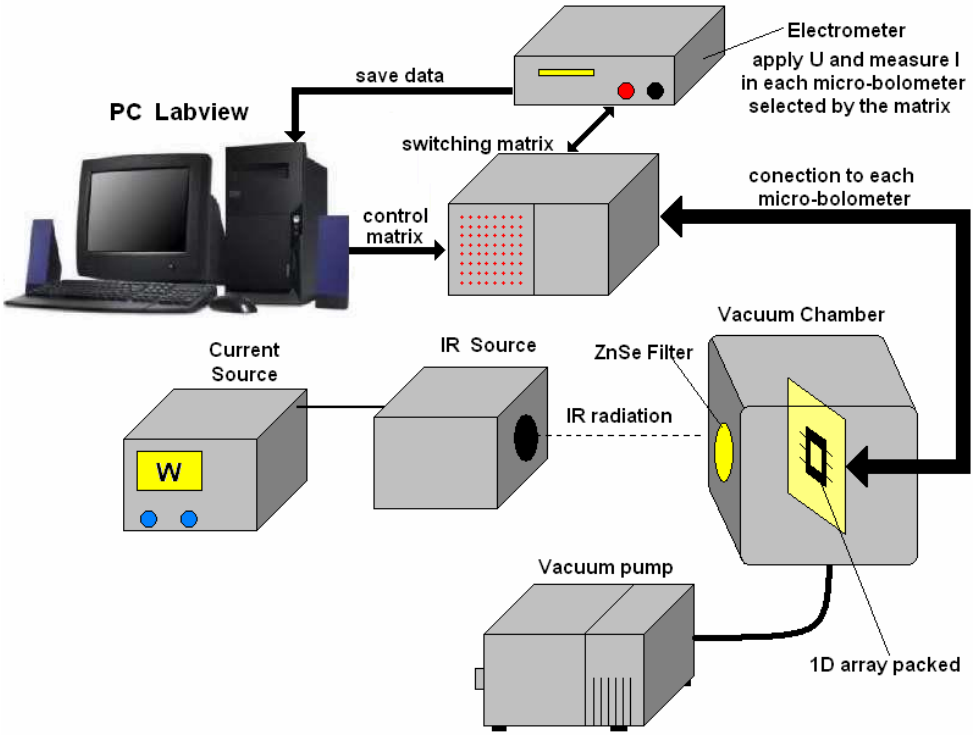

Figure 3.23. Installation used for 1-D arrays characterization.

Each column of the switching matrix is connected to one micro-bolometer leg and one column is connected to the array common node, therefore the number of micro-bolometers connected is limited to 23. In rows A and B is connected the electrometer, which acts as voltage source and also as an ammeter. Figure 3.24 shows a simplified diagram of the readout circuit, which operates in the following way: A PC with a “Labview” program designed especially for this application, controls the

switching matrix card and allows to apply a voltage pulse sequentially to each micro-bolometer in the array employing the electrometer as voltage source, and at the same time the electrometer measure the current in the micro-bolometer.

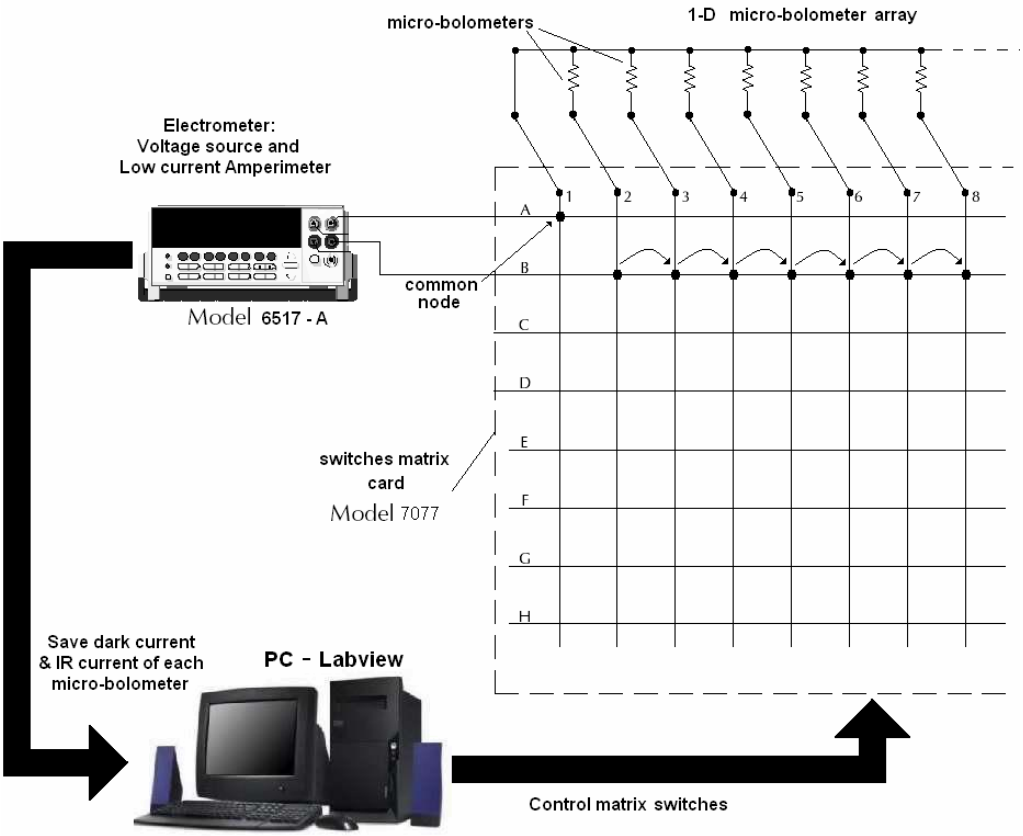

Figure 3.24. Simplified readout schema.

The frequency of the pulse, the voltage amplitude and the time between pulses can be controlled. At the end of the measurements the current values of all micro-bolometers are saved in a data file, which is further used to perform the analysis.

3.5.2 Current – Voltage I(U) measurements in the arrays.

We performed current-voltage I(U) measurements in the arrays, in dark and under IR illumination. With the experimental readout circuit we applied a voltage

pulse sequentially to each micro-bolometer in the 1-D arrays and saved the current for each pulse in a data file. The voltage pulse applied to each micro-bolometer has an amplitude variable in the range of U = 1- 50 V, a pulse duration variable, in the range t = 200 msec - 10 sec. and a time between voltage pulses also variable in the range t = 200 msec - 10 sec. Typical values employed are a pulse amplitude U = 7 V (at this value self heating is not presented in the micro-bolometer), a pulse duration t = 500 msec. and a time between voltage pulses t = 500 msec.

The readout installation employed has the limitation of 23 cells that can be tested, as was discussed in the previous section. Figure 3.25 shows an example of the current values I(U) obtained in each cell of one micro-bolometer array when a voltage pulse U=7V is applied.

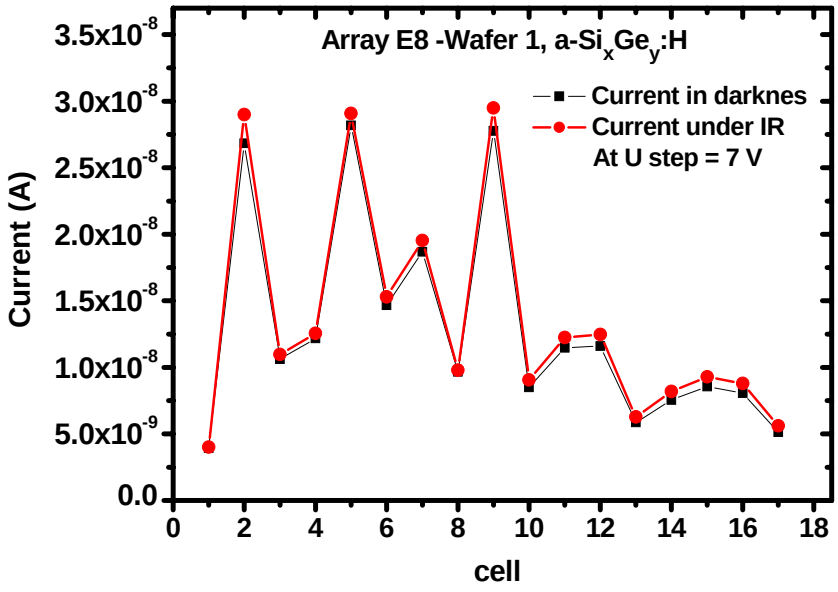

Figure 3.25. I(U) values in every cell of one array, when a U pulse is applied, employing the experimental read-out.

Employing the values of current in dark and under IR radiation, it is possible to calculate the values of responsivity in the cells of the arrays, as it was made for single micro-bolometers. The yield in the arrays was estimated from I(U)

measurements in every cell of the arrays. Thus only the cells that conduce current are taken into account for the yield estimation.

3.5.3 Responsivity calculations in the arrays.

The responsivity values in the cells of the arrays characterized, are obtained performing I(U) measurements with the read-out circuit in dark and under IR illumination. Employing the method described in section 3.4.2, were obtained the responsivity values of every cell in the array. Figure 3.26 shows an example of the values of responsivity obtained from the array I(U) results.

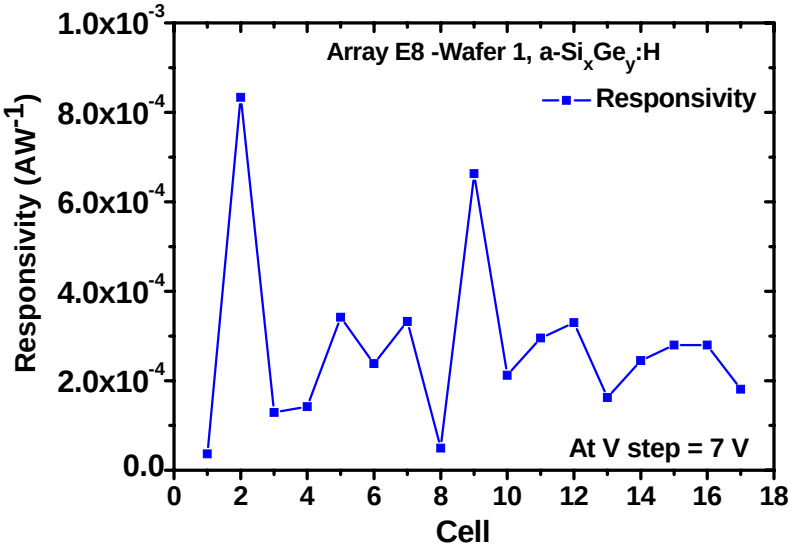

Figure 3.26. Responsivity values in every cell of one micro-bolometer array, obtained from the I(U) results of figure 3.25.

The values of responsivity of Figure 3.26, are employed for the calculations of the detectivity values in every cell in the arrays.

3.5.4 Noise and detectivity in the arrays.

The detectivity values in the cells are calculated employing the method described in section 3.4.4. For this calculation is necessary to know the noise in every cell (as was described in section 3.4.3), however noise measurements are a complex task and was not possible measure the noise in every cell of the array.

Therefore for the detectivity calculations we employed an average spectral density of current noise, I_{noise} obtained in three different cells. For the micro-bolometer array with an a.Si_xGe_y:H film of Figure 3.25 we obtained an average $I_{noise} \approx 1x10^{-15}$ $AHz^{-1/2}$. Figure 3.27 shows an example of the detectivity values of the micro-bolometer array.

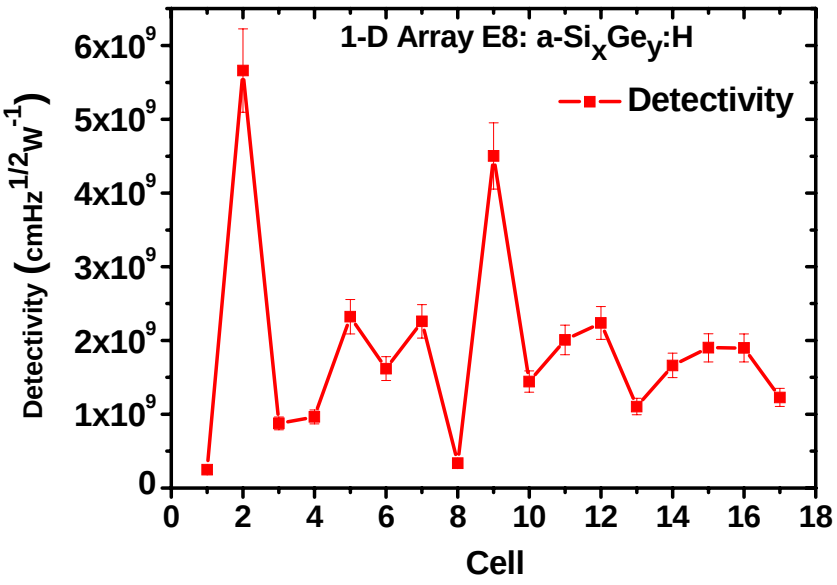

Figure 3.27. Detectivity values in every cell of one micro-bolometer array, obtained from the I(U) results of figure 3.25.

The characterization described in this section is performed with the equipment available in the micro-electronics lab at INAOE. In order to perform a better characterization a black body is required, as well as more modules of isolated coaxial

matrix cards ("Keithley –7077"), which will allow to work with more micro-bolometer cells in the array.

3.5.5 Specific characteristics of arrays: 1-D image and crosstalk

In order to obtain a simple one dimensional image with a 1-D array, we cover one half of the array with a mask composed of a an Al foil + a dielectric plastic, and performed I(U) measurements in dark and under IR radiation in every cell of the array using the experimental readout, as was described in sections 3.5.1 and 3.5.2.

The dark current is subtracted from the IR current in every cell of the array in order to see the difference in response between two regions in the array (one region covered with a mask and the other without a mask).

Electrical crosstalk was measured in the arrays in DC regime. A variable voltage bias is applied to one micro-bolometer (U = 0.5, 1, 2,…10 V) and is measured the current in the neighbors micro-bolometers that are next to it. In order to measure the current in the neighbors micro-bolometers, they are biased with a voltage step of U=0.5 V.

3.6 Conclusions

In the present chapter, the design and fabrication of un-cooled micro-bolometers, work performed in previous work has been studied [1.12]. The different methods for characterization of the thermo-sensing films employed in the micro-bolometer arrays had been described as well as the electrical characterization performed in the micro-bolometer cells and the micro-bolometer arrays.

3.7 References of chapter 3

[3.1] M. García "Characterization and Modeling of uncooled microbolometers of a-SiGe" PhD. Thesis, INAOE, 2006.

[3.2] R. Ambrosio, A. Torres, A Kosarev, A. Heredia, M. Garcia, M. Landa, "Amorphous $Si_{1-x}GeH_x$:H films obtained by LF PECVD for uncooled microbolometers", Mat. Res. Symp., Vol. 808, pp. A4.29.1-A4.29.6, 2004.

[3.3] M. Garcia, A. Torres, A. Kosarev and R. Ambrosio, "IR bolometers based on amorphous silicon germanium alloys " *J. Non-cryst. Solids*, vol. 338 - 340, pp. 744 – 748, 2004.

[3.4] G. Parson, J. Souk, and J. BAtey, "Low hydrogen content stoichiometric silicon nitride films deposited by plasma-enhanced chemical vapor deposition", J. Appl. Phys., Vol. 70, pp. 1553 – 1560, 1991.

[3.5] A. Heredia, "Fabricación y Caracterización de un Bolómetro, Utilizando una película de a-Si:H dopada con Boro, para la detección de IR en el rango de los milímetros", Tesis de doctorado, INAOE, 2004.

[3.6] R. Ambrosio, A. Torres, A Kosarev, A. Heredia, M. Garcia, M. Landa "Effect of the hydrogen content in the optical properties and etching of silicon nitride films deposited by PECVD for uncooled microbolometers", Mat. Res. Symp., Vol. 862, pp. A9.6.1-A9.6.6, 2005.

[3.7] R. Ambrosio, A. Torres, A. Kosarev, C. Zúñiga, A. S. Abramov, "Silicon Germanium Films Prepared from SiH_4 and GeF_4 by Low Frequency Plasma Deposition"*J. Non-cryst. Solids*, vol. 329, p.p. 134-139, 2003.

[3.8] Y. Hernandez "Estudio de las propiedades electrónicas de películas de Si1-xGex depositadas por plasma a bajas frecuencias" Tesis de Maestria, INAOE, 2003.

[3.9] A. Benninghoven, F.G. Rudenauer, and H. W. Werner, "Secondary Ion Mass Spectroscopy: Basic concepts, Instrumental Aspects, Applications and Trends", Wiley, New York, 1987.

[3.10] http://www.cameca.fr/html/sims_technique.html. (November 2007).

CHAPTER 4. EXPERIMENTAL RESULTS

4.1 Introduction

This chapter presents the design of micro-bolometers arrays and the results obtained from the experimental work realized in fabrication and characterization. We started with the selection of the cell (from the previous work [1.12, 3.1]) for the development of micro-bolometer arrays. The design of the cell and the fabrication process flow were modified in order to increase the yield at the end of the fabrication process and to obtain a better cell performance characteristics.

4.2 Cell configuration selection for arrays.

Our first task was to analyze the yield of devices and its correlation with the micro-bolometer (cell) configuration and fabrication, in order to select the best micro-bolometer cell in terms of yield and responsivity, at the end of the fabrication process, from 22 different types of cells available. The cell configuration with the largest yield and responsivity would be the base for the design of arrays.

For that purpose, we selected one wafer (process #328 – fabricated by R. Ambrosio) which contained 49 dies and each die contained 22 different cells (each cell was labeled with a letter followed with a number i.e. A1, A2, etc.). With an optical microscope, we performed an optical inspection of the cells structures in the 49 dies in order to determine which types of cell configurations had structural damage during the fabrication process.

Figure 4.1 shows a top-view of one micro-bolometer structure, we can see that it is broken in the bridge edges an also in the thermo-sensing film, resulting in a device in open circuit, so it is considered as a micro-bolometer in “bad conditions”. Figure 4.2 shows a top view of a micro-bolometer which is considered in “good conditions” since it does not have any rupture in it structure, those devices were considered for yield calculations.

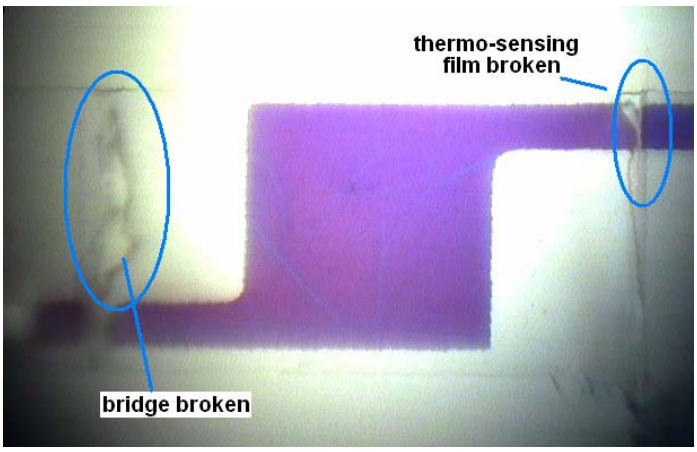

Figure 4.1. Top view of a micro-bolometer in bad conditions after fabrication.

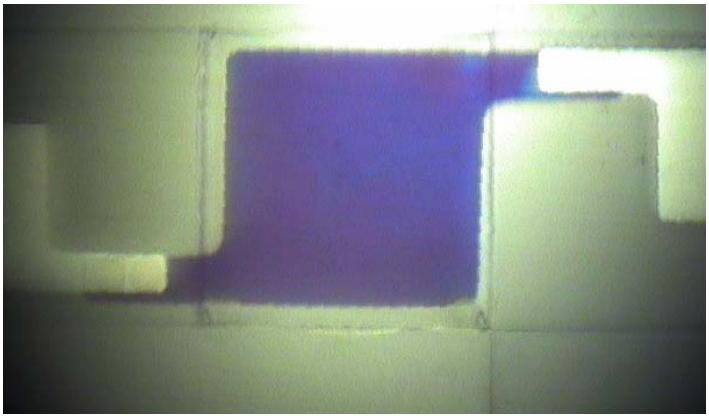

Figure 4.2. Top view of a micro-bolometer in good conditions after fabrication.

The results of the observation of 1078 cells in an optical microscope are shown in Figure 4.3. In the figure we can see the percentage of micro-bolometer cells in good conditions, of the 22 different types available.

Since the yield of the samples is obtained from optical inspection we call it "optical yield", this is an estimation of real yield were all the samples should be electrically tested.

In Table 4.1 are indicated the cell structures with the largest and lowest yield. We identified 3 different structures with more than 50 % of yield: B3, G3 and C4; these structures are the most suitable for the development of micro-bolometer arrays in terms of yield after fabrication.

The cells with the lowest yield are C2, C3, and G4, those cells give some insights on what kind of elements of the cell configuration could be responsible for the yield reduction.

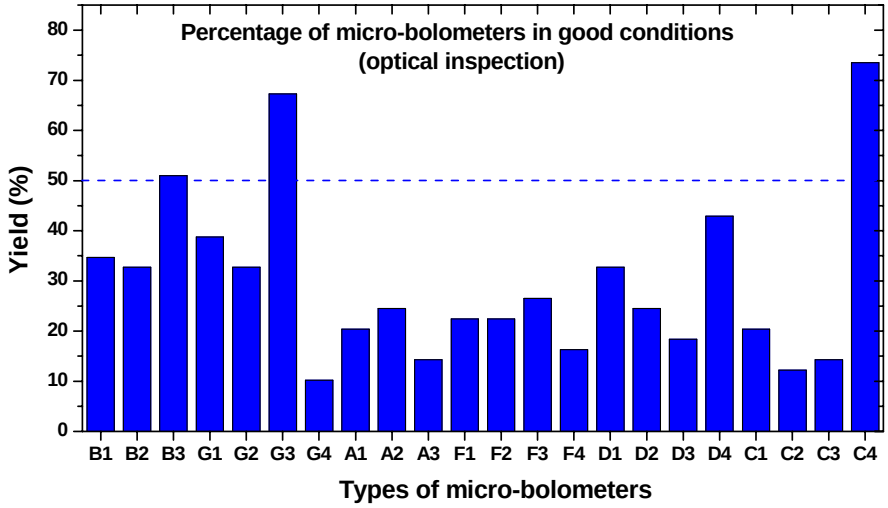

Figure 4.3. Yield of micro-bolometers in good conditions after the fabrication process.

In order to understand the yield correlation with the device configuration, we studied the micro-bolometer structures with the largest and lowest yield. Figure 4.4 shows the micro-bolometer structures with the lowest yield (G4, C2 and C3). We observed that a common characteristic in these structures is that the aluminum lines (that come from the pad) make contact with the thermo-sensing film at the top of the bridge. The main problem encountered in these devices is that the aluminum lines are broken when they climb the bridge.

Figure 4.5 shows the micro-bolometer structures with the largest yield (B3, G3 and C4). The common characteristic of these structures is that the thermo-sensing film at the top of the bridge comes down and makes contact with the aluminum pads, either with thin film lines (as in B3 and G3 structures) or with the complete film (as in C4).

Table 4.1. Results of the observation of the samples in the optical microscope.

	Artículo I. **WAFER D - Process # 328**		
Examined structures	1078		
Devices in good-conditions	320		
Percentage of good devices	29.7 %		
Cell configurations with more than 50% of yield.	**C4 – 70 % (best)**	G3 – 67 %	B3 – 51 %
Cell configurations with less than 15% of yield.	**G4 – 10 % (worst)**	C2 – 12 %	C3 – 14 %

Therefore is more common a rupture in the metal lines when they climb the bridge (resulting in low yield devices), than a rupture in the thermo-sensing film when it goes down from the bridge and make contact with the metal pads (resulting in larger yield devices).

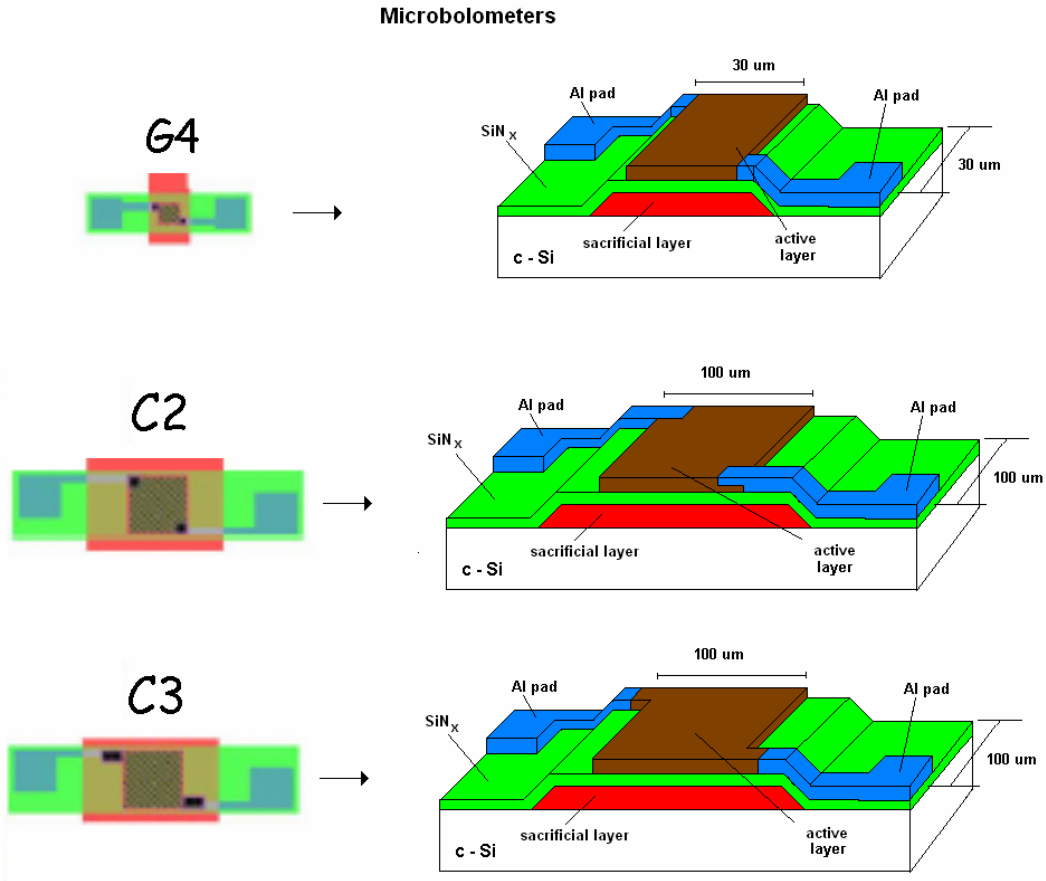

Figure 4.4. Micro-bolometer configurations with the lowest yield.

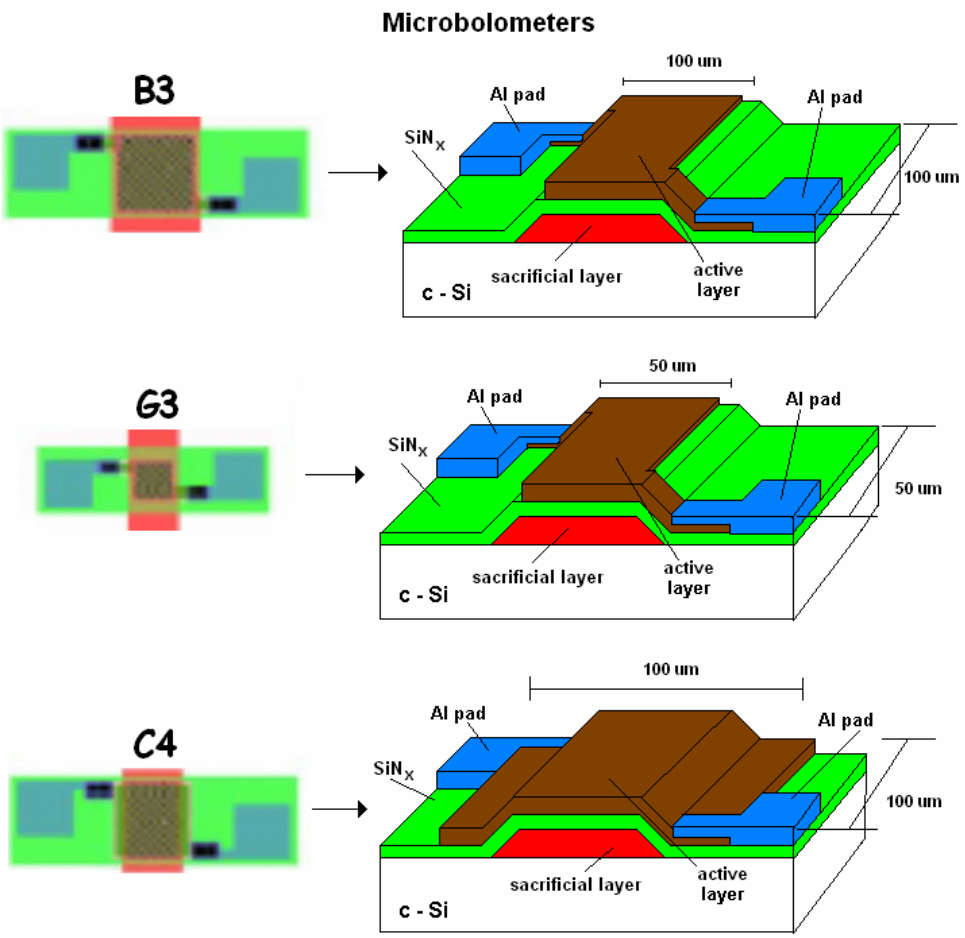

Figure 4.5. Micro-bolometer structures with largest yield.

Table 4.2. Responsivity the structures with the largest yield.

Type of Cell	Current Responsivity (AW^{-1})
B3 (best)	**6×10^{-4}**
C4	1.5×10^{-4}
G3	3.5×10^{-4}

Once that the structures with the largest yield were found, it was necessary to select one of them in order to use it as cell in the micro-bolometer arrays. The selection of the cell was taking into account the micro-bolometer responsivity. We measured the current in dark and under IR radiation at ambient pressure in 5 cells of

each type of the B3, C4 and G3 structures and calculated the current responsivity. The average responsivity is showed in Table 4.2. We found that the B3 type configuration present the larger responsivity; therefore this micro-bolometer structure is our choice in order to be used as cell in the arrays due to its high yield (51%) at the end of the fabrication process and its larger responsivity.

4.3 Design of micro-bolometers.

The micro-bolometers studied in section 4.2 are labeled planar structure micro-bolometers, since in that configuration the metal electrodes are deposited over the thermo-sensing film. We studied the cell structure B3 in order to make some changes in its design and fabrication process flow, with the purpose of increasing the yield and to improve the cell performance characteristics.

4.3.1 Design of the modified planar structure micro-bolometer and process flow.

In section 3.2.1 was described the previously process developed flow for a micro-bolometer fabrication. In that process, there are some critical steps that can be improved in order to increase the yield and the device performance characteristics. Those steps are numbered and the solutions proposed are listed in Table 4.3.

Table 4.3 Critical steps in the fabrication process of planar micro-bolometers.

	Critical Step	**Solution Proposed**
1.	Patterning the SiN_x micro-bridge with RIE (step no. 4 of process flow described in section 3.2.1). One lithographic step (micro-bridge mask) and dry etching (RIE) in order to pattern the SiN_x micro-bridges. We observed that the photo-resist used for protect the bridges does not remains the total time of etching, so both, the photo-resist and the SiN are etched. The latter is supposed to be protected by the photo-resist, but is etched too.	The solution is to divide this step in two, performing the lithographic step once and etching the SiN_x half of the total etching time needed, and then repeat again the lithographic step; by doing this we avoid to over etch the SiN_x micro-bridges.

2.	Etching of the aluminum (Al) sacrificial layer (step no. 5). At the middle of the process flow the Al sacrificial layer is etched, we found that some bridges could be broken in the following steps (layers deposition, lithographic steps), resulting in a decrease in the yield.	Etching the Al sacrificial layer at the end of the process flow. Titanium (Ti) for contacts (instead of Al), allow us to remove with high selectivity the Al sacrificial layer at the end of the process, since the Al etchant does not attack Ti.
3.	Patterning the active area with RIE (step no. 8). This step consist of one lithographic step (using the active area mask) and dry etching (RIE) in order to pattern the active area. The photo-resist used to protect the active area does not resist the total time for etching, so both, the photo-resist and the SiN + a-Si_xGe_y:H are etched. The latter is supposed to be protected by the photo-resist.	Dividing this step in two, performing one lithographic step and etching the SiN_x + a-Si_xGe_y:H unprotected by the photo-resist, half of the total time needed, and then repeat the lithographic step. In order to avoid to over etching the SiN_x + a-Si_xGe_y:H films of the active area.
4.	Windows opening in the second layer of SiN_x and deposition of Al contacts (step no. 9 and 10). In step 9 is carried out one lithographic step and dry etching (RIE) in order to open windows in the upper SiN_x. In step 10 another lithographic step is carried out and Al is deposited over the windows in order to form contacts with the thermo-sensing film. If the upper SiN_x is not completely eliminated in order to open a window, then when the Al for contacts be deposited, the interface metal-semiconductor will have an intermediate dielectric layer, which reduce current and responsivity.	With Ti (instead of Al) for contacts, we can fabricate the contact metal - semiconductor in a different way. After patterning the SiN_x bridge (step 4) we can deposit Ti for contacts, and then deposit the thermo-sensing film. This gives a much better contact between the metal and the thermo-sensing film, improving the device electrical characteristics.
5.	There are two ways to fabricate the metal – semiconductor contacts in planar structures. The first is when the metal lines climb the micro-bridge and make contact with the thermo-sensing film on the top of the bridge. In this approximation the lines are commonly broken, and the yield is low. The second approximation is when the thermo-sensing film comes down from the bridge and makes contact with the metal lines. It increases the yield, but reduces the device conductivity, since the metal-semiconductor contacts are more separated and are not on the bridge.	In the new design the two approximations are performed: the metal lines climb the bridge and also the thermo-sensing film goes down from the bridge and make contact with the metal lines, allowing have the metal contacts on the top of the bridge, without a reduction in yield. This can be possible with an optimal side wall angle of the Al sacrificial layer.

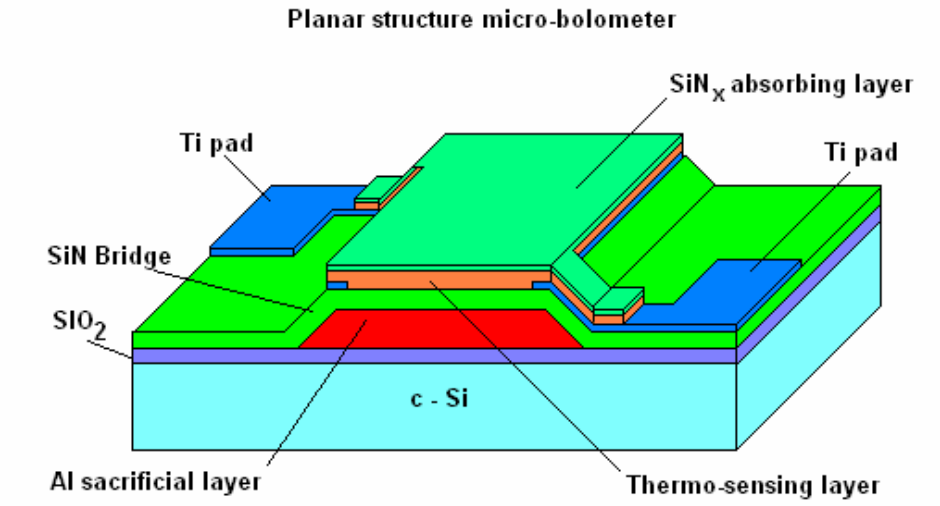

Figure 4.6. 3-D view of a modified planar structure micro-bolometer.

Figure 4.6 shows a 3-D view of the proposed micro-bolometer configuration, which will be implemented as cell in the micro-bolometer arrays, while Figure 4.7 shows a comparison between the standard and the modified process flows, in order to observe the main differences between both processes.

4.3.2 Design of sandwich structure micro-bolometer and process flow.

In the previous section we described the modified planar structure micro-bolometer with an intrinsic a-Si_xGe_y:H thermo-sensing film. A drawback of the planar structure is its very large cell resistance, since the metal electrodes are separated a distance of tens of micrometers. In order to reduce the high cell resistance doping has been employed [2.10], however by doing that, the activation energy, E_a, and TCR of the thermo-sensing film are reduced, resulted in a decrease of the micro-bolometer responsivity. In order to solve that problem, we have designed another micro-bolometer configuration, in which the metal electrodes sandwich the thermo-sensing film. Since the sensing film has a thickness $t \approx 0.5$ μm, the metal electrodes are very close and the electric filed through the thermo-sensing film is large, even with low voltage bias applied.

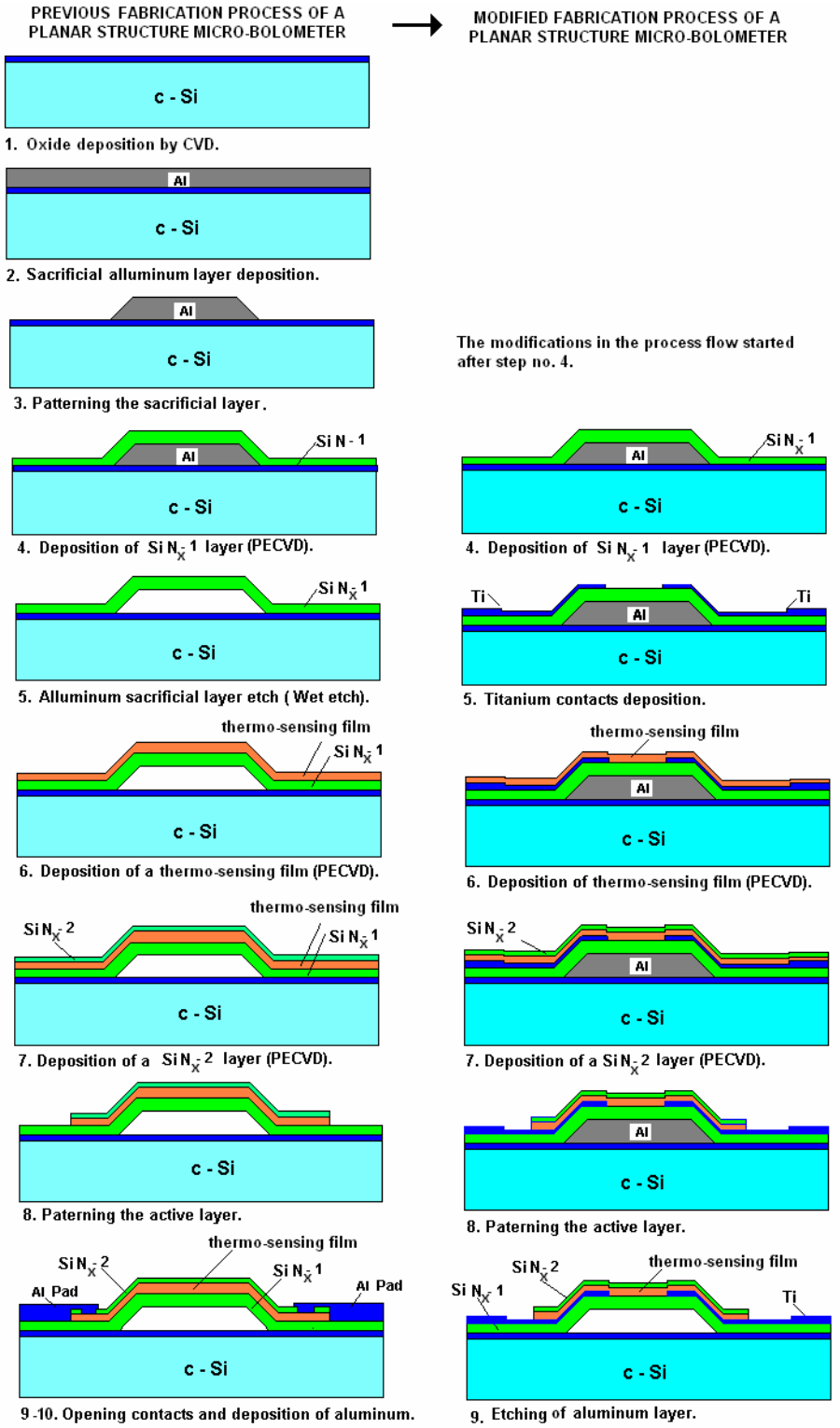

Figure 4.7. Modification in the process flow of a planar structure micro-bolometer.

This results in a lower resistance of the cell, without the disadvantages of doping. Figure 4.8 shows a 3-D view of a sandwich structure micro-bolometer. Figure 4.9 shows the process flow designed for the fabrication of the sandwich structure micro-bolometer. This structure is more complex than the planar one, since there are necessary 12 steps in order to fabricate it.

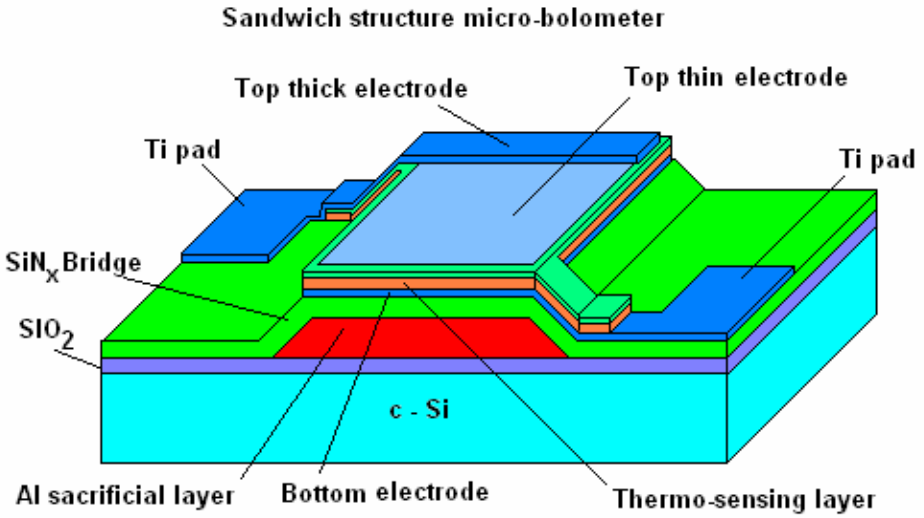

Figure 4.8. 3-D view of one micro-bolometer sandwich structure.

4.3.3 Design of "layout" of planar and sandwich structure micro-bolometers.

The planar cell B3 studied in section 4.2 has an active area A_{cell}= 100 x 100 μm^2, however the tendency in the development of micro-bolometer arrays is the reduction of the cell dimensions, as was described in section 2.7.

Figure 4.10 shows the layout for the fabrication of one modified planar structure micro-bolometer. For the fabrication of this micro-bolometer 4 masks (one mask less than in the previous planar configuration described in section 3.2.1) are necessary. Mask no. 1 is employed for the sacrificial layer, mask no. 2 for the micro-bridge, mask no. 3 for the metal contacts and mask no. 4 for both: the thermo-sensing film and a for the absorbing film.

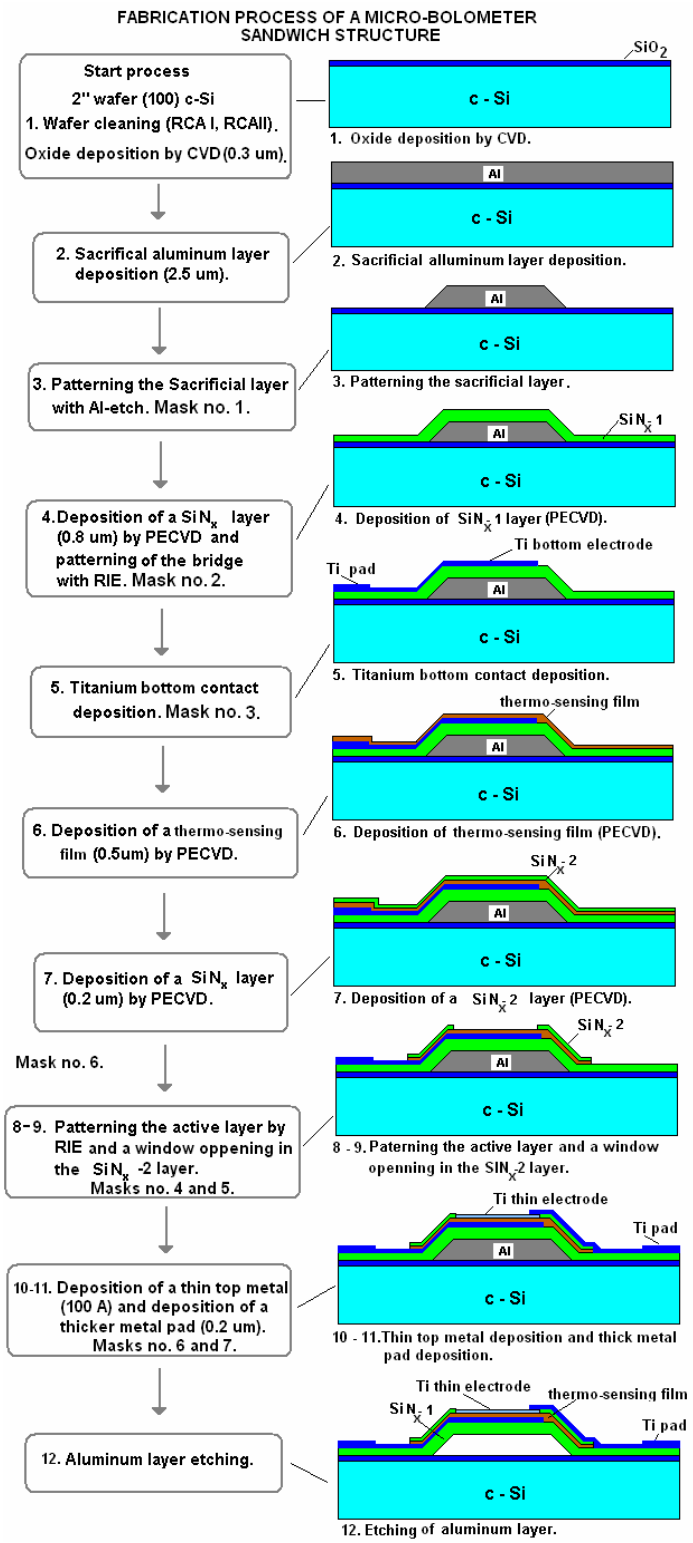

Figure 4.9. Process flow of a sandwich structure micro-bolometer.

The active area of planar structure is A_{cell}= 70 x 66 μm^2 and the metal pads area is A_{pad} = 120 x 120 μm^2, while the interconnection lines width is 20 μm. The active area was reduced in comparison with the structure B3 (A_{cell}= 100 x 100 μm^2), while the pads area was increased (from A_{pad} = 70 x 70 μm^2 in structure B3) in order to facilitate the manipulation of the devices (characterization and bonding).

Figure 4.11 shows the layout designed for the fabrication of sandwich structure micro-bolometers. For the fabrication of those micro-bolometers 7 masks are used. Mask no. 1 for the sacrificial layer, mask no. 2 for both: the micro-bridge and absorbing film, mask no. 3 for the bottom metal contact and pad, mask no. 4 for the thermo-sensing film, mask no. 5 for opening a window in the absorbing film for the top electrode. Mask no. 6 for the top tin electrode and mask no. 7 for the top metal pad. The active area of this structure is A_{cell}= 70 x 66 μm^2, the metal pads area is A_{pad} = 115 x 120 μm^2 and the interconnection lines width is 20 μm.

4.4 Design of un-cooled micro-bolometer arrays

We performed the design of one dimensional micro-bolometer arrays (1-D), taking into account the minimum dimension (10 μm) allowed by the INAOE micro-electronics lab technology, and the maximum dimensions allowed for the layout fabrication (4 mm).

4.4.1 Design of one dimensional (1-D) micro-bolometer arrays.

We designed 1-D arrays, which contain 32 cells. Every cell has an active area A_{cell}= 70 x 66 μm^2, the metal pads area is A_{pad} = 120 x 120 μm^2 and the interconnection lines width is 20 μm, as was discussed for the design of single cells micro-bolometers. In order to save area, there are 3 common nodes for the micro-bolometers in the array. The total 1-D array area including interconnection lines and pads is A_A=1.6 x 3.1 mm^2. The 1-D array layout is shown in Figure 4.12, the layout has been designed in order to fabricate independently arrays with both types of micro-

bolometers: planar structure and sandwich structure, which were discussed in section 4.3.3. The software employed for the layout design was “Tanner L-edit pro v8.11”.

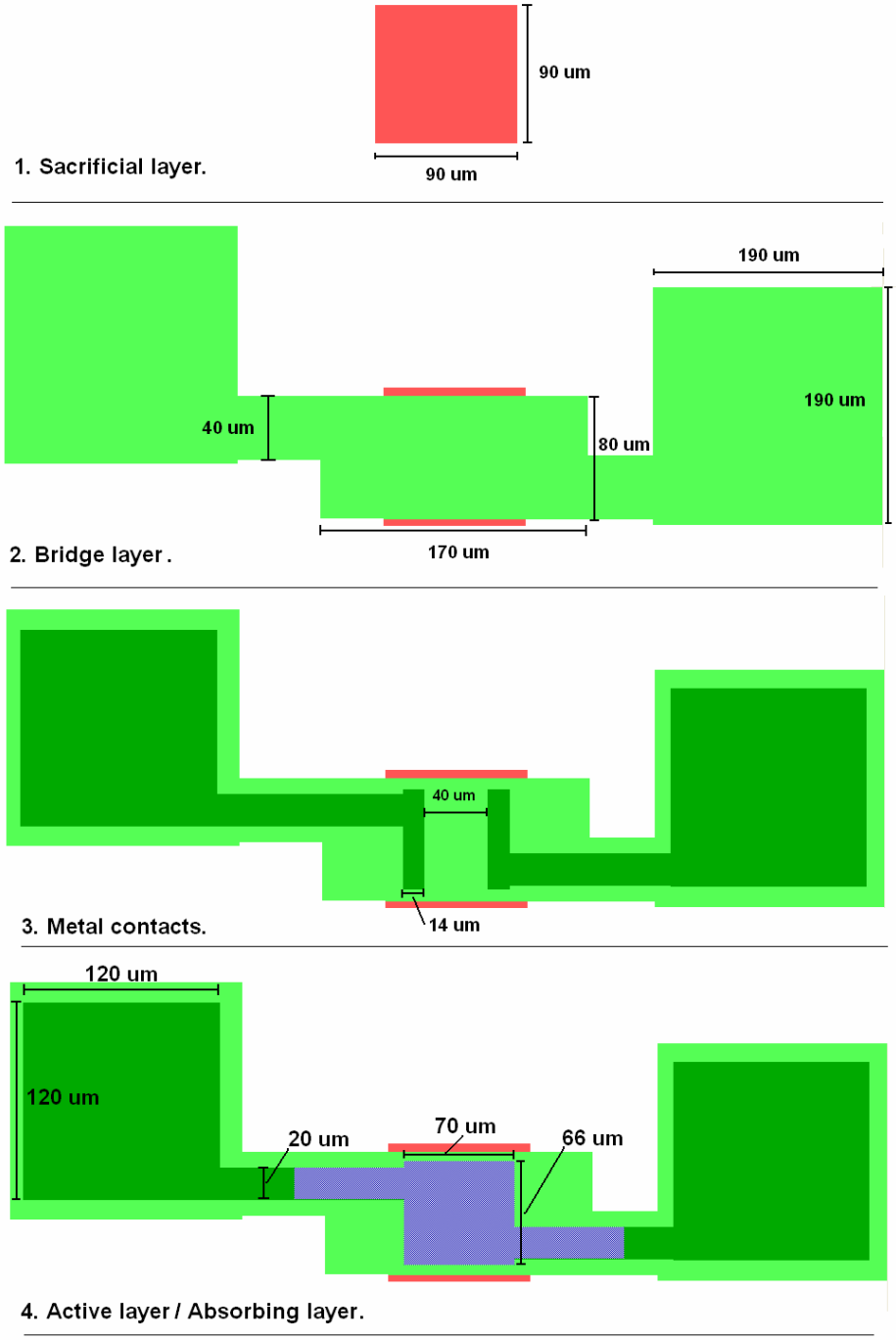

Figure 4.10. Layout of a modified planar structure micro-bolometer.

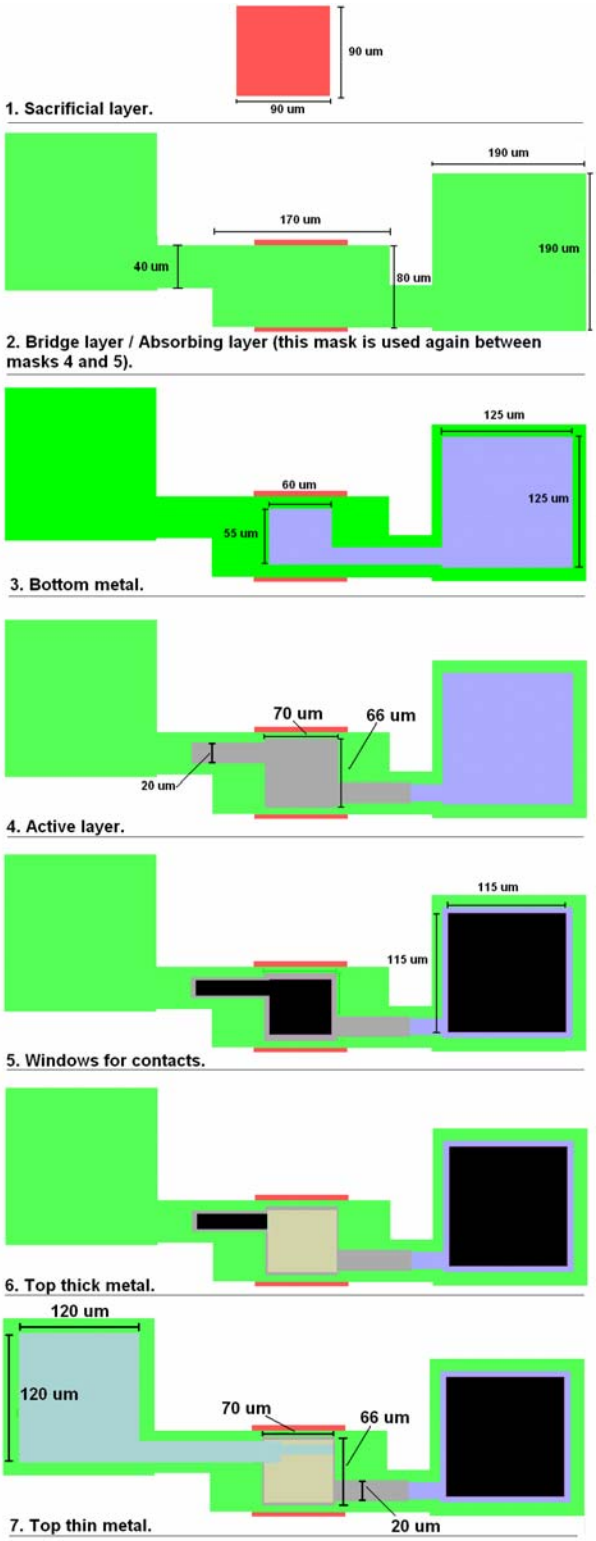

Figure 4.11. Layout of a sandwich structure micro-bolometer.

4.4.2 Design of two dimensional (2-D) micro-bolometer arrays.

We designed a two-dimensional (2-D) micro-bolometer array, It consisted of 72 cells, divided in 9 columns and 8 rows. The cell active area is A_{cell}= 60 x 68 μm^2, while the metal pads area is A_{pad} = 100 x 100 μm^2, and the interconnection lines width is 25 μm. The total 2-D array area including interconnection lines and pads is A_A=1.2 x 1.5 mm^2. Figure 4.12 shows the layout for the 2-D array. The layout has been designed in order to contain planar structure micro-bolometers and is composed of two level interconnection lines, which are fabricated under the micro-bolometers.

4.4.3 Design of layout and mask fabrication of the 1-D and 2-D arrays.

For simplification reasons (save masks), the 1-D array and the 2-D array were designed in the same layout, which have an area A_{layout} = 3.8 x 3.8 mm^2. In the layout also are included probe structures, which are four points and Kelvin structures in order to test the conductivity of the thermo-sensing film properties during the fabrication process. Figure 4.12 shows the layout design, which is composed of a set of 12 masks; with a combination of that masks we can fabricate independently 1-D arrays with planar and sandwich structures and 2-D arrays with planar structures.

4.5 Deposition of a-Si_xGe_y:H and a-$Si_xGe_yB_z$:H thermo-sensing films

In section 3.2.5 were described the parameters for the deposition of the a-Si_xGe_y:H film used as thermo-sensing film in micro-bolometers. These films showed high activation energy E_a=0.34 eV and a high TCR value α = 0.043 K^{-1}, and improved but still high cell resistance [2.18, 3.1]. In order to reduce the undesirable high resistance of the a-Si_xGe_y:H intrinsic films, we proposed to use amorphous silicon-germanium-boron (a-$Si_xGe_yB_z$:H) alloys as thermo-sensing films in un-cooled micro-bolometers. These films have been studied for applications on cooled micro-bolometers at temperatures T ≈ 77 K. [3.5, 4.1].

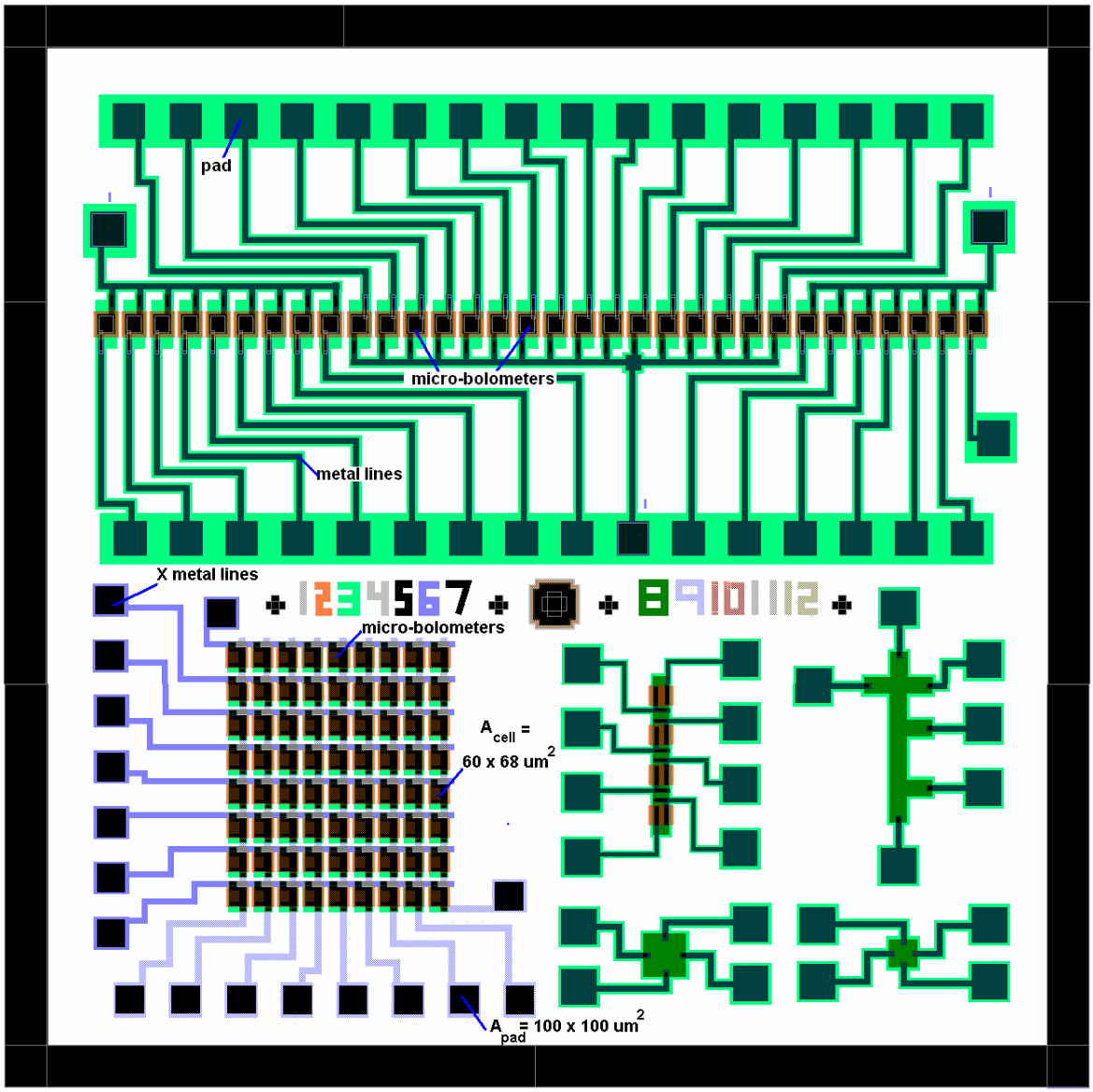

Figure 4.12. Layout of the micro-bolometer arrays.

The a- $Si_xGe_yB_z$:H films were deposited by low frequency (LF) PECVD in a capacitive discharge at frequency f = 110 KHz, substrate temperature T_s = 300 ^oC, pressure P = 0.6 Torr and RF power W = 350 W. Three sets of films were deposited from SiH_4 (100%), GeH_4 (100%) and B_2H_6 (1% on H_2) gas mixture, with a fixed SiH_4 and B_2H_6 gas flow rates: Q_{SiH4}=50sccm and Q_{B2H6}=500 sccm, respectively, while the GeH_4 gas flow was set at the following values: Q_{GeH4} =25, 50 and 75 sccm.

The late resulted in a Ge gas content Y = 0.3, 0.45, 0.55 and a B gas content Z = 0.11, 0.09, 0.07 in the samples labeled as process number 478, 479 and 480, respectively. An intrinsic film (a-Si_xGe_y:H) was deposited in order to compare its characteristics with that of the boron alloys, labeled as process number 443. This film was deposited under the same conditions as used for the boron alloys, with different gas mixture: SiH_4, GeH_4 and H_2; with gas flow rates: Q_{SiH4}=25 sccm, Q_{GeH4} =25 sccm and Q_{H2}=1000 sccm respectively. This result in a Ge gas content Y = 0.5. Table 4.4 shows the deposition parameters for 4 thermo-sensing films deposition processes.

Table 4.4. Parameters for the thermo-sensing films deposition.

	Process 478	**Process 479**	**Process 480**	**Process 443 (intrinsic)**
Gases flow rates (sccm)	SiH_4 (100%): 50 GeH_4(100%): 25 B_2H_6 (1%): 500	SiH_4 (100%): 50 GeH_4(100%): 50 B_2H_6 (1%): 500	SiH_4 (100%): 50 GeH_4(100%): 75 B_2H_6 (1%): 500	SiH_4(100%): 25 GeH_4(100%):25 H_2: 1000
Dilution ratio (%): $\frac{H_2}{SiH_4+GeH_4+B_2H_6}$	6.2	4.7	3.8	20
Ge_x content in gas mixture (%)	30	45	55	50
B_x content in gas mixture (%)	11	9	7	----
Temperature (^oC)	270/270/270	270/270/270	270/270/270	300/300/350
Pressure (Torr.)	0.6	0.6	0.6	0.6
Frequency (Khz.)	110	110	110	110
Power (W)	300	300	300	300

Since those films are studied for applications as thermo-sensing films for micro-bolometers, we measured the film electrical properties after patterning them with photolithography in one cell of dimensions 70 x 66 μm^2. Assuming that stress arisen in the film deposited over a SiN_x micro-bridge could have an effect on the film conductivity, we also studied the films deposited on a micro-bridge. For that purpose,

we prepared three different kinds of samples for each type of the four thermo-sensing films (three boron alloys with different Ge_y content and the intrinsic reference film). The films were prepared as is depicted in Figure 4.13. In the stripes and micro-bridges samples, thermo-sensing film was deposited over the metal electrodes, while in the patterned sample the metal electrodes were deposited over the thermo-sensing film.

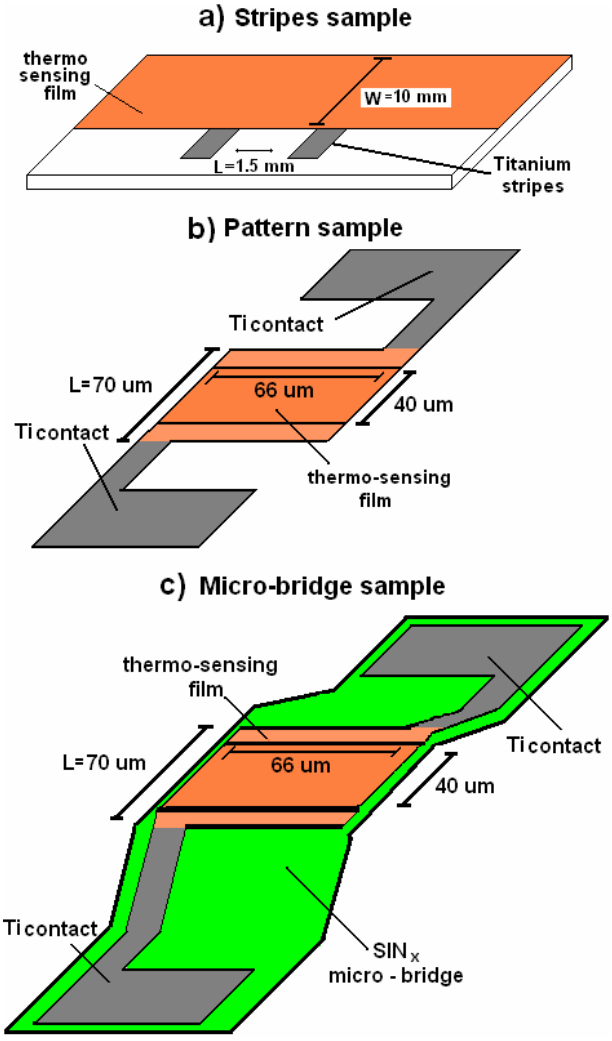

Figure 4.13. Thermo-sensing film samples: a) stripes, b) patterned and c) micro-bridges.

Table 4.5. Samples used for characterization.

	Thermo-sensing films			
	Process 478	**Process 479**	**Process 480**	**Process 443**
Samples	#1: Stripes	#2: Stripes	#3: Stripes	#4: Stripes
	#5: Patterned	#6: Patterned	#7: Patterned	#8: Patterned
	Not available	#9: Micro-bridge	#10:Micro-bridge	#11: Micro-bridge

After fabrication, the different samples available are listed in Table 4.5. In section 4.7 the characterization of these thermo-sensing films is described.

4.6 Characterization of thermo-sensing films

4.6.1 Temperature dependence of conductivity and TCR in a-Si_xGe_y:H and a-$Si_xGe_yB_z$:H films.

We performed measurements of temperature dependence of conductivity σ(T) in the a-Si_xGe_y:H and a-$Si_xGe_yB_z$:H thermo-sensing films (different samples are described in section 4.5), in the range of T= 300 – 400 K. The measurements were performed in a vacuum chamber at a pressure P ≈ 20 mTorrs. A temperature controller (model K-20, MMR Inst.) for the temperature measurement control and an electrometer (model 6517-A, Keithley Inst.) for the current measurements were employed. These measurements allowed us to obtain the σ(T) temperature dependence and then to determine the E_a, the TCR and the room temperature conductivity, σ_{RT}.

The conductivity temperature dependence can be well described by $\sigma(T)=\sigma_0 \exp(-E_a/kT)$, where σ_0 is the prefactor, E_a is the activation energy, k is the Boltzmann constant and T is the temperature. Figure 4.14 shows σ(T) curves for four different thermo-sensing films (three boron alloys with different Ge_y gas content, Ge_y = 0.3, 0.45, 0.55 and the intrinsic film with Ge_y = 0.5), fabricated in three different sample configurations (stripes, patterns and micro-bridges).

From σ(T) measurements with temperature in the thermo-sensing films, we found that the boron alloys (a-$Si_xGe_yB_z$:H) have a significantly larger conductivity (by about 2-3 orders of magnitude) in comparison with that of the intrinsic reference film (a-Si_xGe_y:H). We observed that an increment in the Ge_y content in gas phase in the boron alloys results in an increase of the room temperature conductivity, from σ_{RT} = 2.8 x10^{-3} $(\Omega cm)^{-1}$ (for Ge_y = 0.3) to σ_{RT} = 1 x10^{-2} $(\Omega cm)^{-1}$ (for Ge_y = 0.45) and σ_{RT} = 2.5 x10^{-2} $(\Omega cm)^{-1}$ (for Ge_y = 0.55), while for the intrinsic film the room temperature conductivity is σ_{RT} = 6 x10^{-5} $(\Omega cm)^{-1}$ (for Ge_y = 0.5).

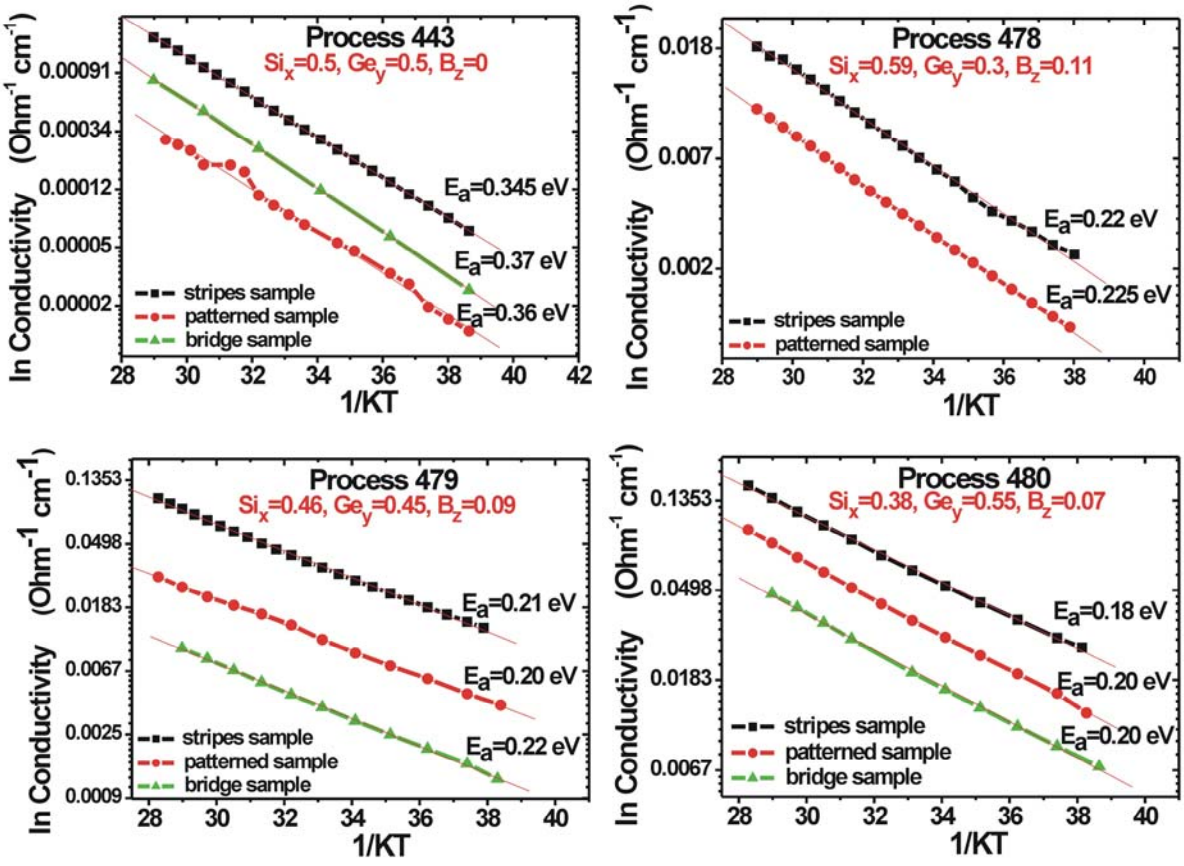

Figure 4.14. Conductivity dependence with temperature for the different thermo-sensing films (process: 443, 478, 479 and 480).

The increment in the σ is accompanied with a reduction in the E_a. We obtained an E_a= 0.22 eV (for Ge_y = 0.3), E_a= 0.21 eV (for Ge_y = 0.45) and E_a= 0.18 eV (for Ge_y = 0.55), while in the intrinsic film is E_a= 0.345 eV (for Ge_y = 0.5). The E_a as a function of Ge_y is shown in Figure 4.15.

The reduction in the thermo-sensing films dimensions, from the stripes samples (10 x1.5 mm^2) to the patterned samples (70 x 66 μm^2), has no significant effect on the E_a, however it has on the σ. We observed a reduction by 50 – 80 % of the σ value in the patterned samples in comparison with that of the stripes samples. Practically no change in the E_a of the thermo-sensing films deposited over a SiN_x micro-bridge was observed, in comparison with that of the stripes and patterned samples, however the micro-bolometer samples showed a larger reduction in the σ values, around 60 – 90 %. The Ge_y content and the sample structure dependence of σ are shown in Figure 4.16, while the deposition rate dependence of Ge_y content in the thermo-sensing films is shown in Figure 4.17. Table 4.6 show a comparison of E_a, TCR, σ_{RT} and σ_0 in stripes, patterned and micro-bridges samples for the different thermo-sensing films.

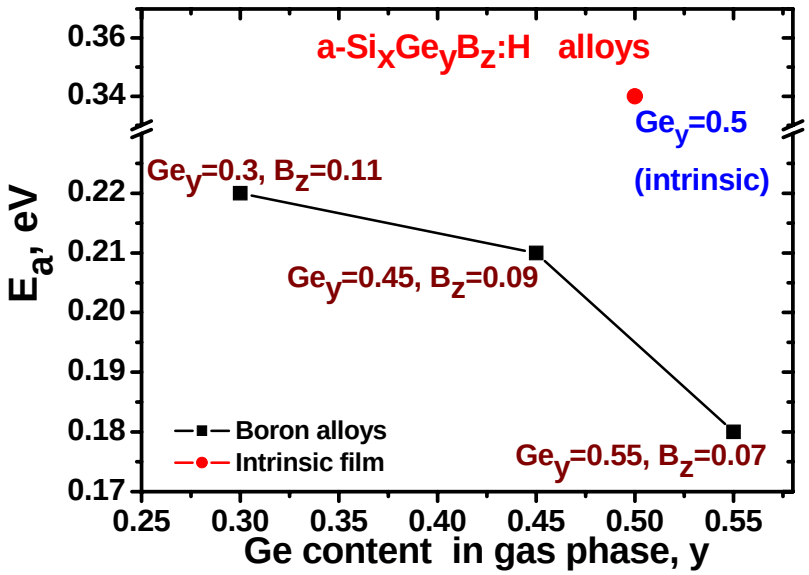

Figure 4.15 E_a as function of Ge gas content, Ge_y, in the boron alloys, a-$Si_xGe_yB_z$:H.

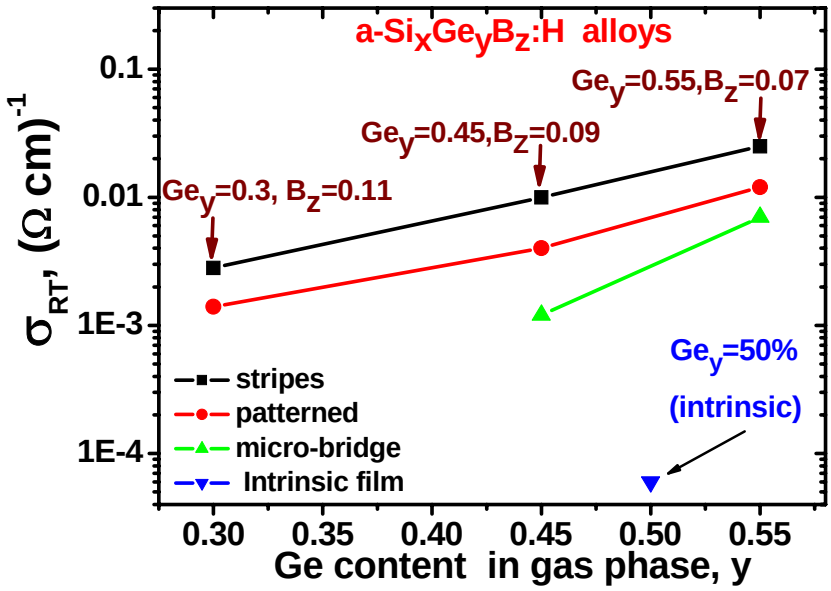

Figure 4.16 Conductivity dependence on the Ge gas content, Ge_y.

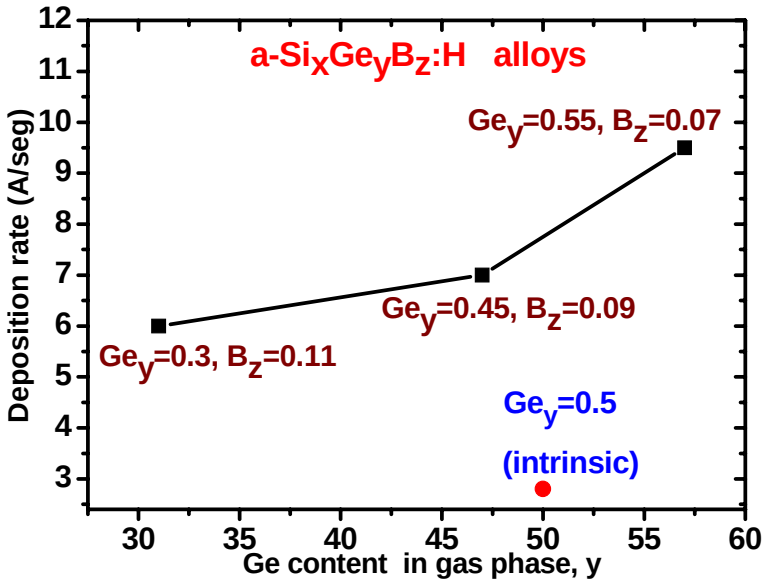

Figure 4.17. Deposition rate dependence on the Ge gas content, Ge_y.

In the patterned samples the metal electrodes are deposited over the thermo-sensing film, in comparison with the stripes samples, where the metal electrodes are under the film. In the patterned samples the surface current can be the main contribution of current rather than the bulk current, resulting in a reduction of conductivity.

In the micro-bridges samples the metal electrodes are under the film, as in the stripes samples, however they have the largest reduction of conductivity, it could be explained by the stress arisen in the SiN_x micro-bridge, affecting the thermo-sensing film electrical conductivity.

The deposition rate in the boron alloys is around 2 -3 times larger than that of the intrinsic film. Boron incorporation during the thermo-sensing deposition, enhance the deposition rate as is shown in Figure 4.17.

4.6.2 Composition of the a-Si_xGe_y:H and a-$Si_xGe_yB_z$:H films.

The composition in solid phase of the different films (three boron alloys with different Ge gas content and the intrinsic film, described in section 4.5) was characterized by secondary ion mass spectroscopy (SIMS). The samples used for SIMS characterization were the stripes samples described in section 4.5 and showed in figure 4.13 a). Figure 4.18 shows the SIMS profiles obtained.

From SIMS profiles we calculated the solid composition in the thermo-sensing films. For the film with gas content: Ge_y=0.3 and B_z=0.11 (process 478), we observed an increase in the solid content: Ge_y=0.59 and B_z=0.32 respectively. For the film with Ge_y=0.45 and B_z=0.09 (process 479), we observed Ge_y=0.67 and B_z=0.26, respectively and for the film with Ge_y=0.55 and B_z=0.07 (process 480), we observed Ge_y=0.71 and B_z=0.23, respectively. These results suggested a strong preferential B and Ge incorporation from gas phase during the film deposition process. The B_z solid content demonstrated values about 3 times larger than the content in gas phase B_z, while the Ge_y solid content increased by a factor of 1.3 – 2 from the Ge_y gas content. Those results are shown in Table 4.7.

Table 4.6. Comparison of E_a, TCR, σ_{RT} and σ_0 in stripes, patterned and micro-bridges samples for the different thermo-sensing films.

		Thermo-sensing films			
		Process 478	**Process 479**	**Process 480**	**Process 443**
Film Thickness (µm)		0.36	0.42	0.51	0.5
Deposition rate ($\overset{o}{A}$/s)		6	7	9.5	2.8
Stripes samples	**E_a (eV)**	**0.22**	**0.21**	**0.18**	**0.345**
	TCR (K^{-1})	-0.028	-0.027	-0.023	-0.044
	σ_{RT} $(\Omega cm)^{-1}$	**$2.8x10^{-3}$**	**$1x10^{-2}$**	**$2.5x10^{-2}$**	**$6x10^{-5}$**
	σ_0 $(\Omega cm)^{-1}$	12.02	36.46	24.55	34.85
Patterned samples	**E_a (eV)**	**0.225**	**0.20**	**0.20**	**0.36**
	TCR (K^{-1})	-0.029	-0.025	-0.025	-0.046
	σ_{RT} $(\Omega cm)^{-1}$	**$1.4x10^{-3}$**	**$4x10^{-3}$**	**$1.2x10^{-2}$**	**$1.08x10^{-5}$**
	σ_0 $(\Omega cm)^{-1}$	7.27	8.23	28.26	11.13
Micro-bridge samples	**E_a (eV)**	**Not available**	**0.22**	**0.20**	**0.37**
	TCR (K^{-1})		-0.028	-0.025	-0.047
	σ_{RT} $(\Omega cm)^{-1}$		**$1.2x10^{-3}$**	**$7x10^{-3}$**	**$2.2x10^{-5}$**
	σ_0 $(\Omega cm)^{-1}$		5.94	15.58	32.8

Table 4.7. Comparison between gas content for the thermo-sensing films deposition and the solid content obtained by SIMS.

		Thermo-sensing films			
		Process 478	**Process 479**	**Process 480**	**Process 443**
Gas content	**Si_x**	0.59	0.46	0.38	0.5
	Ge_y	0.3	0.45	0.55	0.5
	B_z	0.11	0.09	0.07	0
Solid content obtained from SIMS	**Si_x**	0.078	0.05	0.04	0.11
	Ge_y	0.59	0.67	0.71	0.88
	B_z	0.32	0.26	0.23	$2.0x10^{-5}$

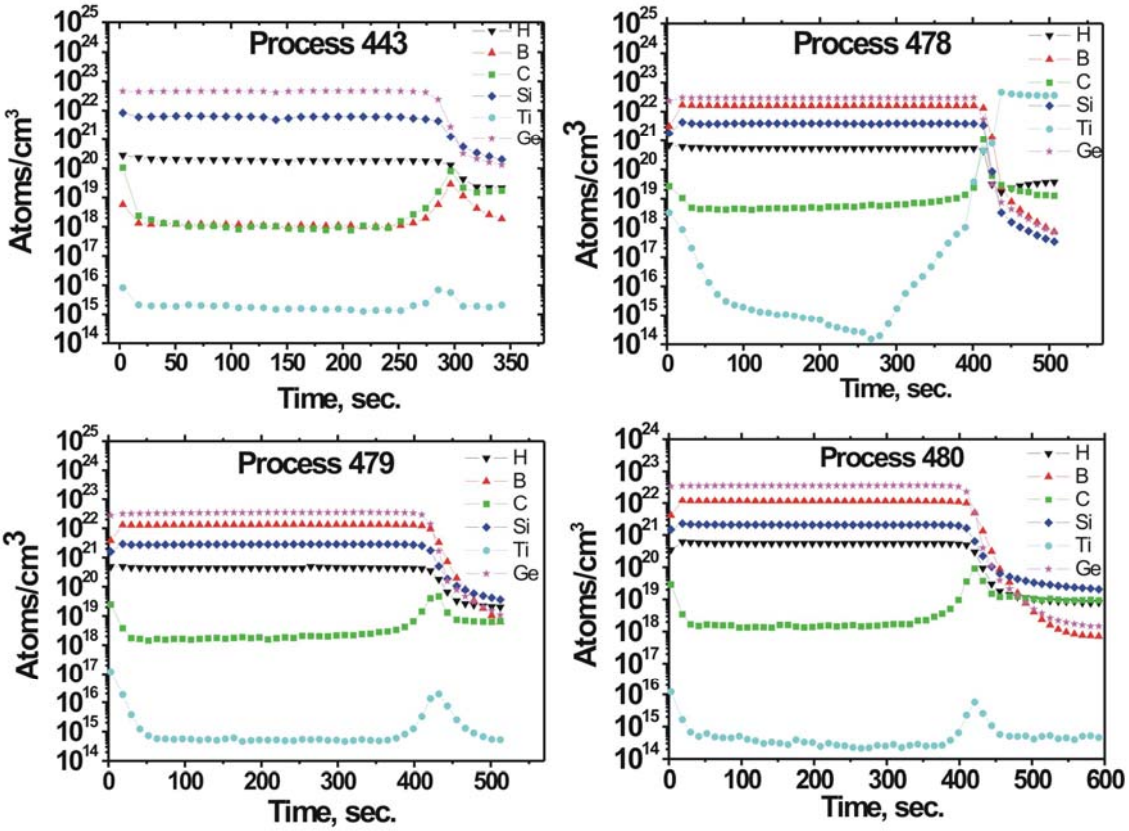

Figure 4.18. SIMS profiles of a-Si_xGe_y:H and a-$Si_xGe_yB_z$:H thermo-sensing films.

SIMS characterization was performed by Dr. Y Kudriavtsev from CINVESTAV, Mexico DF.

4.6.3 FTIR spectroscopy characterization in a-Si_xGe_y:H and a-$Si_xGe_yB_z$:H.

The IR absorption spectra of the a-$Si_xGe_yB_z$:H films (processes 478, 479, 480) and the intrinsic a-Si_xGe_y:H film (process 443 described in section 4.5.1) are shown in Figure 4.19. In the intrinsic film it is observed a Ge-H waging and rocking modes at k=560 cm^{-1} [4.2]. Near to 960 cm^{-1} it is observed a peak which is related to a Ge-O bonds [4.3-4.5]. The peak at k=1100 cm^{-1} is related to a Si-O bonds [4.6]. The absorption peak near 1880 cm^{-1} is attributed to the stretching vibration of Ge-H groups [4.7] and at k=2000 cm^{-1} is observed a peak a Si-H stretching mode [4.6].

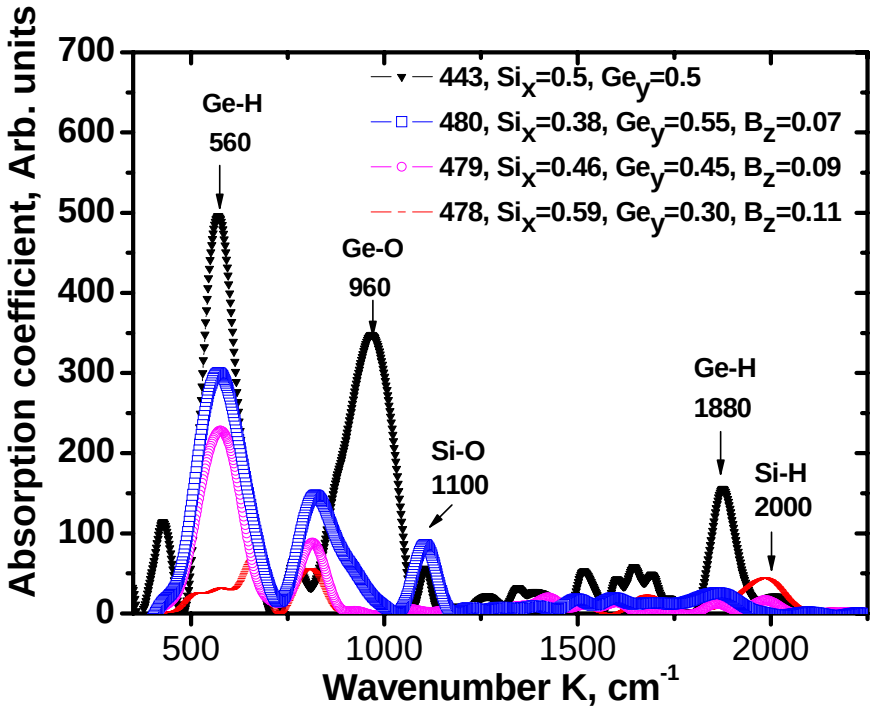

Figure 4.19. Infrared spectra of the a-$Si_xGe_yB_z$:H and a-Si_xGe_y:H thermo-sensing films.

In the boron alloys appears the peak at k=560 cm^{-1} observed in the intrinsic film, which is related with the Ge-H waging and rocking modes, however it decreases as the Ge gas content (y) decreases. Also is observed the peak at k=1100 cm^{-1} which is related to Si-O bonds. At k=810 cm^{-1} is observed a peak related to a Ge-H_2 bending mode [4.8], this peak increase as y increase.

4.7 Fabrication process of un-cooled micro-bolometer arrays

In sections 4.3 and 4.4 the process flow for the fabrication of planar and sandwich structure micro-bolometers and the design of 1-D and 2-D micro-bolometer

arrays were described, respectively. In this section the fabrication of 1-D micro-bolometer arrays with a-Si_xGe_y:H and a-$Si_xGe_yB_z$:H thermo-sensing film is described.

4.7.1 Fabrication of one dimensional (1-D) micro-bolometer arrays.

4.7.1.1 Planar structure micro-bolometer 1-D arrays with a-Si_xGe_y:H and a-$Si_xGe_yB_z$:H thermo-sensing film.

The fabrication process of 1-D arrays containing modified planar structure micro-bolometers (described in section 4.3), is the following:

11. Initially a c-Si substrate is covered by 0.2 μm-thick SiO_2 film deposited by CVD at substrate temperature T_s= 350 ^oC.
12. A 2.5 μm – thick aluminum (Al) layer is deposited by e-beam evaporation over the SiO_2 layer.
13. A lithographic step using the sacrificial mask (mask no. 1 of layout described in figure 4.10) and a wet etching step are carried out in order to pattern the Al sacrificial layer. The etching solution is a modified Al-etch solution, which is composed by phosphoric acid**:** acetic acid**:** nitric acid, at a concentration of 75: 22: 6 (The normal Al-etch concentration is 75: 22: 3). With this solution is possible obtain a side wall angle of 15 ^{0} [1.12], as I shown in Figure 4.20.

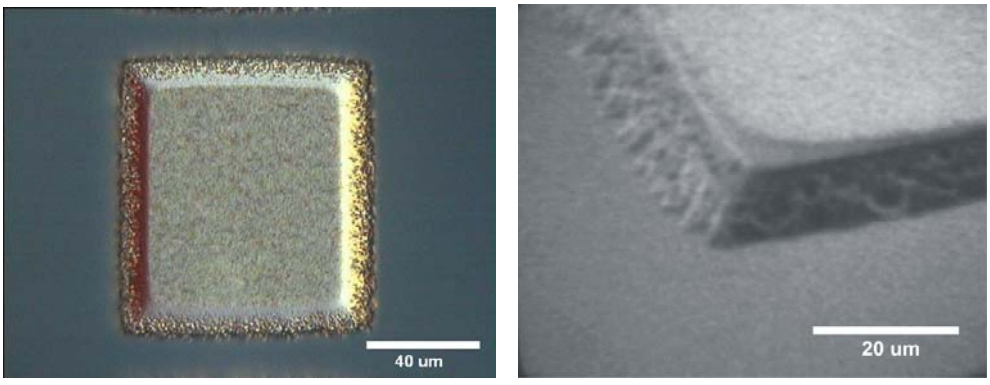

a) Top view of an Al pattern. b) SEM view of an Al pattern.

Figure 4.20. Al sacrificial patterns with a 15 ^{0} side wide angle.

14. A 0.8 μm - thick SiN_x film is deposited by low frequency (LF) PECVD at T_s= 350°C. A lithographic step using the micro-bridges mask (mask no. 2 described in figure 4.10) and a dry etching step (with Reactive Ion etching - RIE) is performed in order to pattern the micro-bridges.

    The lithographic and etching steps are divided in two parts in order to avoid over etch the SIN_x micro-bridges, as was discussed in section 4.3.1.

    Figure 4.21 shows a fragment of a 1-D array, where the SiN_x micro-bridges over the Al patterns are observed.

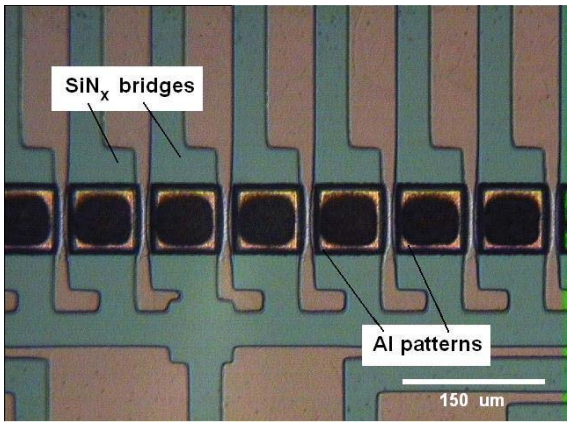

Figure 4.21. SiN_x micro-bridges over Al patterns.

15. A 0.2 μm-thick titanium (Ti) layer is deposited by e-beam evaporation over the SiN_x bridges and a lithographic step was performed (mask no. 3 of Figure 4.10) in order to form the contacts and interconnection lines. Figure 4.22 shows the Ti contacts deposited over the SiN_x micro-bridges.
16. A 0.5 μm – thick thermo-sensing film is deposited by PECVD. Details of deposition are described in section 4.5.
17. The thermo-sensing film is covered with a 0.2 μm-thick SiN_x absorbing film deposited by LF PECVD. Details of deposition are described in section 3.2.4. A lithographic step and dry etching (RIE) is performed in order to pattern the active area, this step is divided in two parts for avoid over etching in the active area, as was discussed in section 4.3.1. Figure 4.23 shows a fragment of

a 1-D array after the deposition and patterning of the thermo-sensing and absorbing films.

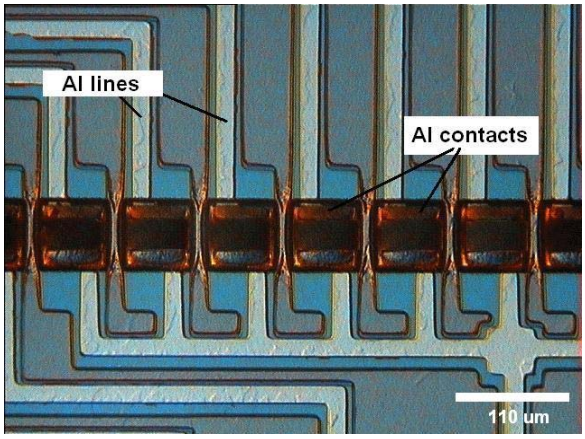

Figure 4.22. Ti contacts over the SiN_x micro-bridges.

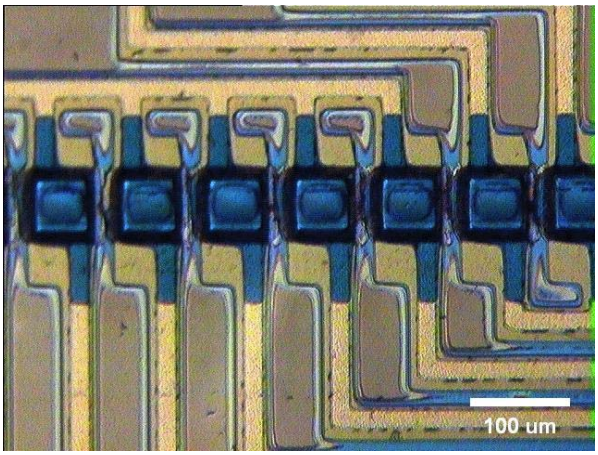

Figure 4.23. Fragment of 1-D array after the deposition and patterning of the thermo-sensing and absorbing films.

18. The final step is the etching of the Al sacrificial patterns with the modified Al-etch solution, at the end of the fabrication process flow. Figure 4.24 shows a fragment of 1-D array at the end of the fabrication process, when the Al sacrificial layer is removed. Figure 4.25 shows a top view of one planar structure micro-bolometer at the end of the fabrication process.

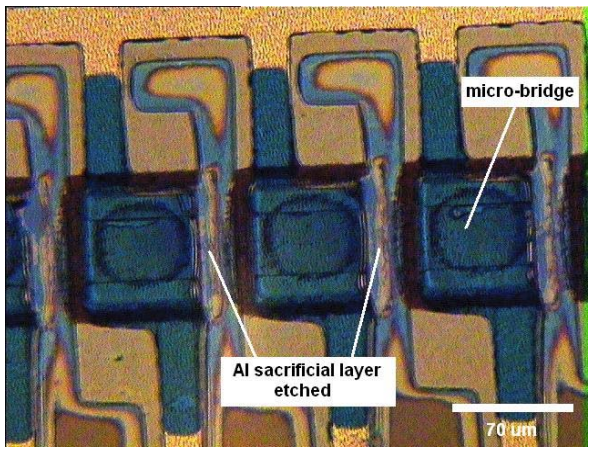

Figure 4.24. Fragment of 1-D array after the etching of the Al sacrificial layer.

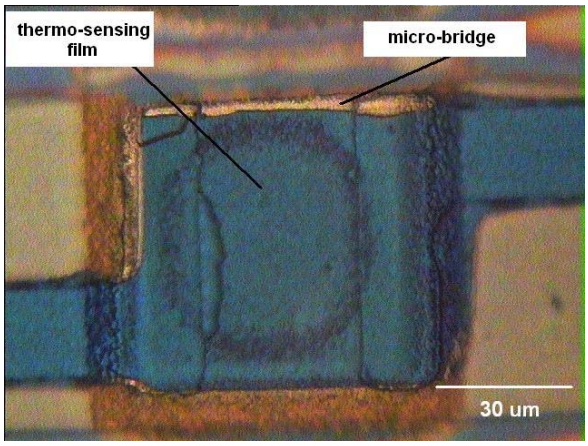

Figure 4.25. Top view of a planar structure micro-bolometer.

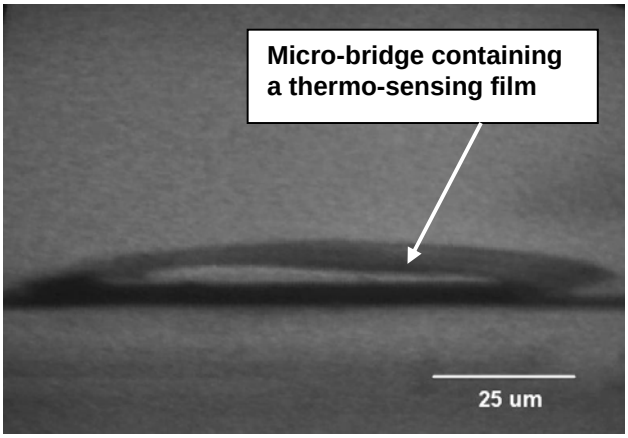

Figure 4.26. Transversal view of a micro-bolometer obtained by SEM.

Figure 4.26 shows a transversal view of a micro-bolometer obtained by SEM, while Figure 4.27 shows a fragment of a 1-D micro-bolometer array.

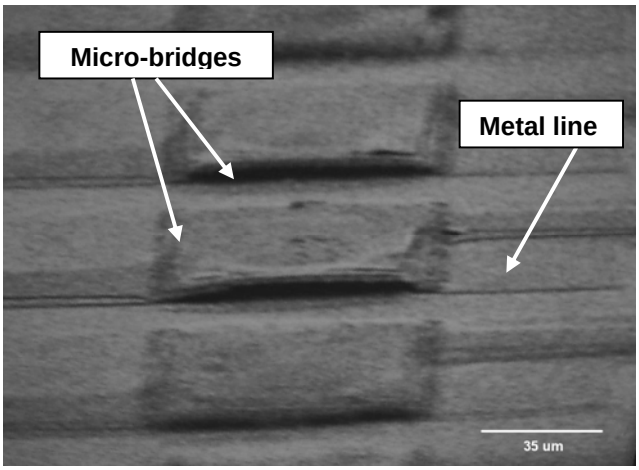

Figure 4.27. View of a fragment of 1-D micro-bolometer array obtained by SEM.

There were fabricated 3 processes of 1-D arrays of planar structure micro-bolometers with different thermo-sensing films: Process 443 (a-Si_xGe_y:H, Ge_y=0.5), process 479 (a-$Si_xGe_yB_z$:H, Ge_y = 0.45, B_z= 0.09) and process 480 (a-$Si_xGe_yB_z$:H, Ge_y = 0.55, B_z= 0.07). The thermo-sensing films fabrication processes were described in section 4.5.1.

4.7.1.2 Sandwich structure micro-bolometers 1-D arrays with Ge_xSi_y:H thermo-sensing film.

The first four steps for the sandwich structure fabrication are similar than those for the planar structure micro-bolometer. The fabrication process of the sandwich structure micro-bolometer 1-D array is the following:

1. A 0.3 μm – thick SiO_2 layer deposition by CVD.
2. A 2.5 μm - thick aluminum (Al) layer deposition by e-beam evaporation.
3. A lithographic and Al-etch steps in order to pattern the Al sacrificial layer.

4. A 0.8 μm - thick SiN_x film deposition by PECVD. A lithographic step and dry etching (RIE) in order to pattern the bridges (the lithographic step and etching is divided in two parts).
5. Deposition of a 0.2 μm – thick bottom Titanium (Ti) electrode and pad, with a lithographic step and e-beam evaporation.
6. A 0.5 μm – thick a-Si_xGe_y:H thermo-sensing film deposition by PECVD. Process 443 (a-Si_xGe_y:H, Ge_y=0.5), details of deposition are described in section 4.5.
7. A 0.2 μm – thick SiN_x layer deposition by PECVD.
8. A lithographic step and dry etching (RIE) in order to pattern the active area (this step is divided in two parts).
9. A lithographic step and dry etching (RIE) in order to open a window in the upper SiN_x layer.
10. Deposition of a 10 nm – thick Ti top electrode, with a lithographic step and e-beam evaporation.
11. Deposition of a 0.2 μm – thick Ti pad and interconnection line, with a lithographic step and e-beam evaporation.
12. Al sacrificial layer etching with Al-etch at the end of the fabrication process flow.

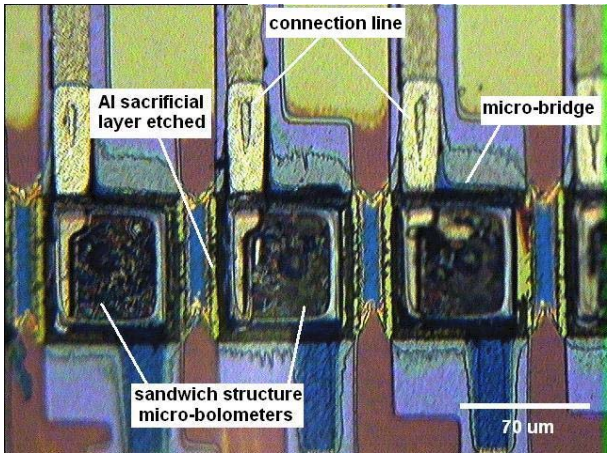

Figure 4.28. Top View of a fragment of one 1-D array of sandwich structure micro-bolometers.

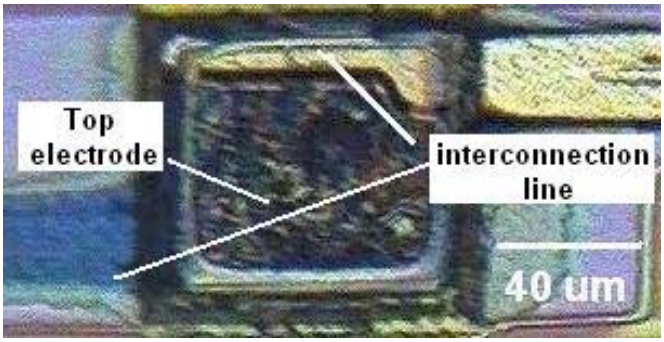

Figure 4.29. Top view of one sandwich structure micro-bolometer.

Figure 4.28 shows the top view of a fragment of a 1-D array of sandwich structure micro-bolometers, while Figure 4.29 shows a top view of one sandwich structure micro-bolometer. There was fabricated 1 processes of 1-D arrays of sandwich structure micro-bolometers with a-Si_xGe_y:H, (Ge_y=0.5) thermo-sensing film (Process 443).

4.7.2 Fabrication of two dimensional (2-D) micro-bolometer arrays of planar structure micro-bolometers with Ge_xSi_y:H thermo-sensing film.

The fabrication process of the planar structure micro-bolometer 2-D array is the following:

1. Deposition of a 0.2 μm – thick Ti layer and a lithographic step in order to form the first level of metal lines. Figure 4.30 shows the first level of Ti interconnection lines.
2. Deposition of a 0.25 μm – thick SiN_x film, in order to cover the first level of metal lines.
3. Deposition of a 0.2 μm – thick Ti layer and a lithographic step in order to form the second level of metal lines.
4. Deposition of a 0.25 μm – thick SiN_x film, in order to cover the second level of metal lines.
5. Deposition of a 2.5 μm - thick aluminum (Al) layer by e-beam evaporation.

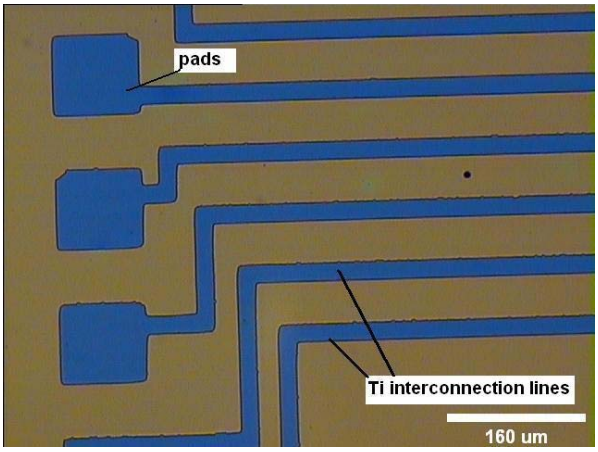

Figure 4.30. First level of Ti interconnection lines for the fabrication of 2-D arrays.

6. A lithographic step and wet etching step with a modified Al-etch solution in order to pattern the Al sacrificial layer with a side wall angle of 15^{o}. Figure 4.31 shows the Al sacrificial patterns for the fabrication of 2-D micro-bolometer arrays.

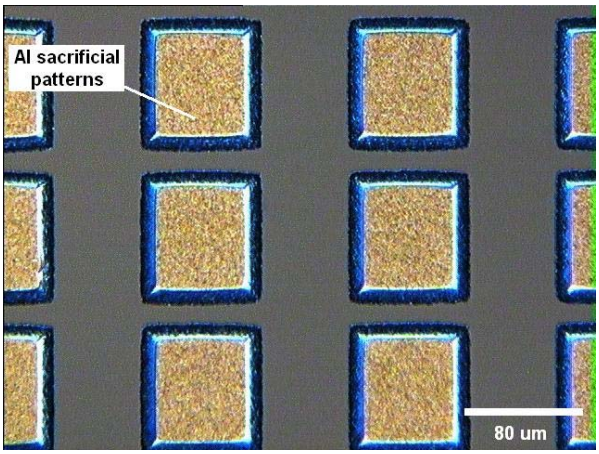

Figure 4.31. Al sacrificial patterns with a side wall angle of 15^{o}.

7. A 0.5 μm - thick SiN_x film deposition by PECVD. A lithographic step and dry etching (RIE) in order to pattern the micro-bridges (the lithographic step and etching is divided in two parts). Figure 4.32 shows the SiN_x micro-bridges, which are over the Al sacrificial patterns.

8. A lithographic step and SiN_x etching with RIE, in order to open windows and let parts of the Ti interconnection lines uncovered.
9. Deposition of a 1 μm – thick Ti layer and a lithographic step in order to form Ti contacts, which are connected with the interconnection lines and are placed over the micro-bridges, in order to contact the thermo-sensing film. Figure 4.33 shows the Ti contacts over the SiN_x micro-bridges.

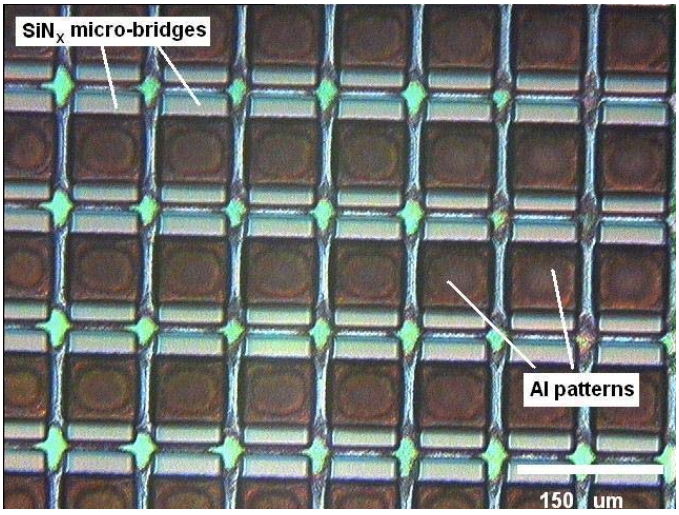

Figure 4.32. SiN_x micro-bridges over the Al sacrificial patterns.

10. Deposition of a 0.5 μm – thick a-Si_xGe_y:H thermo-sensing film by PECVD. Process 443 (a-Si_xGe_y:H, Ge_y=0.5), details of the thermo-sensing film deposition are described in section 4.5.
11. A 0.2 μm – thick SiN_x absorbing film deposition by PECVD. Details of deposition are described in section 3.2.4.
12. A lithographic step and dry etching (RIE) is performed in order to pattern the active area (this step is divided in two parts in order to avoid over etch the thermo-sensing film and absorbing film).
13. The Al sacrificial layer is etched with Al-etch at the end of the fabrication process flow.

Figure 4.33. Ti contacts deposited over SiN_x micro-bridges.

Figure 4.34 shows one planar structure micro-bolometer which belong to a 2-D array, while Figure 4.35 shows a 2-D array at the end of the fabrication process. The array is composed of two levels of Ti interconnection lines, which are under the micro-bolometer and separated by SiN_x films. In the array are 72 planar structure micro-bolometer cells.

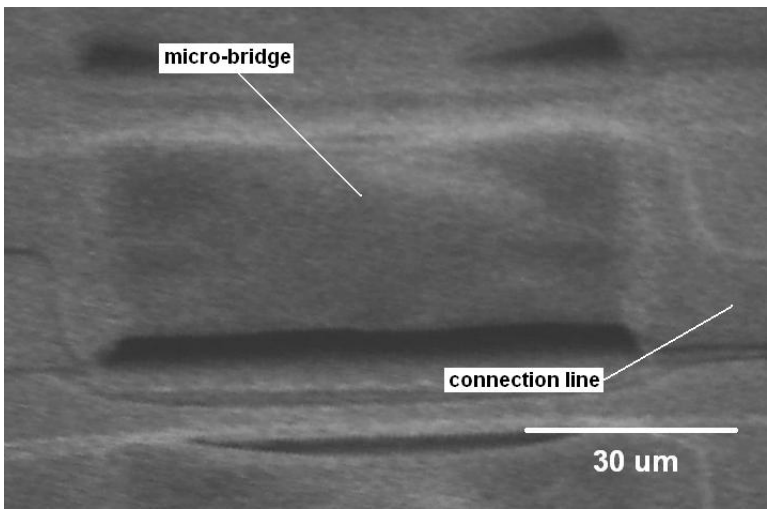

Figure 4.34. One micro-bolometer, which belong to a 2-D micro-bolometer array.

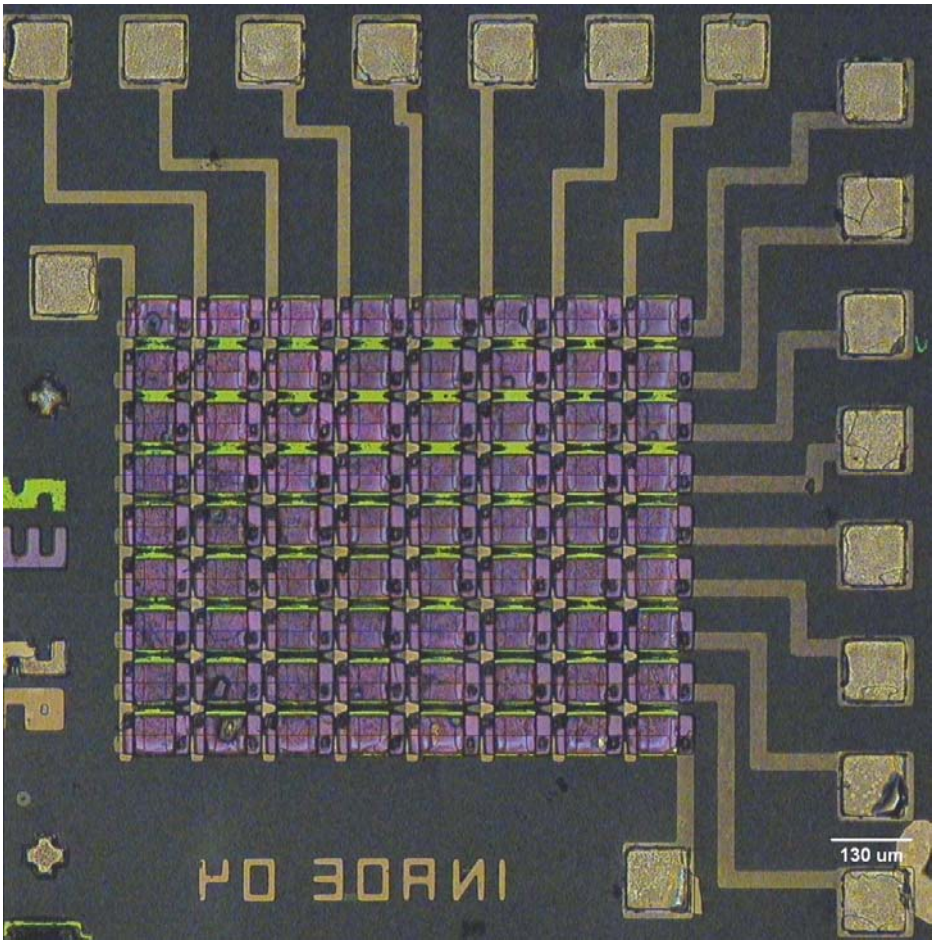

Figure 4.35. Top view of a 2-D planar structure micro-bolometer array.

There was fabricated one process of a 2-D array of planar structure micro-bolometers with a-Si_xGe_y:H, (Ge_y=0.5) thermo-sensing film (Process 443).

4.8 Comparative characterization of four different un-cooled micro-bolometer configurations.

In this section we present a comparative study of four configurations of un-cooled micro-bolometers based on amorphous silicon-germanium thin films deposited by plasma.

The current-voltage characteristics I(U), current noise spectral density (NSD) and response time have been measured in order to characterize and compare the performance characteristics, such as responsivity and detectivity in four configurations of micro-bolometers:

a) Planar structure with a silicon-germanium intrinsic (a-Si_xGe_y:H, Ge_y=0.5) thermo-sensing film (process no. 443).

b) Planar structure with a silicon-germanium-boron alloy (a-$Si_xGe_yB_z$:H, Ge_y=0.45, B_z=0.09) thermo-sensing film (process no. 479).

c) Planar structure with a silicon-germanium-boron alloy (a-$Si_xGe_yB_z$:H, Ge_y=0.55, B_z=0.07) thermo-sensing film (process no. 480).

d) Sandwich structure with an intrinsic (a-Si_xGe_y:H, Ge_y=0.5) thermo-sensing film (process 443).

These devices were described in section 4.3 and belong to the 1-D arrays and their fabrication process was described in section 4.7.

4.8.1 Measurements of current-voltage characteristics I(U) in dark and under Infrared radiation and responsivity calculations.

The measurement of I(U) characteristics were performed in dark and under IR illumination conditions. The source of IR light is a SiC globar source, which provides intensity $I_0=5.3x10^{-2}$ Wcm^{-2} in the range of λ=1 – 20 μm.

The samples were placed in a vacuum thermostat at pressure P≈20 mTorr, at room temperature and illuminated through a zinc selenide window (ZnSe). The window has a 70% transmission in the range of λ=0.6 – 20 μm.

The current was measured with an electrometer (“Keithley”- 6517-A) and the responsivity was calculated from the I(U) measurements, as was described in section 3.4.2.

Figure 4.36 shows the current-voltage I(U) characteristics in dark and under IR illumination for the planar configuration with a-Si_xGe_y:H thermo-sensing film

(process 443); Figure 4.37 shows these characteristics for the planar configuration with a-$Si_xGe_yB_z$:H (process 479) thermo-sensing film; Figure 4.38 shows these characteristics for the planar configuration with a-$Si_xGe_yB_z$:H (process 480) thermo-sensing film and Figure 4.39 shows the same characteristics for the sandwich configuration with a-Si_xGe_y:H thermo-sensing film (process 443).

In those figures we can see the increment in current due to IR illumination, $\Delta I=I_{IR}-I_{Dark}$, where I_{IR} is the current under IR radiation and I_{Dark} is the current in dark.

The planar configuration with the a-Si_xGe_y:H (Ge_y=0.5) film has a ΔI = 5.4 nA (at bias voltage U=7 V); the planar configuration with the a-$Si_xGe_yB_z$:H (Ge_y=0.45, B_z=0.09) film has a ΔI = 65 nA (at bias voltage U=7 V); while the planar configuration with the a-$Si_xGe_yB_z$:H (Ge_y=0.55, B_z=0.07) film has a ΔI = 184 nA (at bias voltage U=7 V) and the sandwich configuration with the a-Si_xGe_y:H (Ge_y=0.5) film has a ΔI = 35 μA (at bias voltage U=4 V). The insert in those figures show the Log I(Log U) characteristics, where we can see their linear behavior.

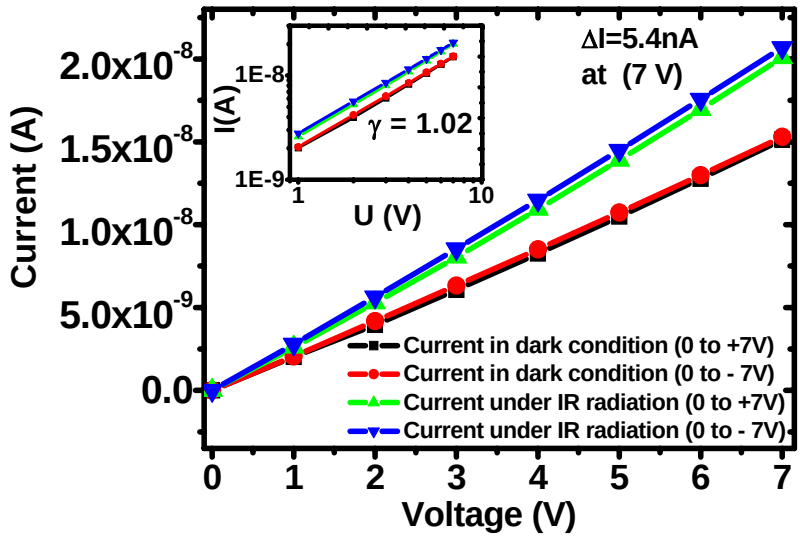

Figure 4.36. I(U) characteristics of the planar configuration micro-bolometer with the a-Si_xGe_y:H film (Ge_y=0.5).

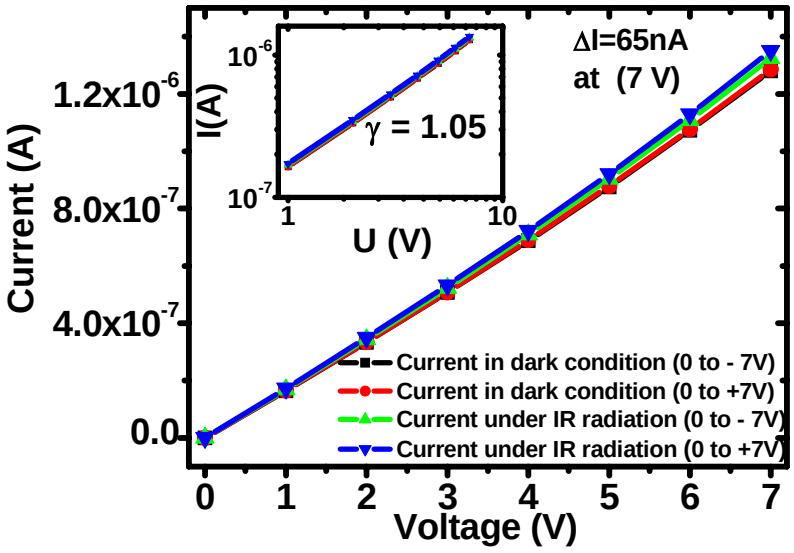

Figure 4.37. I(U) characteristics of the planar configuration micro-bolometer with the a-$Si_xGe_yB_z$:H film (Ge_y=0.45, B_z=0.09).

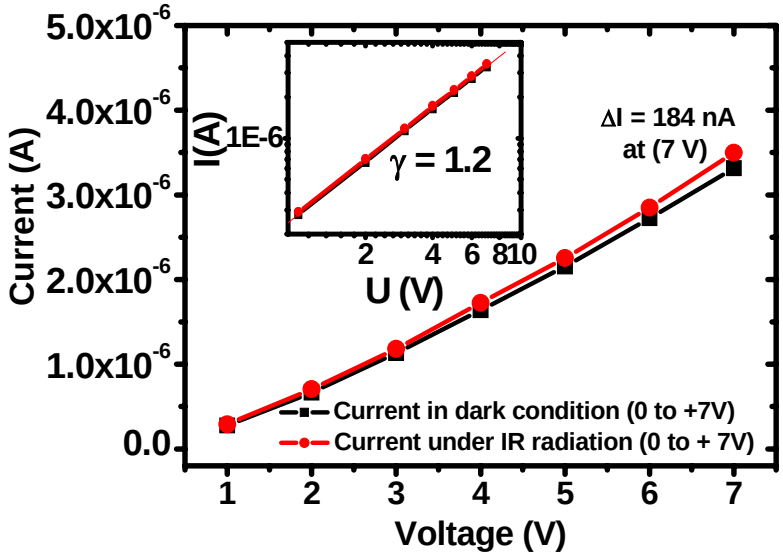

Figure 4.38. I(U) characteristics of the planar configuration micro-bolometer with the a-$Si_xGe_yB_z$:H film (Ge_y=0.55, B_z=0.07).

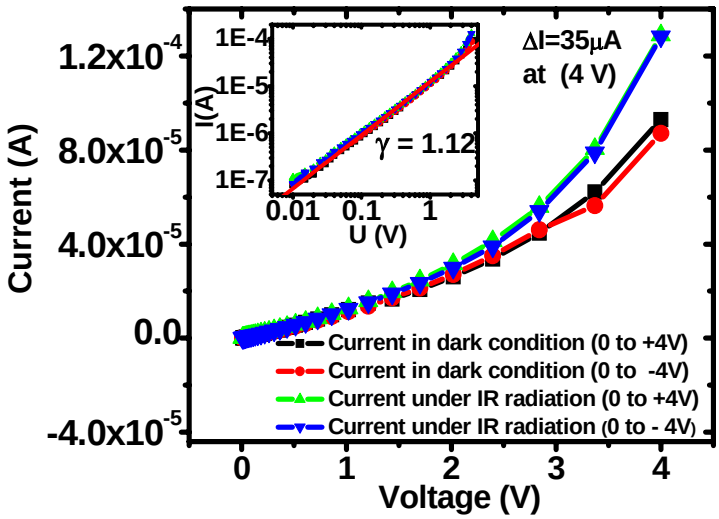

Figure 4.39. I(U) characteristics of the sandwich configuration micro-bolometer with the a-Si_xGe_y:H film (Ge_y=0.5).

The responsivity of micro-bolometers was calculated from I(U) measurements as was described in section 3.4.2. The current responsivity, R_I, is described by the equation 4.1 (equation 3.6 rewritten), where ΔI is the increment in current ($\Delta I = I_{IR} - I_{Dark}$) and $P_{incident}$ is the IR incident power in the device surface. $P_{incident}$ is described by the equation 4.2 (equation 3.7 rewritten) and is the product of the cell area, A_{cell}, by the IR source intensity, I_0.

$$R_I = \frac{\Delta I}{P_{Incident}} \qquad (4.1)$$

$$P_{Incident} = A_{cell} \cdot I_0 \qquad (4.2)$$

The intensity of the IR source is $I_0 = 0.053$ Wcm^{-2}, while the cell area is $A_{cell} = (70x10^{-4})(66x10^{-4})$ cm^2 = $4.6x10^{-5}$ cm^2 in the configurations. Therefore the IR incident power in the device surface is $P_{incident} = 2.475x10^{-6}$ W.

The planar micro-bolometer with a-Si_xGe_y:H (Ge_y=0.5) film has a R_I=2x10^{-3} A/W (at U=7 V); the planar micro-bolometer with a-$Si_xGe_yB_z$:H (Ge_y=0.45, B_z=0.09) film has a R_I= 3x10^{-2} A/W (at U=7 V); the planar micro-bolometer with a-$Si_xGe_yB_z$:H (Ge_y=0.55, B_z=0.07) film has a R_I= 7x10^{-2} A/W (at U=7 V); and the sandwich micro-bolometer with a-Si_xGe_y:H (Ge_y=0.5) film has a R_I= 14 A/W (at U=4 V). Table 4.8 shows the ΔI and R_I values obtained in the configurations. Figure 4.40 shows the voltage dependence of R_I for the planar micro-bolometer with a-Si_xGe_y:H (Ge_y=0.5) film; Figure 4.41 shows the voltage dependence of R_I for the planar micro-bolometer with a-$Si_xGe_yB_Z$:H (Ge_y=0.45, B_z=0.09) film; Figure 4.42 shows the voltage dependence of R_I for the planar micro-bolometer with a-$Si_xGe_yB_Z$:H (Ge_y=0.55, B_z=0.07) film and Figure 4.43 shows the voltage dependence of R_I for the sandwich micro-bolometer with a-Si_xGe_y:H (Ge_y=0.5) film. The insert in those figures show a relative current responsivity. Relative current responsivity is the ratio between the increment of current from dark to IR condition, ΔR_I, and the micro-bolometer resistance R_{cell} (expressed in %). The planar and sandwich structures with the intrinsic film show larger values of relative current responsivity.

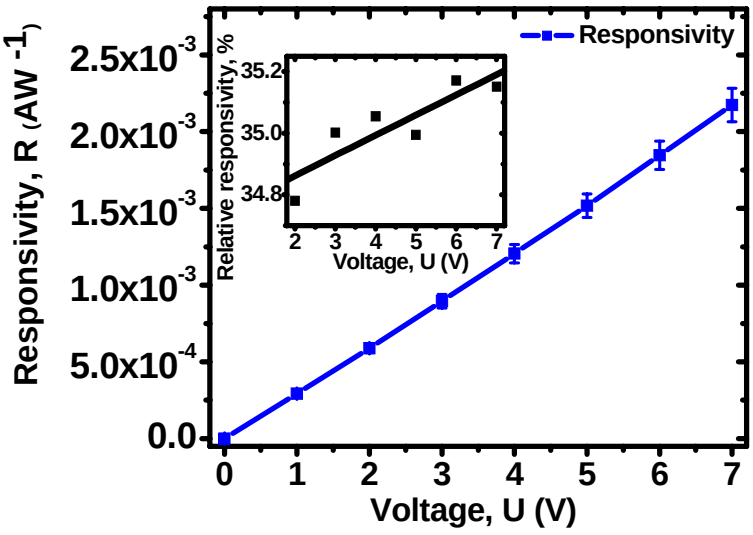

Figure 4.40. Voltage dependence of R_I for the planar micro-bolometer with a-Si_xGe_y:H (Ge_y=0.5) film.

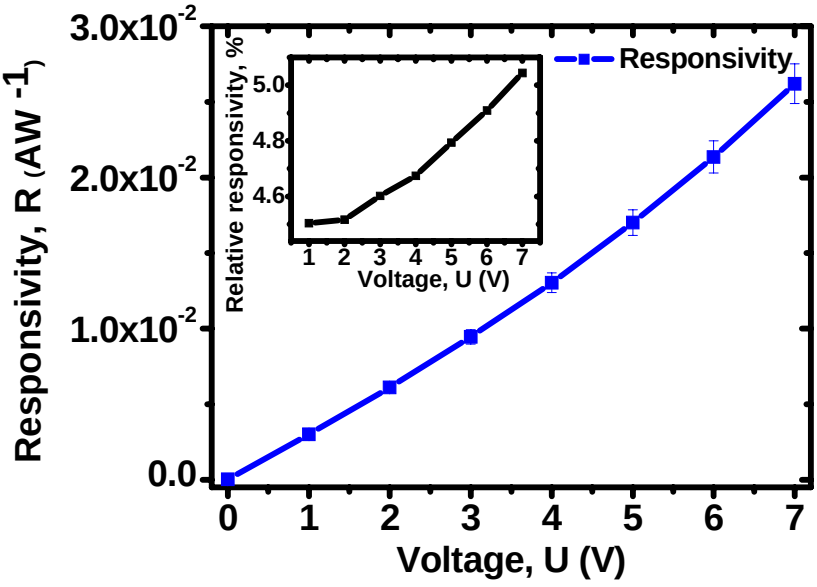

Figure 4.41. Voltage dependence of R_I for the planar micro-bolometer with a-$Si_xGe_yB_Z$:H (Ge_y=0.45, B_z=0.09) film.

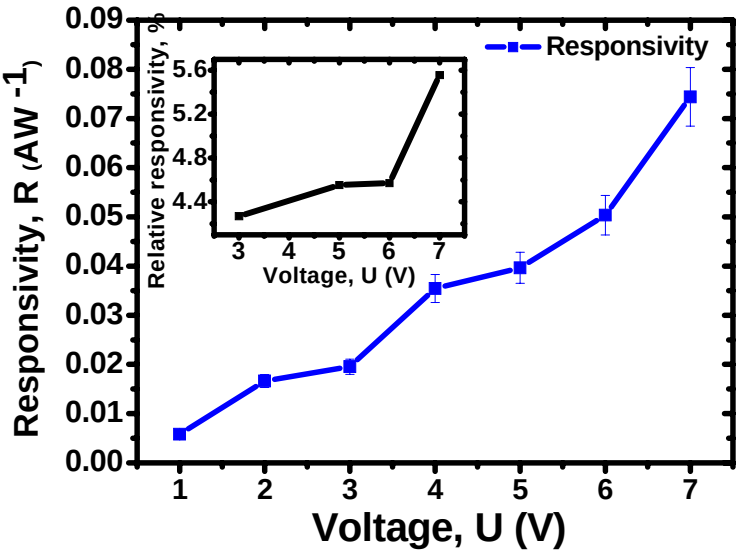

Figure 4.42. Voltage dependence of R_I for the planar micro-bolometer with a-$Si_xGe_yB_Z$:H (Ge_y=0.55, B_z=0.07) film.

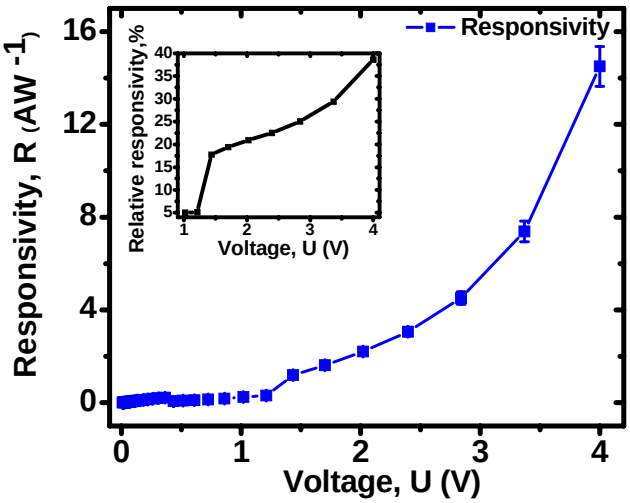

Figure 4.43. Voltage dependence of R_I for the sandwich micro-bolometer with a-Si_xGe_y:H (Ge_y=0.5) film.

The voltage responsivity, R_U, was calculated from the experimental I(U) points, the increment in voltage from dark condition to IR condition was obtained from a fixed current. Figure 4.44 shows a ΔU= 1.8 V extracted from a fixed current I = $1.5x10^{-8}$ A, in the planar structure micro-bolometer with the a-Si_xGe_y:H (Ge_y=0.5) film. Figure 4.45 shows a ΔU= 0.3 V extracted from a fixed current I = $1.35x10^{-6}$ A, in the planar structure micro-bolometer with the a-$Si_xGe_yB_Z$:H (Ge_y=0.45, B_z=0.09) film. Figure 4.46 shows a ΔU= 0.45 V extracted from a fixed current I = $3.27x10^{-6}$ A, in the planar structure micro-bolometer with the a-$Si_xGe_yB_Z$:H (Ge_y=0.55, B_z=0.07) film. Figure 4.47 shows a ΔU= 0.54 V extracted from a fixed current I = $1.16x10^{-4}$ A, in the sandwich structure micro-bolometer with the a-Si_xGe_y:H (Ge_y=0.5) film.

The planar micro-bolometer with a-Si_xGe_y:H (Ge_y=0.5) film has a R_U=$7.2x10^5$ V/W (at I=$1.5x10^{-8}$ A); the planar micro-bolometer with a-$Si_xGe_yB_z$:H (Ge_y=0.45, B_z=0.09) film has a R_U= $1.2x10^5$ V/W (at I=$1.4x10^{-6}$ A); the planar micro-bolometer with a-$Si_xGe_yB_z$:H (Ge_y=0.55, B_z=0.07) film has a R_U= $1.8x10^5$ V/W (at I=$3.27x10^{-6}$ A) and the sandwich micro-bolometer with a-Si_xGe_y:H (Ge_y=0.5) film has a R_U=

$2.2x10^5$ V/W (at $I=1.16x10^{-4}$ A). Table 4.8 shows the R_I and R_U values obtained from the different micro-bolometers configurations.

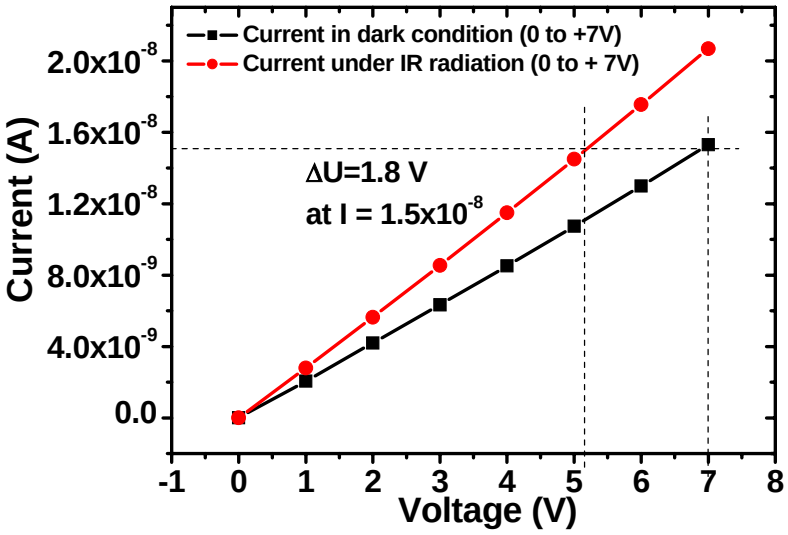

Figure 4.44. Extraction of ΔU from I(U) characteristics in a planar structure micro-bolometer with a-Si_xGe_y:H (Ge_y=0.5) thermo-sensing film.

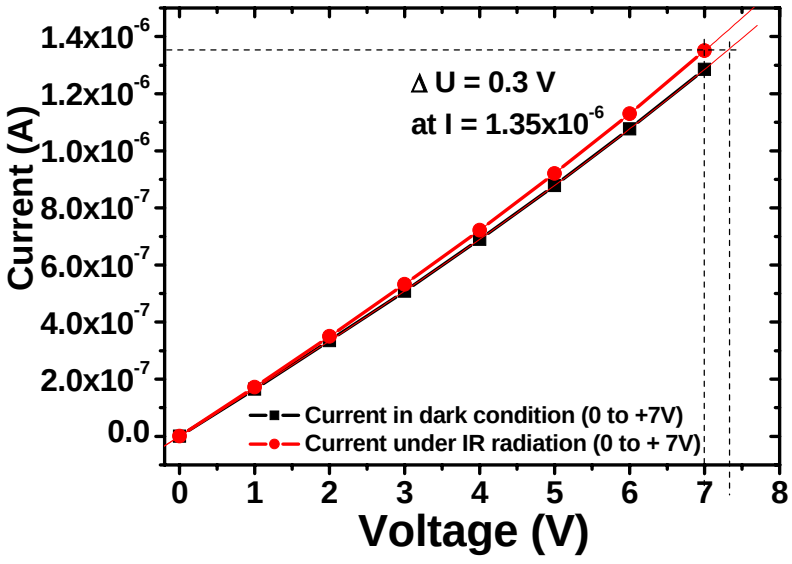

Figure 4.45. Extraction of ΔU from I(U) characteristics in a planar structure micro-bolometer with a-$Si_xGe_yB_Z$:H (Ge_y=0.45, B_z=0.09) thermo-sensing film.

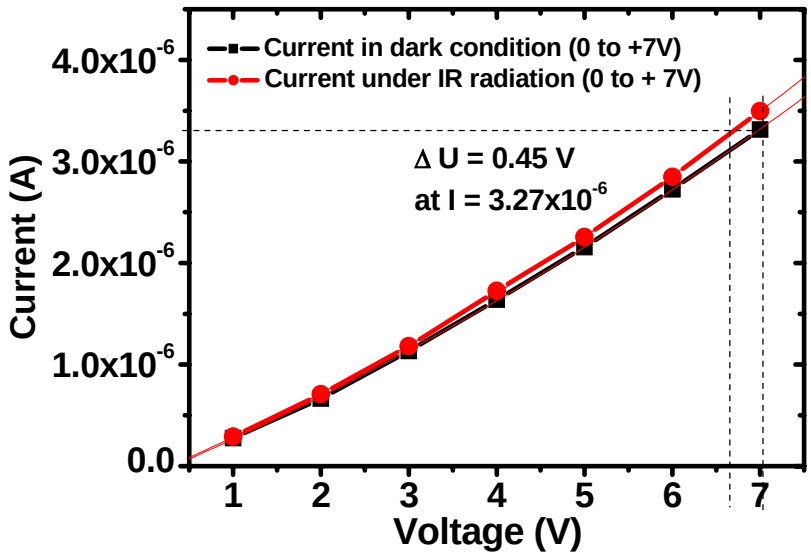

Figure 4.46. Extraction of ΔU from I(U) characteristics in a planar structure micro-bolometer with a-$Si_xGe_yB_Z$:H (Ge_y=0.55, B_z=0.07) thermo-sensing film.

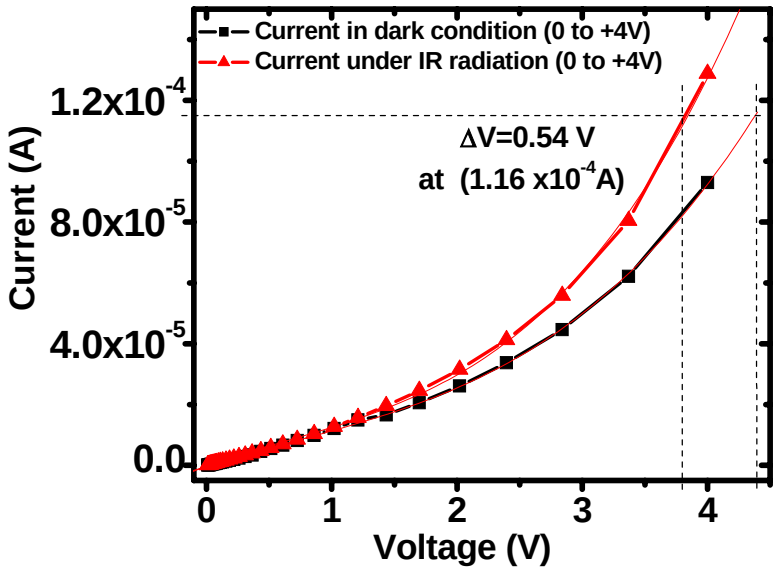

Figure 4.47. Extraction of ΔU from I(U) characteristics in a sandwich structure micro-bolometer with a-Si_xGe_y:H (Ge_y=0.5) thermo-sensing film.

Table 4.8. Current and voltage responsivity values for the four micro-bolometer configurations.

	Planar structure with a-Si_xGe_y:H film	**Planar structure with a-$Si_xGe_yB_z$:H film**	**Planar structure with a-$Si_xGe_yB_z$:H film**	**Sandwich structure with a-Si_xGe_y:H film**
Film process	443	479	480	443
$\Delta I = I_{IR} - I_{Dark}$ (A)	5.4×10^{-9} (at U=7 V)	65×10^{-9} (at U=7 V)	184×10^{-9} (at U=7 V)	$\Delta I = 35 \times 10^{-6}$ (at U=4 V)
Current Responsivity R_I (AW^{-1})	2×10^{-3}	3×10^{-2}	7×10^{-2}	14
$\Delta U = U_{IR} - U_{Dark}$ (V)	1.8 (at $I=1.5 \times 10^{-8}$)	0.3 (at $I=1.35 \times 10^{-6}$)	0.45 (at $I=3.27 \times 10^{-6}$)	0.54 (at $I=1.16 \times 10^{-4}$)
Voltage Responsivity R_U (VW^{-1})	7.2×10^5	1.2×10^5	1.8×10^5	2.2×10^5

4.8.2 Noise spectral density measurements and detectivity calculations.

Noise measurements in the micro-bolometers were performed with a lock-in amplifier ("Stanford Research Systems" - SR530). The noise of the system and the total noise (system + cell noise) were measured separately, and a subtraction of the system noise allowed us to obtain the noise of the device, as was described in section 4.3.2. The detectivity was calculated from the responsivity values and noise measurements. The current noise spectral density (NSD), $I_{cell\ noise}(f)$, of the fabricated devices with the different thermo-sensing films are shown in Figures 4.48, 4.49, 4.50 and 4.51, respectively.

The NSD in the cell is obtained as $(I_{cell\ noise}(f))^2 = (I_{system\ +\ cell\ noise}(f))^2 - (I_{system\ noise}(f))^2$, where $I_{cell\ +\ system\ noise}(f)$ is the NSD measured at the micro-bolometer with the measuring system and the $I_{system\ noise}(f)$ is the NSD measured in the system without the micro-bolometer. In noise curves we observed different slopes at different frequencies and different cone frequencies, these data are shown in Table 4.9.

The planar structure with a-Si_xGe_y:H (Ge_y=0.5) film shows $I_{cell\ noise}$ (f) ≈ 10^{-16} $AHz^{-1/2}$; the planar structure with a-$Si_xGe_yB_z$:H (Ge_y=0.45, B_z=0.09) film shows $I_{cell\ noise}$ (f) ≈ 10^{-14} $AHz^{-1/2}$; the planar structure with a-$Si_xGe_yB_z$:H (Ge_y=0.55, B_z=0.07) film presents $I_{cell\ noise}$ (f) ≈ 10^{-13} $AHz^{-1/2}$ and the sandwich structure with a-Si_xGe_y:H (Ge_y=0.5) presents $I_{cell\ noise}$ (f) ≈ 10^{-11} $AHz^{-1/2}$.

The procedure for the detectivity calculation was described in section 3.4.4 and is shown in equation 4.3 (equation 3.12 rewritten), where R_I is the current responsivity, A_{cell} is the detector area, I_{noise} is the cell NSD and Δf = 1 is the bandwidth of the measurement system.

$$D^* = \frac{R_I \cdot \sqrt{A_{cell}}}{I_{noise} / \sqrt{\Delta f}} \qquad (4.3)$$

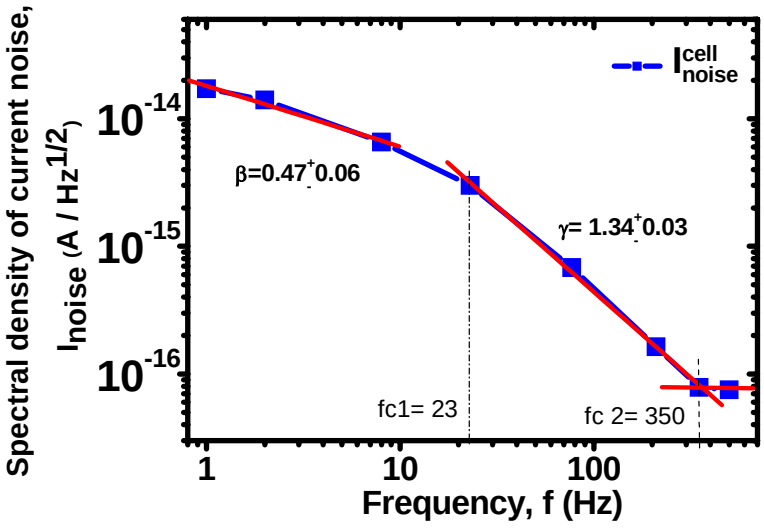

Figure 4.48. Spectral density of current noise in a planar structure micro-bolometer with an a-Si_xGe_y:H (Ge_y=0.5) thermo-sensing film.

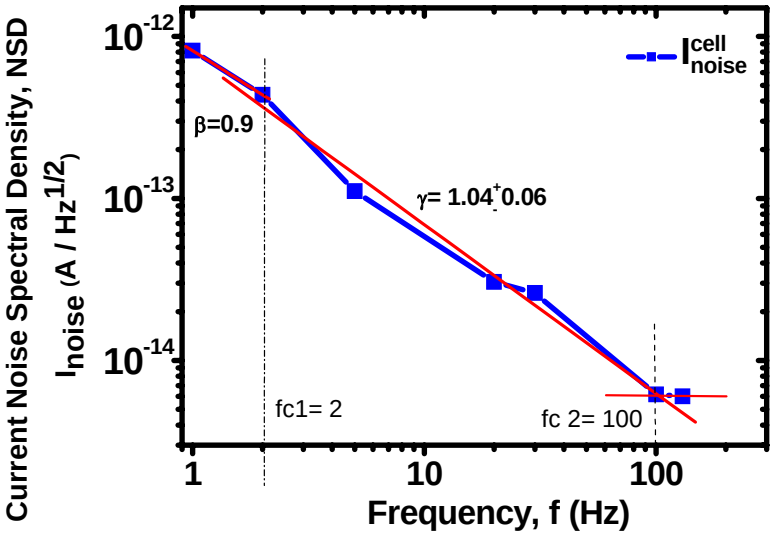

Figure 4.49. Spectral density of current noise in a planar structure micro-bolometer with an a-$Si_xGe_yB_z$:H (Ge_y=0.45, B_z=0.09) thermo-sensing film.

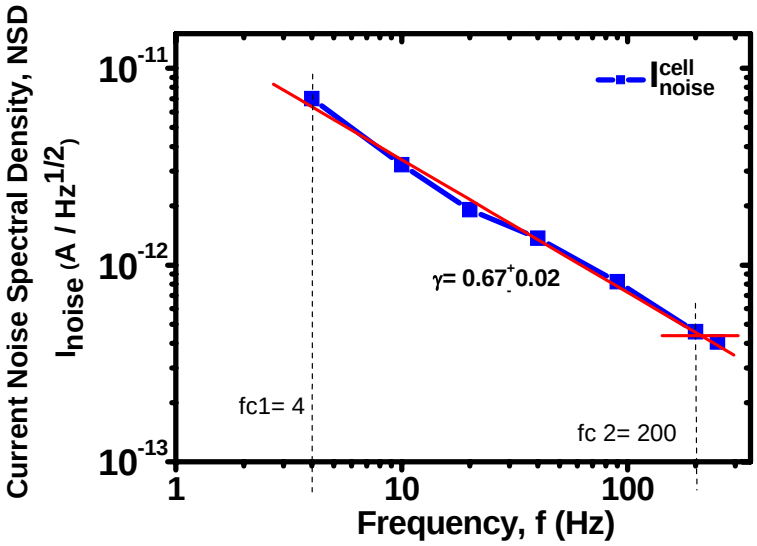

Figure 4.50. Spectral density of current noise in a planar structure micro-bolometer with an a-$Si_xGe_yB_z$:H (Ge_y=0.55, B_z=0.07) thermo-sensing film.

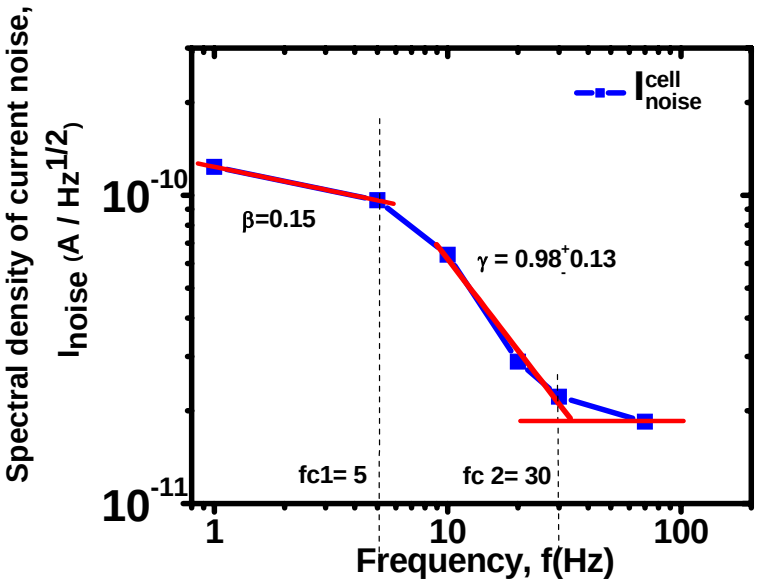

Figure 4.51. Spectral density of current noise in a sandwich structure micro-bolometer with an a-Si_xGe_y:H (Ge_y=0.5) thermo-sensing film.

Table 4.9. NSD versus frequency regions in the micro-bolometers studied.

Sample	Frequency Regions				
	Region no. 1		Region no. 2		Region no. 3
	β	fc1 (Hz.)	γ	fc2 (Hz.)	Noise level ($AHz^{-1/2}$)
Planar structure a-Si_xGe_y:H (Ge_y=0.5)	0.47 ± 0.06	23	1.34 ± 0.03	350	10^{-16}
Planar structure a-$Si_xGe_yB_z$:H (Ge_y=0.45, B_z=0.09)	0.9	2	1.04 ± 0.06	100	10^{-14}
Planar structure a-$Si_xGe_yB_z$:H (Ge_y=0.55, B_z=0.07)	----	4	0.67 ± 0.02	200	10^{-13}
Sandwich structure a-Si_xGe_y:H (Ge_y=0.5)	0.15	5	0.98 ± 0.13	30	10^{-11}

We calculated the detectivity values D^* in the four structures. For the planar structure with the a-Si_xGe_y:H (Ge_y=0.5) film we obtained $D^*= 7x10^9$ $cmHz^{1/2}W^{-1}$; for the planar structure with the a-$Si_xGe_yB_z$:H (Ge_y=0.45, B_z=0.09) film it is $D^*= 5.9x10^9$ $cmHz^{1/2}W^{-1}$; for the planar structure with the a-$Si_xGe_yB_z$:H (Ge_y=0.55, B_z=0.07) film it is $D^*= 2x10^9$ $cmHz^{1/2}W^{-1}$ and for the sandwich structure micro-bolometer with the a-Si_xGe_y:H (Ge_y=0.5) film it is $D^*= 4x10^9$ $cmHz^{1/2}W^{-1}$.

4.8.3 Thermal response time characterization.

We performed the thermal response time characterization in the four micro-bolometers configurations, the procedure for this kind of characterization was described in section 3.4.5. Figures 4.52, 4.53, 4.54 and 4.55 show a voltage pulse applied to one micro-bolometer and its current response, for the different micro-bolometer configurations.

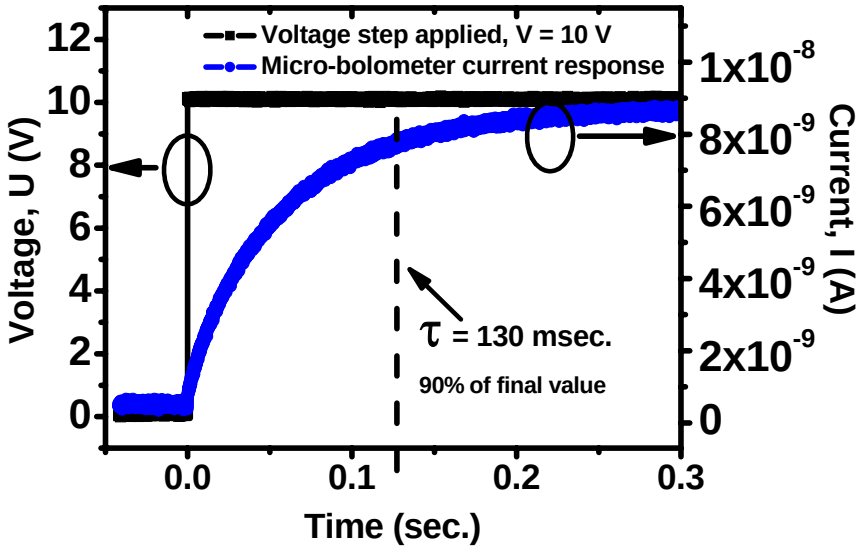

Figure 4.52. Thermal response time of a planar structure micro-bolometer with a-Si_xGe_y:H (Ge_y=0.5) thermo-sensing film .

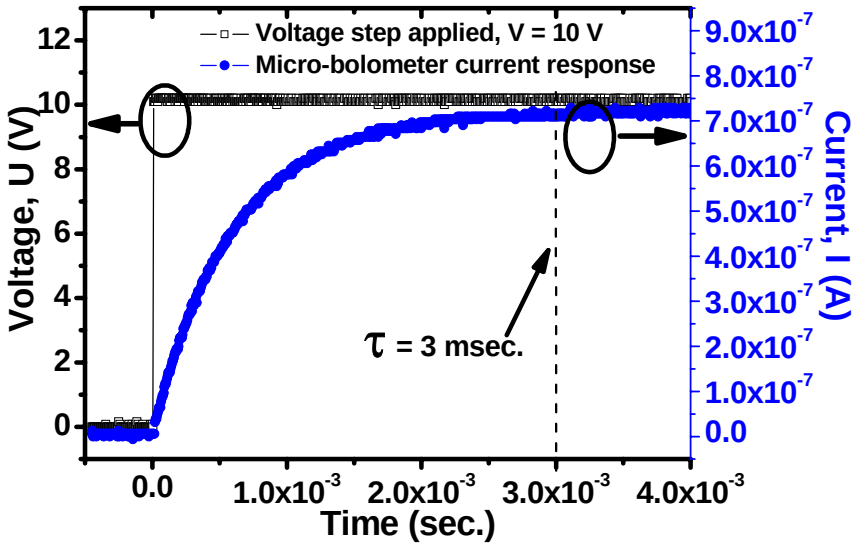

Figure 4.53. Thermal response time of a planar structure micro-bolometer with a-$Si_xGe_yB_z$:H (Ge_y=0.45, B_z=0.09) thermo-sensing film.

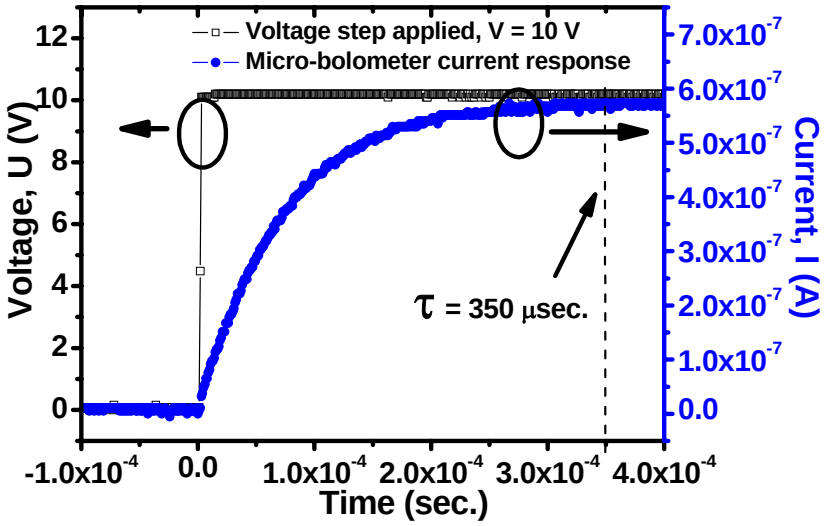

Figure 4.54. Thermal response time of a planar structure micro-bolometer with a-$Si_xGe_yB_z$:H (Ge_y=0.55, B_z=0.07) thermo-sensing film.

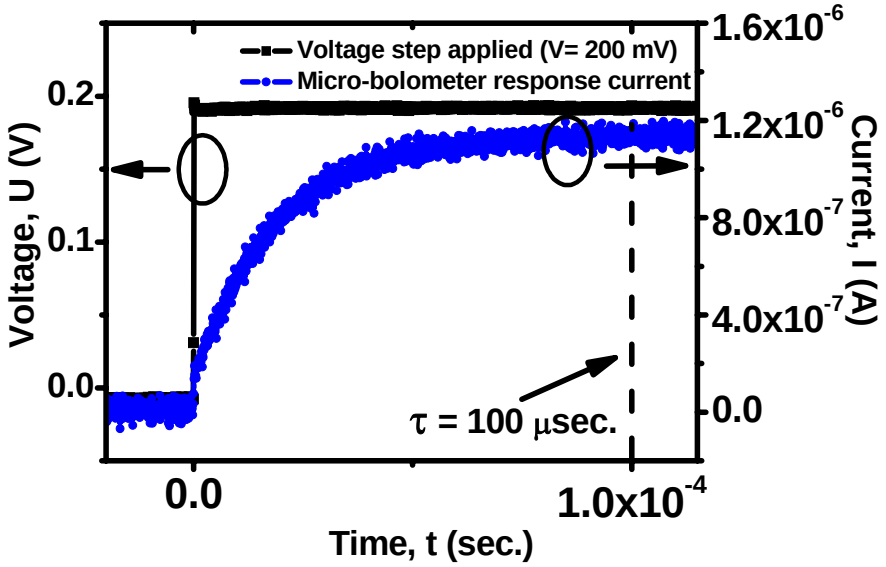

Figure 4.55. Thermal response time of a sandwich structure micro-bolometer with a-Si_xGe_y:H (Ge_y=0.5) thermo-sensing film.

The planar micro-bolometer with the intrinsic a-Si_xGe_y:H (Ge_y=0.5) film has a thermal response time τ_{th} = 130 msec., from 0 to the 90% of its final value; the planar configuration with the a-$Si_xGe_yB_z$:H (Ge_y=0.45, B_z=0.09) film shows a thermal response time τ_{th} = 3 msec., the planar configuration with the a-$Si_xGe_yB_z$:H (Ge_y=0.55, B_z=0.07) film results in a thermal response time τ_{th} = 350 μsec. and the sandwich configuration with the intrinsic a-Si_xGe_y:H (Ge_y=0.5) film has a thermal response time τ_{th} = 100 μsec.

4.8.4 Thermal capacitance and conductance characterization

Following the methodology described in section 3.4.5, we calculated the thermal capacitance, C_{th} and the thermal conductance, G_{th} in the four micro-bolometers studied. Table 4.10 shows those results.

Table 4.10. Results of thermal characterization in the four micro-bolometers.

	Planar structure with a-Si_xGe_y:H	**Planar structure with a-$Si_xGe_yB_z$:H**	**Planar structure with a-$Si_xGe_yB_z$:H**	**Sandwich structure with a-Si_xGe_y:H**
Film process	443	479	480	443
Thermal constant, τ_{th}, (sec.)	$1.3x10^{-1}$	$3x10^{-3}$	$3.5x10^{-4}$	$1x10^{-4}$
Thermal conductance, G_{th}, (WK^{-1})	$3.8\ x10^{-7}$	$3.2x10^{-6}$	$3.1x10^{-6}$	$4.7x10^{-6}$
Thermal capacitance, C_{th}, (JK^{-1})	$4.9x10^{-8}$	$1x10^{-8}$	$1x10^{-9}$	$4.7x10^{-10}$
Cell resistance, R_{cell}, (Ω)	$3.7x10^{8}$	$5x10^{6}$	$2x10^{-6}$	$1.17x10^{5}$

4.8.5 Temperature dependence of thermal conductance and calibration curve

Following the methodology presented in section 3.4.7, there were obtained the calibration and the temperature dependence of thermal conductance (thermal resistance) curves in the different micro-bolometers. Figures 4.56 and 4.57 show the calibration and thermal resistance curves in the planar structure micro-bolometer with a-Si_xGe_y:H (Ge_y=0.5) thermo-sensing film.

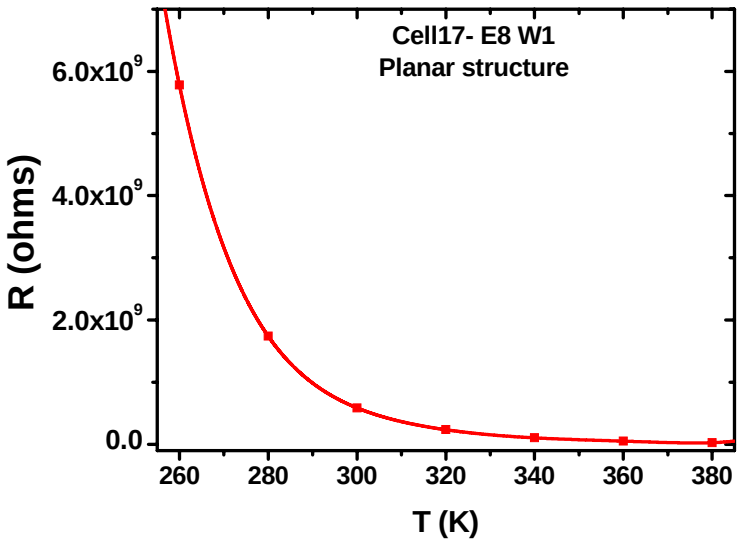

Figure 4.56. Calibration curve of a planar structure micro-bolometer with a-Si_xGe_y:H (Ge_y=0.5) thermo-sensing film.

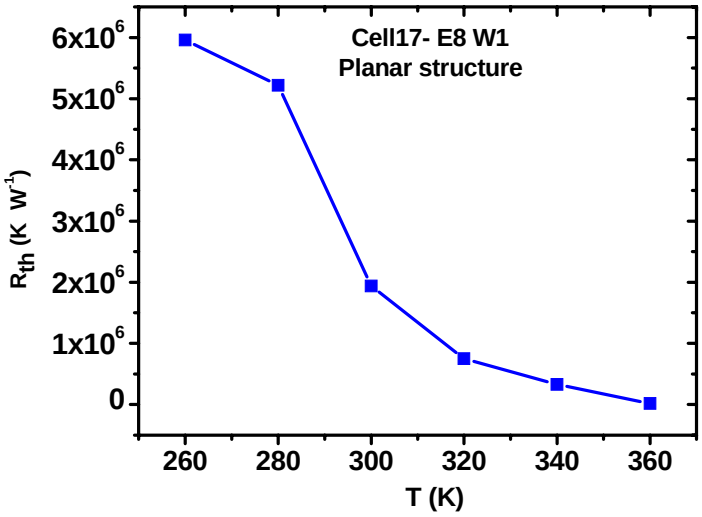

Figure 4.57. Thermal resistance of a planar structure micro-bolometer with a-Si_xGe_y:H (Ge_y=0.5) thermo-sensing film.

Figures 4.58 and 4.59 show the calibration and thermal resistance curves in the planar structure micro-bolometer with a-$Si_xGe_yB_z$:H (Ge_y=0.45, B_z=0.09) film.

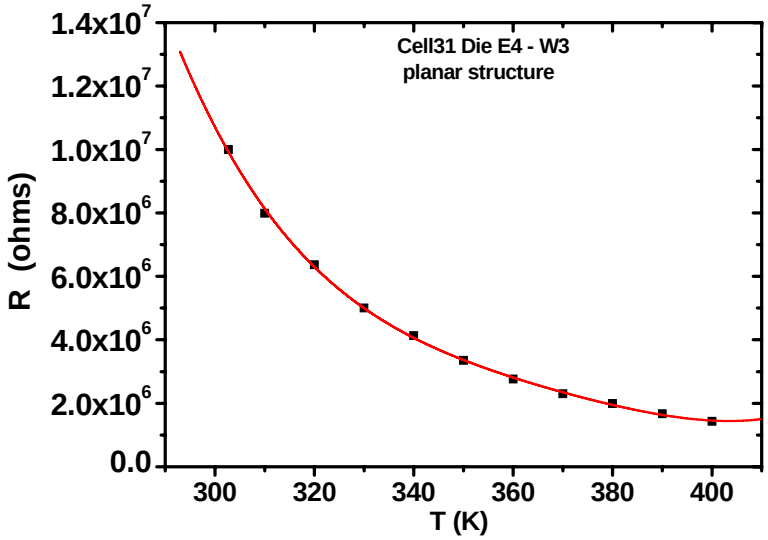

Figure 4.58. Calibration Curve of a planar structure micro-bolometer with a-$Si_xGe_yB_z$:H (Ge_y=0.45, B_z=0.09) thermo-sensing film.

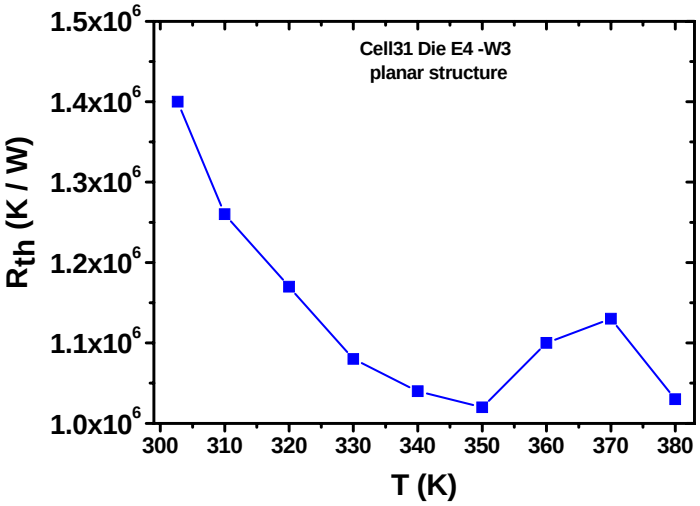

Figure 4.59. Thermal resistance of a planar structure micro-bolometer with a-$Si_xGe_yB_z$:H (Ge_y=0.45, B_z=0.09) thermo-sensing film.

Figures 4.60 and 4.61 show the calibration and thermal resistance curves in the planar structure micro-bolometer with a-$Si_xGe_yB_z$:H (Ge_y=0.55, B_z=0.07) film.

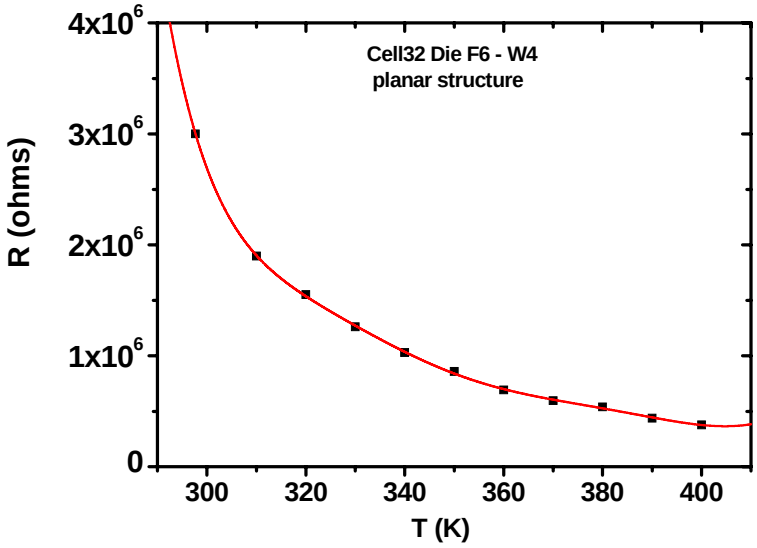

Figure 4.60. Calibration curve of a planar structure micro-bolometer with a-$Si_xGe_yB_z$:H (Ge_y=0.55, B_z=0.07) thermo-sensing film.

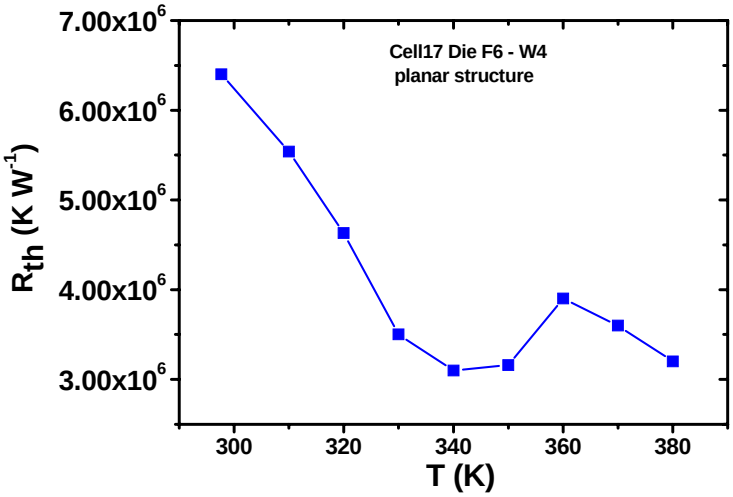

Figure 4.61. Thermal resistance of a planar structure micro-bolometer with a-$Si_xGe_yB_z$:H (Ge_y=0.55, B_z=0.07) thermo-sensing film.

In the sandwich structure micro-bolometers there was not possible to perform this kind of characterization, since they were broken with the previous measurements.

4.9 Characterization of one dimensional un-cooled micro-bolometer arrays.

In this section is described the characterization performed in arrays, using the experimental read-out described in section 3.5.1, current voltage characteristics, responsivity and detectivity were obtained in every cell of the arrays. Specific arrays characteristics, described in section 3.5.5, were measured in the arrays also.

4.9.1 Wafer mapping of four processes of 1-D arrays.

In section 4.7.1 was described the fabrication process of 1-D micro-bolometer arrays. There were fabricated four different processes of 1-D micro-bolometer arrays with different thermo-sensing films (one wafer by process). Table 4.11 listed the main characteristics of the four processes of 1-D micro-bolometer arrays.

Table 4.11 Characteristics of 1-D arrays available for characterization.

Process number	**Wafer number**	**Micro-bolometer structures in the array**	**Thermo-sensing film**	**Ge_y**	**B_z**	**E_a (eV)**
443	Wafer #1	Planar	a-Si_xGe_y:H	0.5	-	0.37
443	Wafer #2	Sandwich	a-Si_xGe_y:H	0.5	-	0.37
479	Wafer #3	Planar	a-$Si_xGe_yB_z$:H	0.45	0.09	0.22
480	Wafer #4	Planar	a-$Si_xGe_yB_z$:H	0.55	0.07	0.20

In order to find the arrays with the largest yield for further characterization, a map of each wafer was made and a letter followed by a number was assigned to every die. The cells were electrically tested in several arrays of each wafer in order to obtain the real yield of the micro-bolometer arrays.

Figure 4.62 shows the map of wafer no. 1, which contain 1-D arrays of planar structure micro-bolometers with an a-Si_xGe_y:H (Ge_y=0.5) intrinsic film (process 443). In the wafer map the dark dies are those which were damaged during the fabrication process. We measured I(U) characteristics in 15 arrays containing 480 cells (micro-bolometers). From these measurements we calculated the yield of these arrays, taking into account for yield just the cells that are electrically active (cells in open circuit or short circuit were considered as cells in bad conditions).

The yield of the 15 arrays tested in wafer no. 1 is 47%, however we found arrays with yield as high as 80 %, these results are shown in Figure 4.63.

Figure 4.64 shows the map of wafer no. 2, which contain 1-D arrays of sandwich structure micro-bolometers with an a-Si_xGe_y:H (Ge_y=0.5) intrinsic film (process 443). In this wafer we tested 22 arrays containing 704 cells. From these measurements we calculated the yield of these arrays. The yield of the 22 arrays tested in wafer no. 2 is 9%. We observed a very low yield in the sandwiched structure devices, these results are shown in Figure 4.65. The sandwich structure micro-bolometers are more complex devices and its fabrication consists of more steps than those of the planar configuration micro-bolometers, this can explain the reason of low yield in these structures.

Figure 4.66 shows the map of wafer no. 3, which contain 1-D arrays of planar structure micro-bolometers with an a-$Si_xGe_yB_Z$:H (Ge_y=0.45, B_z=0.09) thermo-sensing film (process 479). We tested 19 arrays containing 608 micro-bolometers. From these measurements we calculated the yield of these arrays. The yield of the 19 arrays tested in wafer no. 3 is 59%, however we found arrays with yield as large as 90%, these results are shown in Figure 4.67.

Figure 4.68 shows the map of wafer no. 4, which contain 1-D arrays of planar structure micro-bolometers with an a-$Si_xGe_yB_Z$:H (Ge_y=0.55, B_z=0.07) thermo-sensing film (process 480). We measured I(U) characteristics in 18 arrays containing 576 micro-bolometers. From these measurements we calculated the yield of these arrays. The yield of the 18 arrays tested in wafer no. 4 is 47%, however we found 1-D arrays with yield as large as 80%, as is shown in Figure 4.69. Table 4.12 shows the 1-D arrays with larger yield of the four processes of 1-D micro-bolometer arrays, these arrays can be packed in order to be characterized with the experimental read out. The 1-D arrays of sandwich structures presented very low yield, and during testing several cells were broken, therefore this kind of samples are not suitable for packing.

Table 4.12. 1-D arrays with larger yield, of 4 different processes.

		Wafer no. 1 Process 443	**Wafer no. 2 Process 443**	**Wafer no. 3 Process 479**	**Wafer no. 4 Process 480**
Thermo-sensing film		a-Si_xGe_y:H Ge_y=0.5	a-Si_xGe_y:H Ge_y=0.5	a-$Si_xGe_yB_z$:H Ge_y=0.45, B_z=0.09	a-$Si_xGe_yB_z$:H Ge_y=0.55, B_z=0.07
Structure		planar	sandwich	planar	planar
Wafer yield (%)		46	9	59	47
Arrays yield	50 %	E4, F4, H6, D8	----	G5, G6, D6, C7, D8, G9	G5
	60 %	H4, G7, E8	----	D5, E5	H5, I5, J6, G7
	70 %	----	----	F3, F4, B5, F9	F5, H6
	80 %	F7	----	C4	F6, G6
	90 %	----	----	E3, E4, D4	----

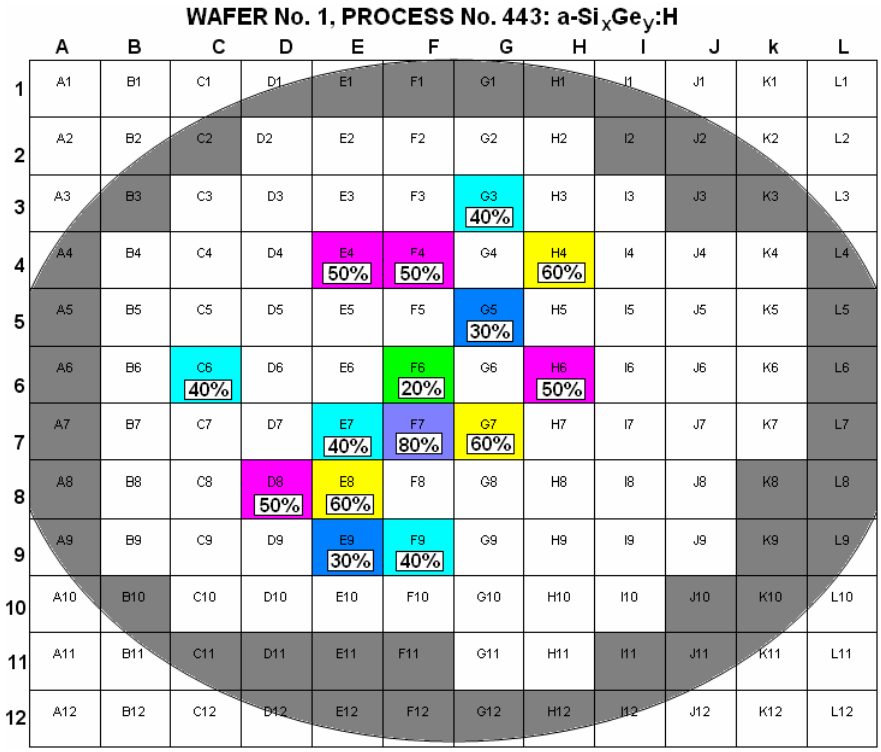

Figure 4.62. Map of wafer no. 1 of 1-D planar micro-bolometer arrays, process 443.

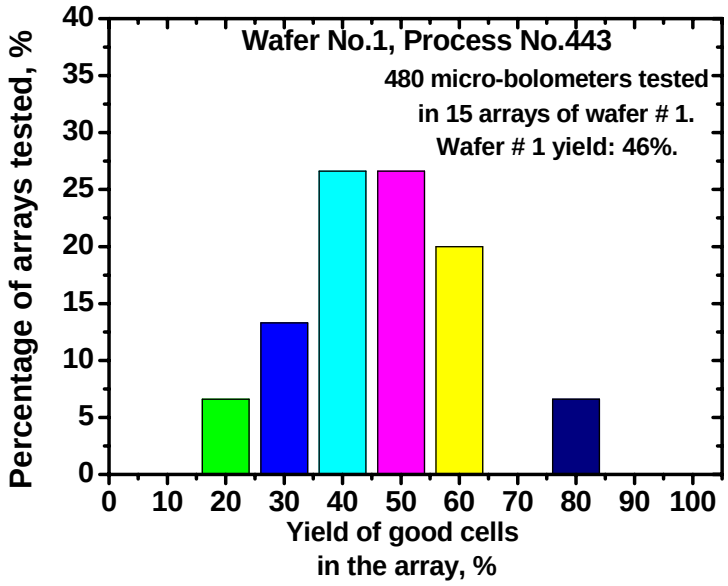

Figure 4.63. Yield of 15 arrays tested in wafer no. 1, containing 1-D planar micro-bolometer arrays with a-Si$_x$Ge$_y$:H (Ge$_y$=0.5) thermo-sensing film.

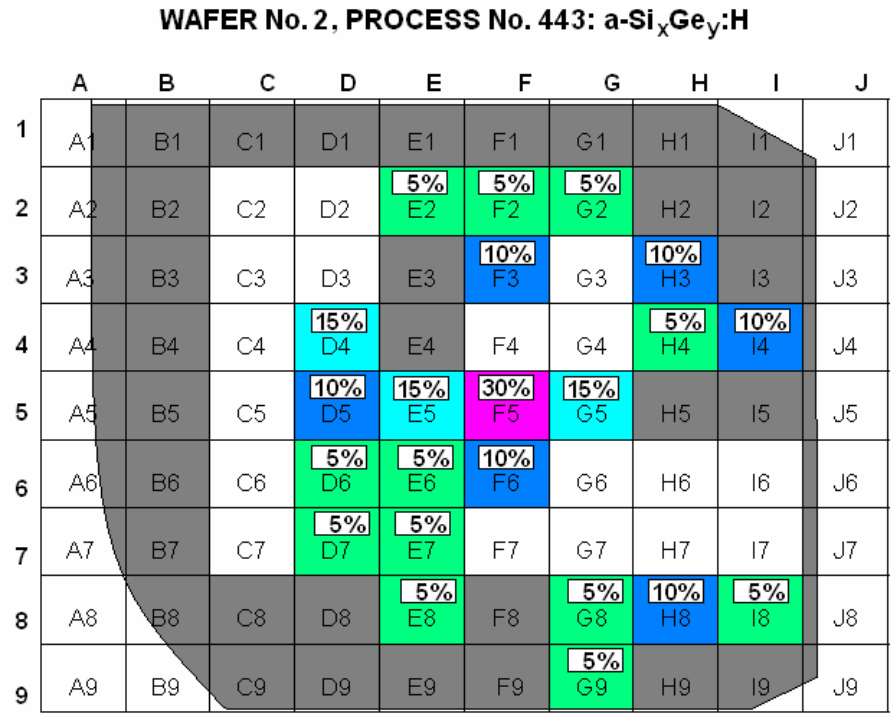

Figure 4.64. Map of wafer no. 2 containing 1-D sandwich micro-bolometer arrays, with a-Si$_x$Ge$_y$:H (Ge$_y$=0.5) thermo-sensing film, process 443.

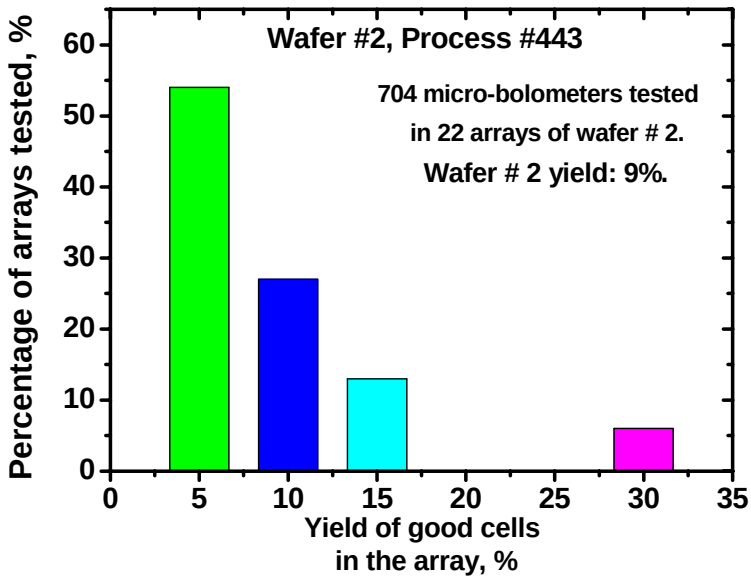

Figure 4.65. Yield of 22 arrays tested in wafer no. 2, containing 1-D sandwich micro-bolometer arrays with a-Si$_x$Ge$_y$:H (Ge$_y$=0.5) thermo-sensing film.

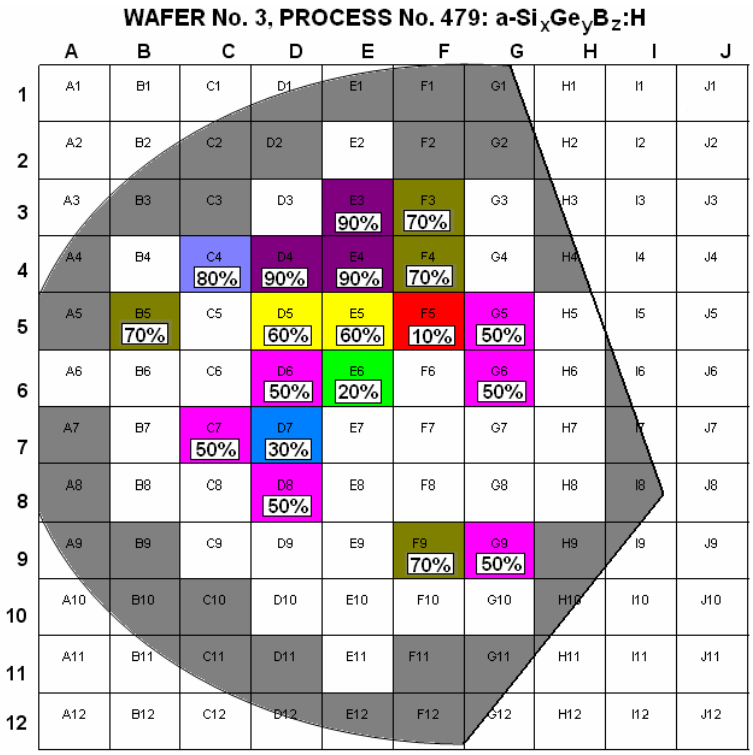

Figure 4.66. Map of wafer no. 3, containing 1-D planar micro-bolometer arrays with a-Si$_x$Ge$_y$B$_z$:H (Ge$_y$=0.45, B$_z$=0.09) thermo-sensing film, process 479.

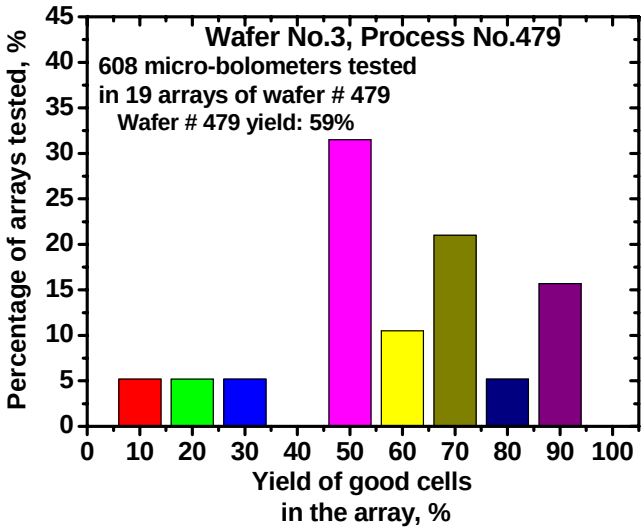

Figure 4.67. Yield of 19 arrays tested in wafer no. 3, containing 1-D planar micro-bolometer arrays with a-Si$_x$Ge$_y$B$_z$:H (Ge$_y$=0.45, B$_z$=0.09) film.

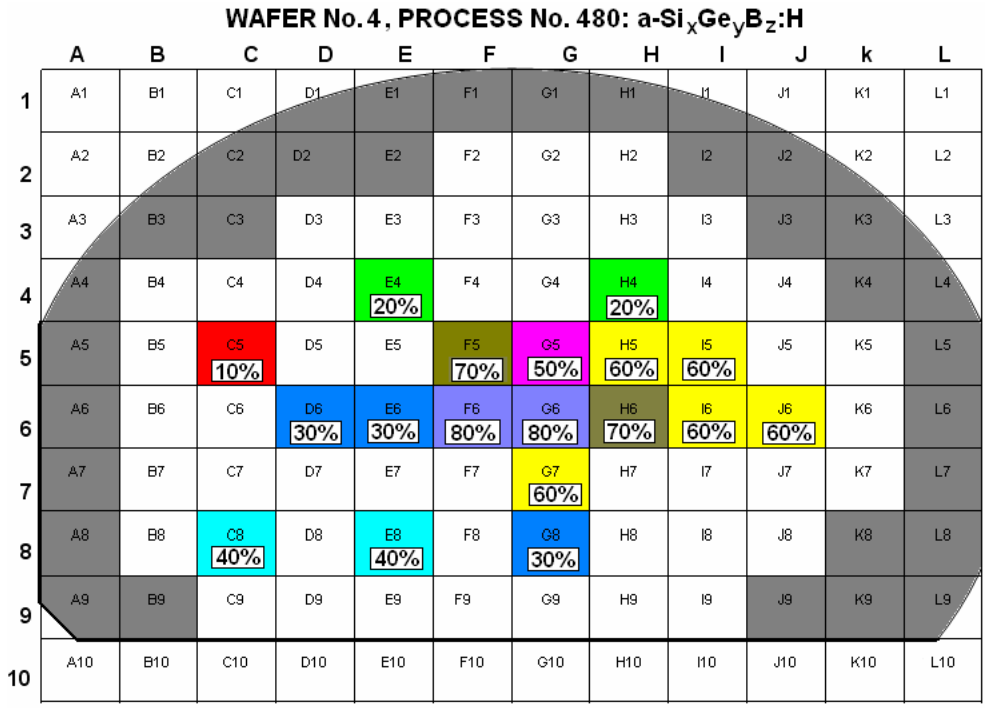

Figure 4.68. Map of wafer no. 4 containing 1-D planar micro-bolometer arrays with a-$Si_xGe_yB_z$:H (Ge_y=0.55, B_z=0.07) thermo-sensing film, process 480.

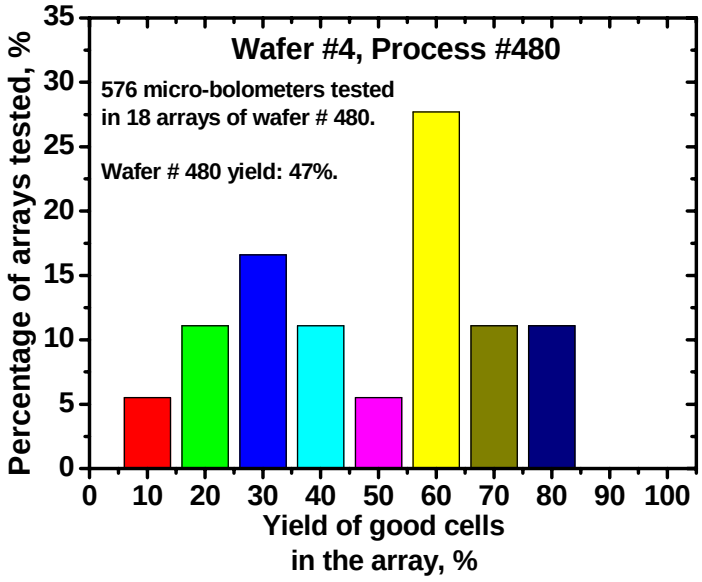

Figure 4.69. Yield of 18 arrays tested in wafer no. 4, containing 1-D planar micro-bolometer arrays with a-$Si_xGe_yB_z$:H (Ge_y=0.55, B_z=0.07) film.

4.9.2 Encapsulation of 1-D arrays for characterization.

In the previous section we described the mapping of the wafers of the four processes of 1-D arrays fabricated. We found the arrays with larger yield, which are shown in Table 4.12. We selected six 1-D micro-bolometer arrays in order to encapsulate them in a 40 legs box (DIP CSB04075). The arrays of sandwich structures were not encapsulated since they resulted in a very low yield.

Table 4.13. 1-D arrays encapsulated for further characterization.

	Process 443	**Process 479**	**Process 480**
Thermo-sensing film	a-Si_xGe_y:H Ge_y=0.5	a-$Si_xGe_yB_z$:H Ge_y=0.45, B_z=0.09	a-$Si_xGe_yB_z$:H Ge_y=0.55, B_z=0.07
Structure	Planar	planar	Planar
Arrays Encapsulated–yield	E8 – 56%	C4 – 72%	F5 – 69%
	F7 – 65%	D4 – 75%	F6 – 87%

Table 4.13 shows the general characteristics of the 1-D arrays encapsulated. As we see in the table, we decrease the yield in some arrays during bonding.

4.9.3 Measurements of current-voltage characteristics I(U) in dark and under infrared radiation, responsivity and detectivity calculations.

In this section, we present the characterization of 1-D un-cooled micro-bolometer arrays, based on an amorphous silicon-germanium intrinsic film, a-Si_xGe_y:H (process 443) and amorphous silicon-germanium-boron thermo-sensing films, a-$Si_xGe_yB_z$:H (process 479 and 480). Current-voltage characteristics I(U) in dark and under IR radiation have been measured in the micro-bolometer arrays with the three different thermo-sensing films in order to characterize and compare their performance characteristics, such as responsivity, R, and detectivity, D^*. For characterization the arrays encpasulated were placed in a vacuum thermostat with a

zinc selenide window (ZnSe) with a transmission of 70% in the range of λ=0.6–20 μm, at pressure P≈20 mTorr and at room temperature.

We performed current-voltage I(U) measurements in the arrays, in dark and under IR illumination. We employed an experimental external readout circuit, which was described in section 3.5.1. The readout system is computer controlled and allows us to apply a voltage pulse to the micro-bolometers in the array, with a variable frequency and measure and save their currents. For the IR illumination we employed a SiC globar source, with an intensity $I_0=5.3x10^{-2}$ W/cm^2 and spectrum in the range λ=1–20 μm. From I(U) characterization we obtained the responsivity of the micro-bolometer arrays. In order to compare the performance characteristics of the fabricated 1-D arrays of planar structure micro-bolometers with 3 different thermo-sensing films, we have selected one array of each type for a characterization.

The 1-D array of planar micro-bolometers with an a-Si_xGe_y:H film (Ge_y=0.5, process 443) is E8 and has a yield of 56%; the 1-D array of planar micro-bolometers with an a-$Si_xGe_yB_z$:H film (Ge_y=0.45, B_z=0.09, process 479) is D4 and has a yield of 75%; and the 1-D array of planar micro-bolometers with an a-$Si_xGe_yB_z$:H film (Ge_y=0.55, B_z=0.07, process 480) is F5 and has a yield of 69%.

With the experimental readout circuit we applied a voltage pulse sequentially to each micro-bolometer in the 1-D arrays and saved the current in a data file. The voltage pulse applied to each micro-bolometer had an amplitude of U = 7V and a duration t = 500 msec. Figure 4.70 shows the current values for dark and IR illumination conditions when a voltage pulse is applied to each micro-bolometer in the array E8 with an a-Si_xGe_y:H intrinsic film (Ge_y=0.5); Figure 4.71 shows those values for the array D4 with an a-$Si_xGe_yB_z$:H film (Ge_y=0.45 and B_z=0.09) and Figure 4.72 shows the same values for the array F5 with an a-$Si_xGe_yB_z$:H film (Ge_y=0.55 and B_z=0.07). From I(U) characteristics we calculated the ΔI in every cell of the arrays. ΔI was obtained by subtracting I_{IR}-I_{Dark} individually in every cell.

We observed an average ΔI≈1 nA for the a-Si_xGe_y:H intrinsic film micro-bolometers with a maximum value ΔI=2.5 nA; while in the a-$Si_xGe_yB_z$:H film (Ge_y=0.45, B_z=0.09) micro-bolometers we observed an average ΔI≈65 nA, with a

maximum value ΔI=132 nA and in the a-$Si_xGe_yB_z$:H film (Ge_y=0.55, B_z=0.07) micro-bolometers we observed an average ΔI≈100 nA, with a maximum value ΔI = 197 nA.

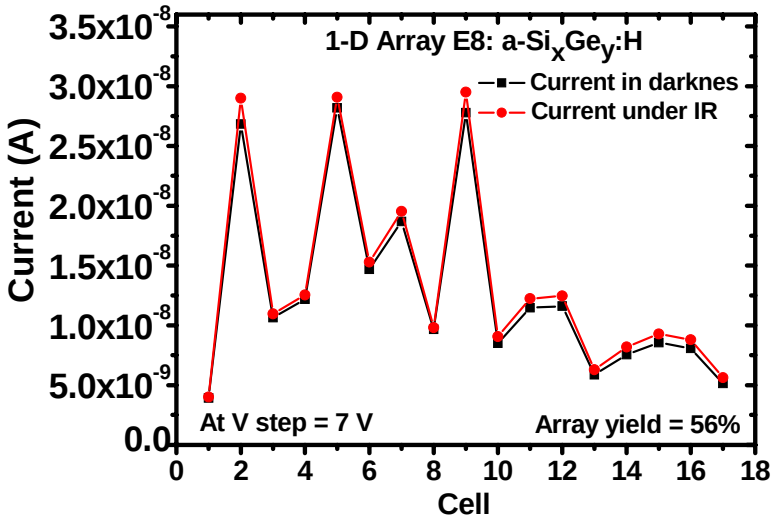

Figure 4.70. Current values for dark and IR illumination conditions for the array E8 with an a-Si_xGe_y:H intrinsic film (process 443).

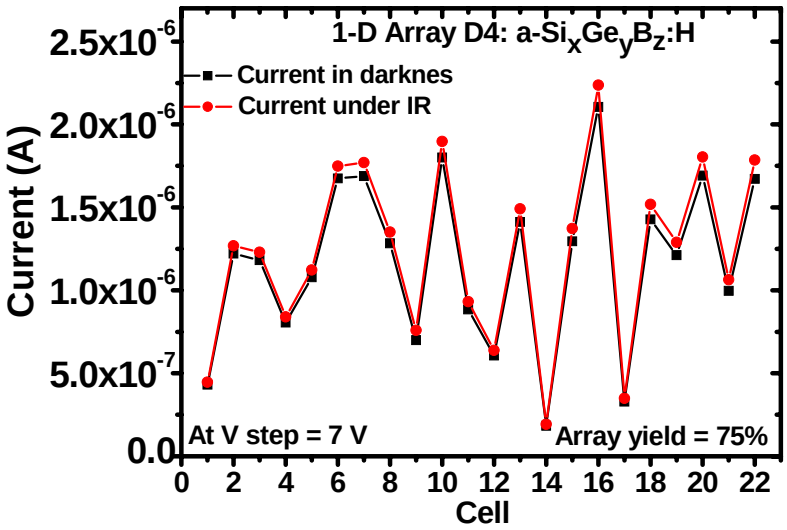

Figure 4.71. Current values for dark and IR illumination conditions for the array D4 with an a-$Si_xGe_yB_z$:H intrinsic film (process 479).

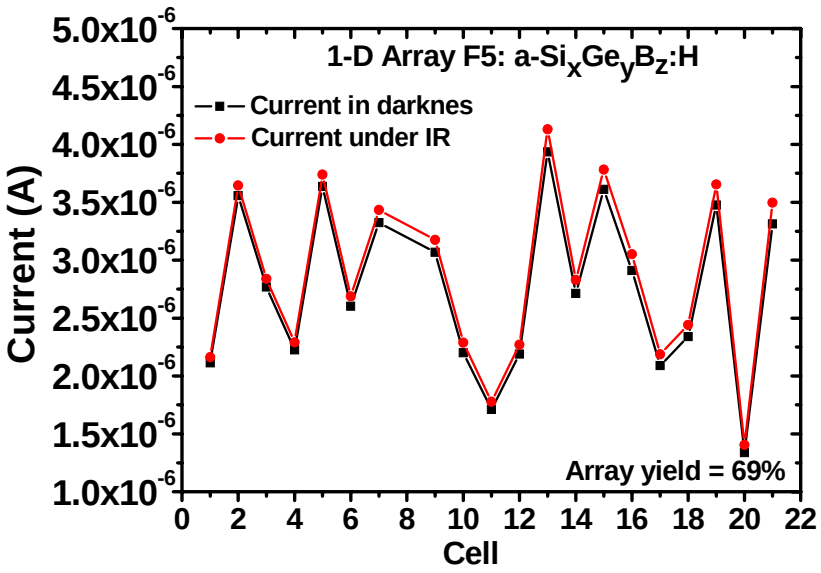

Figure 4.72. Current values for dark and IR illumination conditions for the array F5 with an a-$Si_xGe_yB_z$:H intrinsic film (process 480).

We calculated the current responsivity, R_I, in every cell of the arrays. In the intrinsic film micro-bolometer array E8 we observed an average $R_I \approx 3x10^{-4}$ AW^{-1} with a maximum value $R_I = 8.4x10^{-4}$ AW^{-1}, as is shown in Figure 4.73; while in the boron alloy micro-bolometer array D4 we observed an average $R_I \approx 2.5x10^{-2}$ AW^{-1} with a maximum value $R_I = 5x10^{-2}$ AW^{-1}, as is shown in Figure 4.74; and in the boron alloy micro-bolometer array F5 we observed an average $R_I \approx 4.1x10^{-2}$ AW^{-1} with a maximum value $R_I = 7.5x10^{-2}$ AW^{-1}, as is shown in Figure 4.75.

We performed noise measurements in the 3 micro-bolometer in every array obtaining an average spectral density of current noise, I_{noise}, on each array. For the intrinsic film (Ge_y=0.5) micro-bolometers we obtained an average $I_{noise} \approx 1x10^{-15}$ $AHz^{-1/2}$; while for the boron alloy (Ge_y=0.45, B_z=0.09) micro-bolometers we obtained an average $I_{noise} \approx 5x10^{-14}$ $AHz^{-1/2}$; and for the boron alloy (Ge_y=0.55, B_z=0.07) micro-bolometers we obtained an average $I_{noise} \approx 3x10^{-13}$ $AHz^{-1/2}$.

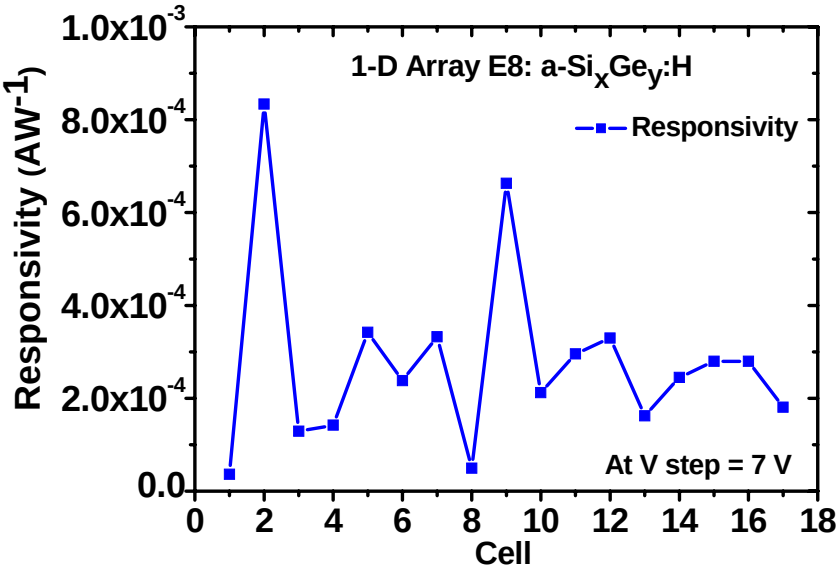

Figure 4.73. Responsivity values of the array E8 with an a-Si_xGe_y:H intrinsic film (process 443).

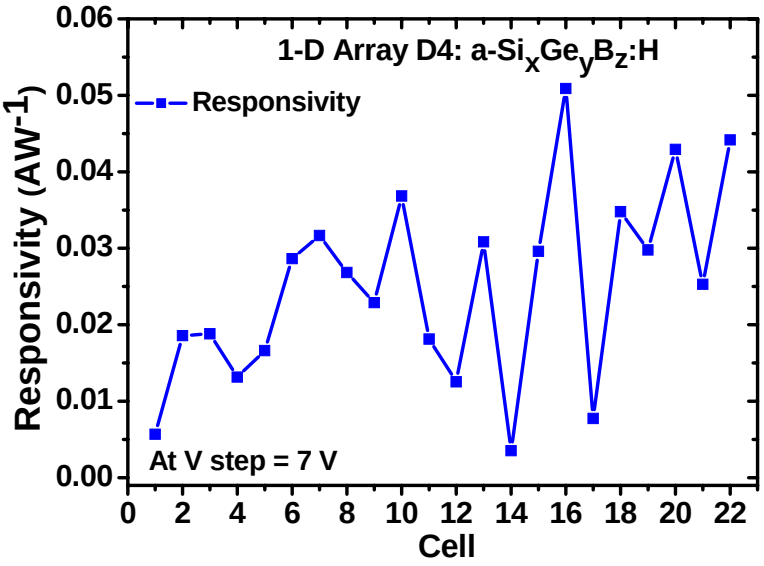

Figure 4.74. Responsivity values of the array D4 with an a-$Si_xGe_yB_z$:H intrinsic film (process 479).

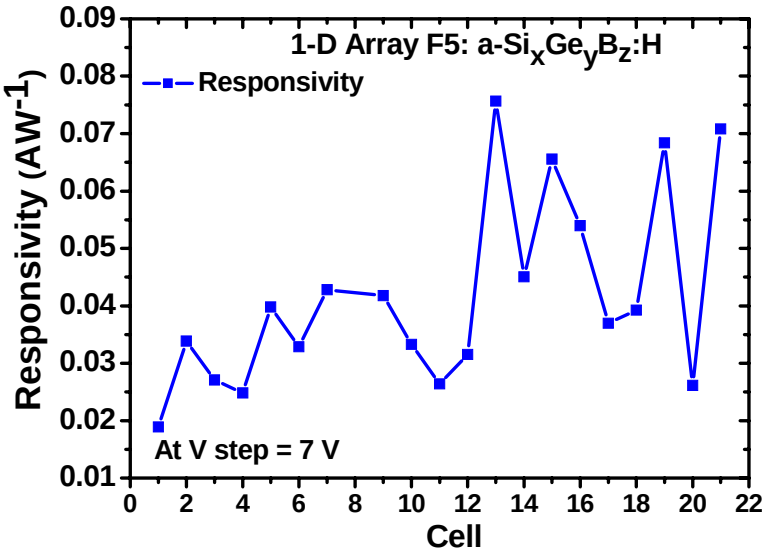

Figure 4.75. Responsivity values of the array F5 with an a-$Si_xGe_yB_z$:H intrinsic film (process 480).

From these results we calculated the detectivity, D^*, in the arrays. Figure 4.76 shows the D^* in every micro-bolometer in the array E8 with the intrinsic film (Ge_y=0.5); while Figure 4.77 shows the D^* values for the micro-bolometers in the array D4 with the boron alloy (Ge_y=0.45 and B_z=0.09); and Figure 4.78 shows the D^* values for the micro-bolometers in the array F5 with the boron alloy (Ge_y=0.55 and B_z=0.07).

In the intrinsic film micro-bolometer array E8 we observed an average $D^* \approx 1.9x10^9$ $cmHz^{1/2}W^{-1}$ with a maximum value $D^* = 5.6x10^9$ $cmHz^{1/2}W^{-1}$; while in the boron alloy micro-bolometer array D4 we observed an average $D^* \approx 3.4x10^9$ $cmHz^{1/2}W^{-1}$ with a maximum value $D^* = 6.9\ x10^9$ $cmHz^{1/2}W^{-1}$; and in the boron alloy micro-bolometer array F5 we observed an average $D^* \approx 1\ x10^9$ $cmHz^{1/2}W^{-1}$ with a maximum value $D^* = 1.8\ x10^9$ $cmHz^{1/2}W^{-1}$.

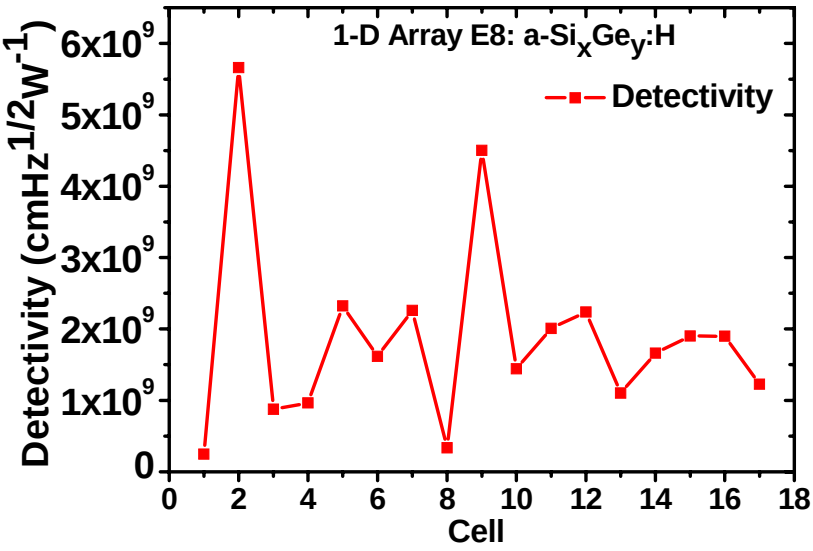

Figure 4.76. Detectivity values of the array E8 with an a-Si_xGe_y:H intrinsic film (process 443).

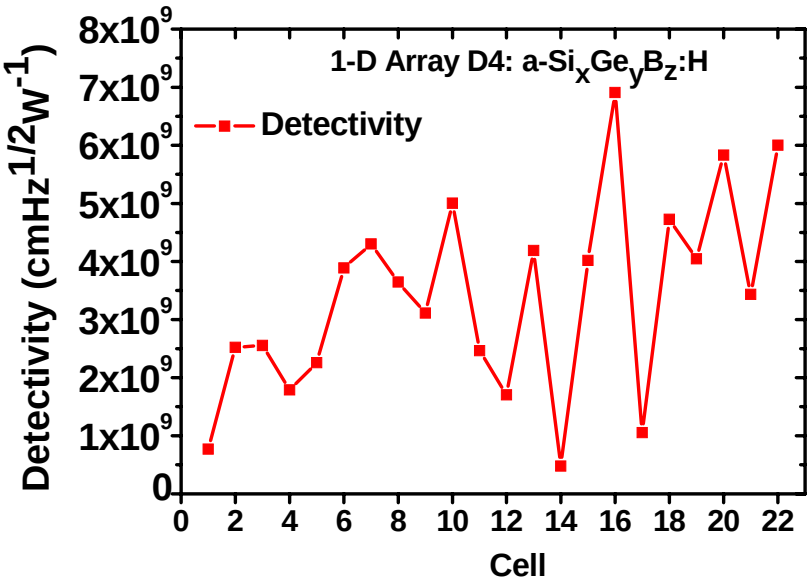

Figure 4.77. Detectivity values of the array D4 with an a-$Si_xGe_yB_z$:H film (process 479).

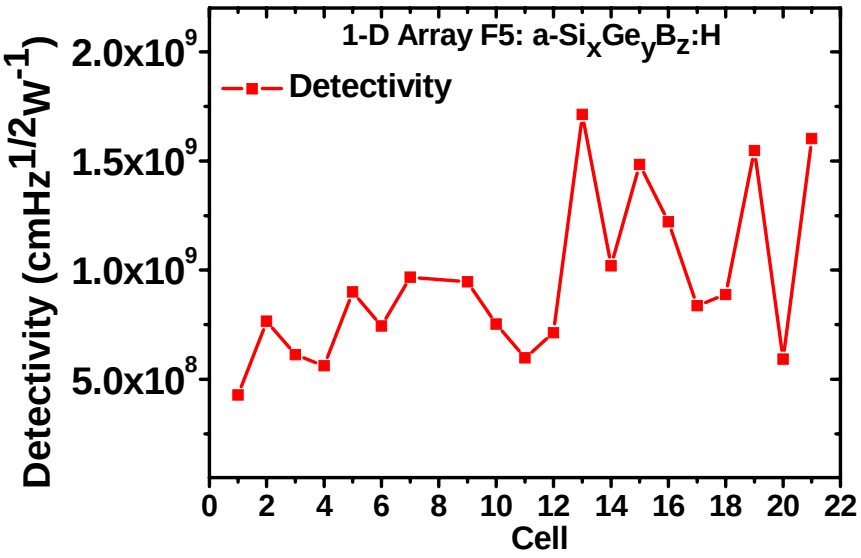

Figure 4.78. Detectivity values of the array F5 with an a-$Si_xGe_yB_z$:H film (process 480).

The array D4 of boron alloy micro-bolometers (process 479) showed the largest average detectivity.

4.9.4 Statistical analysis in responsivity values in micro-bolometer arrays.

In the previous section the subtraction $\Delta I = I_{IR} - I_{Dark}$, was performed individually in every micro-bolometer in the arrays. However it is attractive to obtain an average dark current, $\bar{I}_{Dark,}$ of the micro-bolometers in the array and subtract this value from the current under IR illumination, of each micro-bolometer $\Delta I = I_{IR} - \bar{I}_{Dark.}$

In order to study that algorithm, the dispersion in the current values of the micro-bolometers must to be small. Table 4.14 shows the results of a dispersion analysis in the three arrays studied in the previous section (section 4.9), where the subtraction $\Delta I = I_{IR} - I_{Dark}$ was made individually.

Standard deviation and relative scattering are included in Table 4.14, we can observe that the standard deviation is large and therefore the relative scattering in responsivity is very large, in the range of 0.39 - 0.69.

Table 4.14 Standard deviation and relative scattering in the cells of 3 arrays.

	Arrays		
Values	**E8-W1 a-Si_xGe_y:H**	**D4-W3 a-$Si_xGe_yB_z$:H**	**F5-W4 a-$Si_xGe_yB_z$:H**
Number of cells	17	22	20
$\overline{R}$ (mean responsivity)	2.8E-4	2.5E-2	4.17E-2
σ (Standard deviation)	1.95E-4	1.24E-2	1.63E-2
σ_m (Standard deviation / $\sqrt{N}$)	4.7E-5	2.6E-3	3.6E-3
δ (σ / $\overline{R}$ - relative scattering)	0.69	0.49	0.39

If Equation 4.4 is employed in order to remove bad cells (the cells that comply Equation 4.4 have large scattering), then Table 4.14 can be rewritten without bad cells. Table 4.15 shows those results, where the standard deviation and the relatively scattering have a small reduction, but still are very large.

$$\left|Ri - \overline{R}\right| > 2\sigma \qquad (4.4)$$

Table 4.15 Standard deviation and relative scattering in the cells of 3 arrays, when bad cells have been removed.

	Arrays		
Values	E8-W1 a-Si_xGe_y:H	D4-W3 a-$Si_xGe_yB_z$:H	F5-W4 a-$Si_xGe_yB_z$:H
Cells removed	2	1	1
Cells took into account	15	21	19
$\overline{R}$ (mean responsivity)	2.17E-4	2.38E-2	4E-2
σ (Standard deviation)	9.5E-5	1.13E-2	1.46E-2
σ_m (Standard deviation / $\sqrt{N}$)	2.45E-5	2.4E-3	3.3E-3
δ (σ / $\overline{R}$ - relative scattering)	0.43	0.47	0.36

If the previous analysis is repeated when an average dark current is subtracted to each micro-bolometer in the arrays, $\Delta I = I_{IR} - \bar{I}_{Dark}$. We obtained the results of Table 4.16, where the standard deviation and relative scattering have a significant increase. Table 4.17 shows the results where the bad cells are removed (bad cells are those that comply Equation 4.4), where it can be observed that the standard deviation and relative scattering have an increase from the results obtained in Table 4.16.

Table 4.16 Standard deviation and relative scattering in the cells of 3 arrays, when an average dark current is subtracted to the IR current in each micro-bolometer.

	Arrays		
Values	E8-W1 a-Si_xGe_y:H	D4-W3 a-$Si_xGe_yB_z$:H	F5-W4 a-$Si_xGe_yB_z$:H
Number of cells	17	22	20
$\lvert\bar{R}\rvert$ (mean responsivity)	2.34E-3	1.7E-1	2.45E-1
σ (Standard deviation)	2.03E-3	1.14E-1	1.46E-1
σ_m (Standard deviation / $\sqrt{N}$)	4.9E-4	2.4E-2	3.2E-2
δ (σ / $\bar{R}$ - relative scattering)	0.86	0.67	0.59

Table 4.17 Standard deviation and relative scattering, when an average dark current is subtracted to the IR current in each micro-bolometer and bad cells have been removed.

	Arrays		
Values	E8-W1 a-Si_xGe_y:H	D4-W3 a-$Si_xGe_yB_z$:H	F5-W4 a-$Si_xGe_yB_z$:H
Cells removed	2	1	1
Cells took into account	15	21	19
$\lvert\bar{R}\rvert$ (mean responsivity)	2.36E-3	1.59E-1	2.3E-1
σ (Standard deviation)	2.15E-3	1.04E-1	1.34E-1
σ_m (Standard deviation / $\sqrt{N}$)	5.5E-4	2.2E-2	3E-2
δ (σ / $\bar{R}$ - relative scattering)	0.91	0.65	0.58

From this analysis we can conclude that it is not suitable perform an algorithm in order to subtract an average dark current $\bar{I}_{Dark}$ to the IR current I_{IR} in every cell in the array, due to the high dispersion presented in the responsivity values of the micro-bolometers in the arrays.

4.9.5 Measurements of 1-D image employing with a micro-bolometer array

We selected the array F5 (process 479) for this characterization. The selection was made considering the large average current responsivity showed by this array.

We used a mask composed by an Al foil placed over a plastic lid. The mask was placed over the array covering half of the cells. I(U) measurements in the cells of the array were performed, in dark and under IR illumination, as was described in section 4.9.3.

Figures 4.79 and 4.80, show the increment in current form dark condition to IR radiation, $\Delta I = I_{IR} - I_{Dark}$, in the cells of array F5, for two voltage pulses U=5 V and U=9 V, respectively.

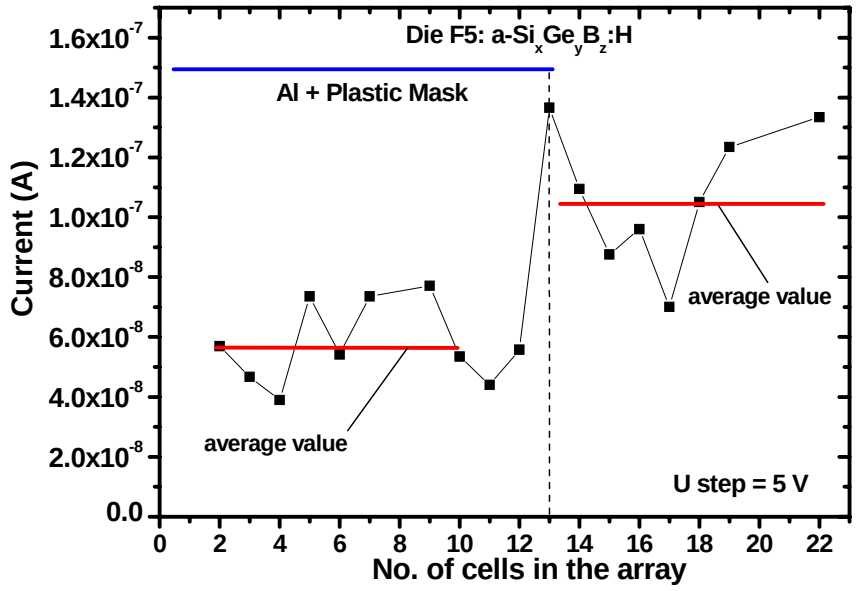

Figure 4.79. 1-D image obtained with the array F5 with an a-$Si_xGe_yB_z$:H film (process 480), for a voltage step U= 5V.

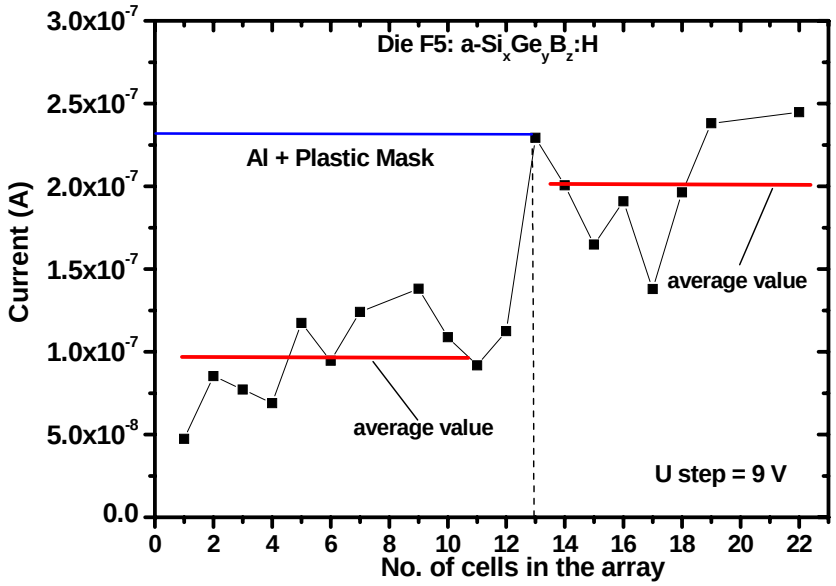

Figure 4.80. 1-D image obtained with the array F5 with an a-$Si_xGe_yB_z$:H film (process 480), for a voltage step U= 9V.

In Figures 4.79 and 4.80 we can observe that the cells covered by the mask, show a smaller current value than those which are not covered. For a voltage step U=5 V, the difference in current, form the uncovered part of the array and the covered part is around 5 x10^{-8} A, while for a step U= 9 V, the difference is around 1x10^{-7} A.

The cells which are covered by the mask show an increment in current ΔI, the reason is that the mask used is not a perfect IR mask, it reflects part of the IR radiation, but also absorbs part of it, which is absorbed by the micro-bolometers, which are covered.

4.9.6 Measurements of crosstalk in micro-bolometers

Crosstalk in micro-bolometer arrays could be of different nature, such as electrical, thermal and optical. In literature there is not too much information related to methods of characterization of crosstalk in micro-bolometer arrays. Employing the

experimental read-out circuit, we performed a characterization of electrical crosstalk in DC regime, in one micro-bolometer array.

We define the crosstalk in DC regime, as the voltage bias that cause heating in the neighbors cells of a cell biased, where heating due to biasing is presented. Optical, and thermal crosstalk, and crosstalk due to high frequency bias are not considered in this characterization. One cell (labeled central cell) was biased with different voltage bias values, U= 0.5, 1, 2,…18, and the current in its neighbors cells was monitored (a small voltage was applied U= 0.5 V in the neighbor cells), in order to observe any change in their currents due to the bias heating in the central cell. Table 4.18 shows the results of this characterization.

Table 4.18. Results of crosstalk characterization in DC regime in the micro-bolometers arrays

	Current (U=0.5 V)	
Voltage of central cell	left neighbor cell	rigth neighbor cell
(V)	(A)	(A)
0	$1.17x10^{-7}$	$8.25x10^{-8}$
0.5	$1.17x10^{-7}$	$8.26 x10^{-8}$
1	$1.17x10^{-7}$	$8.27 x10^{-8}$
2	$1.17x10^{-7}$	$8.27 x10^{-8}$
3	$1.17x10^{-7}$	$8.26 x10^{-8}$
4	$1.17x10^{-7}$	$8.26 x10^{-8}$
5	$1.17x10^{-7}$	$8.24 x10^{-8}$
6	$1.17x10^{-7}$	$8.26 x10^{-8}$
7	$1.17x10^{-7}$	$8.26 x10^{-8}$
8	$1.17x10^{-7}$	$8.26 x10^{-8}$
9	$1.17x10^{-7}$	$8.25 x10^{-8}$
10	$1.17x10^{-7}$	$8.26 x10^{-8}$
12	$1.17x10^{-7}$	$8.26 x10^{-8}$
15	$1.17x10^{-7}$	$8.26 x10^{-8}$
18	$1.18x10^{-7}$	$8.22 x10^{-8}$

In Table 4.18 we can observe that the value of current in the neighbor cells do not change due to the voltage applied to the central cell. That means that in DC regime, large voltage bias in the micro-bolometers do not affect the neighbor cells.

Characterization in 2-D arrays was not performed, since the experimental read-out circuit available is for 23 cells of 1-D arrays, however in 2-D arrays, the cell performance characteristics are expected similar than those observed in the 1-D arrays.

4.10 Conclusions.

The design of the process flow of a modified planar structure and sandwich structure micro-bolometers has been described. The results of characterization of intrinsic amorphous silicon-germanium a-Si_xGe_y:H and amorphous silicon-germanium-boron a-$Si_xGe_yB_z$:H films, which are employed as thermo-sensing films in un-cooled micro-bolometers, has been presented.

The fabrication of one dimensional (1-D) arrays of planar and sandwich structure micro-bolometers based on a-Si_xGe_y:H and a-$Si_xGe_yB_z$:H thermo-sensing films has been described, as well as the fabrication of two dimensional (2-D) arrays of planar structure micro-bolometers based on a-Si_xGe_y:H thermo-sensing film.

We also have characterized the different kind of single cell micro-bolometers: planar structure with both a-Si_xGe_y:H and a-$Si_xGe_yB_z$:H thermo-sensing films and the sandwich structure with a-Si_xGe_y:H thermo-sensing film. The performance characteristics as I(U) characteristics, Noise and Thermal time constant, have been measured in the devices in order to obtain the figures of merit as responsivity and detectivity. Finally was presented the characterization performed in the arrays employing an experimental read-out circuit, specific characteristics of an array were measured as crosstalk and the obtaining of a 1-D image.

4.11 References of chapter 4

[4.1] A Heredia-J, A Torres J, F. J. De la Hidalga – W, A Jaramillo-N, J Sanchez–M, C Zuñiga-I, M. Basurto P. and A Pérez, “Low Resistivity Boron Doped

Amorphous Silicon-Germanium Alloy Films Obtained with a Low Frequency Plasma", Mat. Res. Soc. Symp. Proc. 796 V2.4.1, 2004.

[4.2] V. L. Dalal "Growth Chemistry of Amorphous Silicon and Amorphous Silicon Germanium Alloys". Current Opinion in Solid State and Materials Science Vol. 6, p.p. 455-464, 2002.

[4.3] Tatsuo Shimizu, Optoelectronics Devices and technologies, Vol. 9, p.p. 277-298, 1994.

[4.4] B.D. Chapman and S. W. Han, G.T. Seidler, E. A. Stern, J. David Cohen, S. Guha, and J. Yang, "Short-range compositional randomness of hydrogenated amorphous silicon–germanium films", Journal of Applied Physics, Vol. 92, pp. 801 – 807, 2002.

[4.5] K. D. Mckenzie, J.R. Eggert, D.J. Leopold, Y.M. Li, S Lin, William Paul, Physical Review B, Vol. 31, pp. 2198-2212, 1985.

[4.6] Boris G. Budaguan, Alexei A. Sherchenkov, Grigory L. Gorbulin, "The properties of a-SiGe:H films deposited by 55kHz PECVD", Journal of Non-Crystalline Solids, Vol. 297, pp. 205-209, 2002.

[4.7] M.S. Abo Ghazala, "Composition and electronic properties of a-SiGe:H alloys produced from ultra thin layers of a-Si:H/a-Ge:H" Physica B, Vol. 293, pp. 132-136, 2000.

[4.8] C.C. Tsai, Physical Review B, Vol. 19, pp. 2044-2054, 1979.

CHAPTER 5. DISCUSSION

The results obtained from the study of fabrication and characterization of different micro-bolometer structures and micro-bolometer arrays, containing intrinsic a-Si_xGe_y:H films and boron alloys a-$Si_xGe_yB_z$:H, are discussed in the present chapter and compared with data reported in literature. The discussion of results has been divided in subsections according to the different achievements obtained in the present work.

A) Fabrication of planar structure micro-bolometer arrays and yield

At the present time, two main companies lead the development of micro-bolometer arrays based on amorphous silicon deposited by plasma, L-3 communications in US and LETI in France, as was discussed in chapter 2. They have reported arrays as large as 640 x 480 pixels, with a pixel size of 25 x 25 μm, based on planar structure micro-bolometers. ULIS has reported arrays with yield around 99%. However they do not report how yield was calculated, if it is an optical inspection or they are electrically tested, also they do not report the total yield in the wafer. L-3 communications do not report any information about yield of arrays.

The micro-bolometer arrays fabricated in the present work, contain 32 pixels (cells), with a pixel size of 70 x 66 μm, these arrays are significantly small in comparison with those available commercially, however the goal of this work is optimize the performance characteristics in the micro-bolometers and also establish the basis for the study and the development of un-cooled micro-bolometer arrays based on a-Si_xGe_y:H thin films.

The modifications performed in planar structure micro-bolometers resulted in wafer yields obtained by electrical characterization, in the range of 45 – 60%, and some arrays presented yields as large as 90%. This yield is larger than those obtained by optical inspection in the previous micro-bolometer structures fabricated at INAOE [1.12, 3,1], which presented a total wafer yield of 30%.

We found that the yield in the 1-D planar structure micro-bolometer arrays had a variation depending on the thermo-sensing film used; the intrinsic film micro-bolometers presented an average wafer yield of 45 % with some arrays with yields of 65%; while the boron alloy devices presented an average yield in the range of 50 – 60 %, whit some arrays with yield of 90%. The performance characteristics in those devices are discussed in the following sections.

There was performed a fabrication process of 2-D micro-bolometer arrays with intrinsic film, these arrays were not characterized, since our experimental read-out circuit works with linear arrays of 23 cells. However, the performance characteristics of the 2-D arrays are expected to be similar than those of the 1-D arrays.

From the above discussion, we can stress that the modifications made to layout and process flow of the planar structure micro-bolometers, have resulted in an increase of yield in comparison with the previous work.

B) Fabrication of sandwich structure micro-bolometer arrays and yield

In literature is reported just one work related to the fabrication of single cells sandwich structure micro-bolometers with a pixel size of 50 x 50 μm, based on a-$Ge_xSi_{1-x}O_y$ films deposited by sputtering on a metal membrane [2.20].

These devices are deposited over metal legs and no supporting film is employed, this cause stress problems in those devices and very low yield, however they do not perform a deep yield analysis. The thermo-sensing film employed is highly resistive and is deposited by sputtering, where no option for doping is possible.

In the present work sandwich structure micro-bolometer arrays based on intrinsic a-Si_xGe_y:H films has been studied: designed, fabricated and characterized. In these devices a SiN_x supporting film is employed, where the thermo-sensing film is sandwiched by Ti contacts.

The sandwich structure micro-bolometers arrays were tested electrically resulting in a low yield at the end of the fabrication process, which is around 10 %.

The problem of yield reduction is not related to stress, since the micro-bridges are not broken. The yield loss is due to short circuits between the metal contacts that sandwich the thermo-sensing film. Thus a better isolation between both electrodes is required. The performance characteristics are discussed in the following sections.

C) Thermo-sensing film characterization

In section 2.3 there were presented the most employed thermo-sensing films in micro-bolometers, Table 5.1 shows the most employed materials as thermo-sensing films in micro-bolometers.

Table 5.1 Most common thermo-sensing materials employed in micro-bolometers.

Material	TCR (K^{-1})	Ea (eV)	σ_{RT} $(\Omega\ cm)^{-1}$	Reference
VO_x	0.021	0.16	$2x10^{-1}$	[2.14-1.16]
a-Si:H (PECVD)	0.039	0.30	$\sim 1x10^{-9}$	[2.9,2.17]
a-Si:H,B (PECVD)	0.028	0.22	$5x10^{-3}$	[2.10]
a-SiGe:H (PECVD)*	0.043	0.34	$1.6x10^{-6}$	[2.17-2.18]
$Ge_xSi_{1-x}O_y$	0.042	0.32	$2.6x10^{-2}$	[2.19-2.21]

* INAOE, Mexico.

VO_x is one of the most employed materials [2.14-2.16], however this material is not compatible with Si CMOS standard technology and its TCR is not very large, around 0.021 K^{-1}.

Amorphous $Ge_xSi_{1-x}O_y$ films have been employed in sandwich structure micro-bolometers [2.19-2.21], these films are compatible with the CMOS technology and present a high TCR, around 0.042 K^{-1}; however it has a high resistance and is deposited by sputtering where doping is not possible to perform.

At the present time a-Si:H and boron doped a-Si:H are employed in large micro-bolometer arrays [2.10, 2.17-2,18]. Intrinsic a-Si:H is compatible with CMOS technology and has a high TCR, around 0.039 K^{-1}; however it is a highly resistive

material, resulting in high resistive micro-bolometers which present a mismatch impedance with the readout circuits. Boron doped a-Si:H, present moderated resistivity, but also a reduction in TCR, around 0.028 K^{-1}.

Therefore none of those materials can be considered the optimum one as thermo-sensing material in micro-bolometers. Intrinsic a-Si_xGe_y:H films presents a large TCR, around 0.043 K-^{1}, a moderated resistivivy and is compatible with the Si CMOS technology; those characteristics make this material suitable as thermo-sensing film for micro-bolometer arrays, however the resistivity is still high.

Amorphous silicon-germanium-boron alloys a-$Si_xGe_yB_z$:H, have been studied in this thesis work, in order to reduce the high resistivity presented in intrinsic films. From the conductivity characterization in the thermo-sensing films, we can state that the a-$Si_xGe_yB_z$:H alloys demonstrated an increment in their conductivity (between 2 and 3 orders of magnitude) in comparison of that of the intrinsic a-Si_xGe_y:H film. However the increment in σ was accompanied by a reduction in TCR, around 0.028 K^{-1}. The deposition rate in the boron alloys is around 2 -3 times larger than that of the intrinsic film. Thus B incorporation during the thermo-sensing deposition, enhance the deposition rate. The deposition of the thermo-sensing films over a SiN_x micro-bridge, has as consequence a reduction in the film conductivity, the stress arisen in the SiN_x micro-bridge could be the cause for the σ reduction.

The a-$Si_xGe_yB_z$:H films compared with the another thermo-sensing materials, have better performance characteristics, which are: compatibility with the Si CMOS technology, moderated values of TCR, comparables with those of the VO_x and a-Si:H films, and reduced resistivty. In general the a-$Si_xGe_yB_z$:H alloys have similar characteristics than those of the a-Si:H,B thermo-sensing film [2.10], but present one order of magnitude shorter values of resistivity.

D) Micro-bolometers characterization

Table 5.2 presents the main performance characteristics of the micro-bolometers reported in literature, which are compared with the different micro-

bolometer configurations studied in this work, containing intrinsic and boron alloys thermo-sensing films. Information related to the performance characteristics of micro-bolometers in literature is not completely open, most of the performance characteristics are not published.

Table 5.2. Comparison of characteristics of micro-bolometers with literature.

Thermo sensing layer	**E_a, eV**	**TCR,α K^{-1}**	**Cell area, A_{cell}, μm^2**	**Cell resistance, R_{cell}, Ohm**	**Voltage responsivity, R_U, VW^{-1}**	**Current responsivity, R_I, AW^{-1}**	**Thermal response time, ms.**	**Detecti vity, D* $cmHz^{1/2}W^{-1}$**	**References**
VO_X	0.16	0.021	50 x 50	-	2.5×10^7	-	-	-	Planar [2.14-2.15]
$Ge_xSi_{1-x}O_y$	0.32	0.042	50 x 50	$7x10^5$	$1x10^5$	-	13	$6.7x10^8$	Sandwich [2.20-2.21]
a-Si:H,B	0.22	0.028	48 x 48	$3 x10^7$	10^6	-	11	-	Planar [2.10]
a-Si:H	0.30	0.039	25 x 25	-	-	-	7	-	Planar [2.35-2.37]
$a\text{-}Si_xGe_y$:H Ge_y=0.5	0.34	0.043	70 x 66	$5x10^8$	$7.2x10^5$ *	$2x10^{-3}$	125	$7.9x10^9$	Planar [This work]
$a\text{-}Si_xGe_yB_z$:H Ge_y=0.45,B_z=0.09	0.21	0.027	70 x 66	$1x10^6$	$1.2x10^5$ *	$3x10^{-2}$	3	$5.9x10^9$	Planar [This work]
$a\text{-}Si_xGe_yB_z$:H Ge_y=0.55, B_z=0.07	0.20	0.028	70 x 66	$3x10^6$	$1.8x10^5$ *	$7x10^{-2}$	0.3	$2x10^9$	Planar [This work]
$a\text{-}Si_xGe_y$:H Ge_y=0.5	0.34	0.043	70 x 66	$1x10^5$	$2.2x10^5$ *	0.3 - 14	0.1	$4x10^9$	Sandwich [This work]

* Voltage responsivity R_U, was calculated from the current responsivity R_I.

Commercial planar structure micro-bolometers based on VO_x films [2.14-2.15], present moderated values of TCR, around α=0.021 K^{-1} and high values of

voltage responsivity, R_U=2.5x10^7 VW^{-1}. Another performance characteristics as detectivity, D^* and thermal response time, τ_{th}, are not published. The main drawback of these devices is their un-compatibility with Si CMOS technology, thus special installations are necessary for their fabrication, which make impossible to fabricate those devices in any standard Si CMOS fabrication line.

Commercial planar structure micro-bolometers based on resistive a-Si:H [2.35], present high values of TCR, around α=0.039 K^{-1}, however also present high values of resistance. The τ_{th} reported for those devices is around τ_{th} =7 ms.

Comercial a-Si:H,B based planar structure micro-bolometers [2.10] present moderated values of TCR, around α=0.28 K^{-1}, a cell resistance R_{cell} = 3x10^7 Ω, a relatively fast thermal response time , τ_{th}= 11 ms, and a high voltage responsivity, around R_U= 10^6 VW^{-1}. However values of D^* are not reported.

Sandwich structure micro-bolometers based on a-$Ge_xSi_{1-x}O_y$ [2.20-2.21] are not commercial and are studied as single cell, they have demonstrated high values of TCR, around α=0.042 K^{-1}, a moderated cell resistance, R_{cell} = 7x10^5 Ω, a moderated detectivity D^*=6.7 x10^8 cmHz$^{1/2}$W^{-1}, and a thermal response time in the range of τ_{th}= 13 ms. However the yield in those devices is very low. Deformation in the films occurs due to stress in the metal supporting structures employed.

In this work, the planar structure micro-bolometers based on intrinsic a-Si_xGe_y:H films have a very high value of TCR, around α=0.043 K^{-1}, a current responsivity, R_I=2x10^{-3} AW^{-1}, a very low current NSD, I_{noise} ≈ 1x10^{-15} AHz$^{-1/2}$, resulting in a very high detectivity D^*= 7.9x10^9 cmHz$^{1/2}$W^{-1}. However those devices present a very high cell resistance, R_{cell} = 5x10^8 Ω and a slow thermal response time, τ_{th}= 120 ms.

The boron alloy planar structure micro-bolometers have a cell resistance, around R_{cell} ≈ (1-3) x10^6 Ω, which is two orders of magnitude shorter than that of the planar structure devices with intrinsic film and one order of magnitude shorter than that of the a-Si:H,B commercial devices [2.10].

The current responsivity is around R_I= (3-7)x10^{-2} AW^{-1}, and the current NSD, I_{noise} ≈ 10^{-13} AHz$^{-1/2}$, which results in a high detectivity D^*= (2-6) x10^9 cmHz$^{1/2}$W^{-1}.

The thermal response time in those devices is fast, around τ_{th}= 0.3 - 3 ms, which is faster than those reported in literature.

The sandwich structure micro-bolometer with the intrinsic a-Si_xGe_y:H film, presents the shortest cell resistance of the devices reported in literature, $R_{cell} \approx 1 \times 10^5$ Ω, which is 3 orders of magnitude less than that of the planar devices with the same intrinsic film; one order of magnitude shorter than that of the boron alloy devices; 2 orders shorter than that of the a-Si:H,B [2.10] devices; and near to 1 order of magnitude shorter than that of the a-$Ge_xSi_{1-x}O_y$ [2.20-2.21] micro-bolometers.

The TCR in sandwich structures is very high, around α=0.043 K^{-1}, the current responsivity is in the range of R_I= (0.3 -14) AW^{-1}, which is around 2 - 3 orders of magnitude larger than that of the boron alloys a-$Si_xGe_yB_z$:H planar structure micro-bolometers and around 3 - 4 orders of magnitude larger than the intrinsic a-Si_xGe_y:H film planar structure devices. However the sandwich structure presents a larger current NSD, $I_{noise} \approx 10^{-11}$ $AHz^{-1/2}$, which results in a detectivity $D^*= 4 \times 10^9$ $cmHz^{1/2}W^{-1}$.

The thermal response time measured in the sandwich structure micro-bolometers is the shortest reported in literature, τ_{th}= 100 μs, which is near 2 orders of magnitude shorter than that reported for a-Si:H micro-bolometers [2.35 -2.37].

The response time obtained in the devices is not the RC constant, since this constant has been estimated for the devices.

The electrical time, τ_{elec}, is the product of the coaxial cable capacitance ($C_{cable} \approx$ 10 pF) used in the measurements, and the resistance of the micro-bolometer. The micro-bolometer with the intrinsic film, has cell resistance around $R_{cell} \approx$ 500 MΩ. Therefore $\tau_{elec} \approx$ 5 msec, which is 2 orders of magnitude smaller than the micro-bolometer thermal time, τ_{th}. In the case of sandwich configuration micro-bolometers with resistances around $R_{cell} \approx$ 100 KΩ, the electrical time should be approximately $\tau_{elec} \approx$ 1 μsec, 2 orders of magnitude less than the τ_{th}.

An explanation of the reason of the reduction of τ_{th} in the boron alloys micro-bolometers and in the sandwich devices, is not simple and it is not completely clear; however, we have found that the reduction of the τ_{th} is accompanied with an increase

in the device conductivity, an increase in noise, and a reduction in D^*. Thus there is a compromise between τ_{th} and D^* in the micro-bolometers.

In conclusion, the boron alloys planar structures micro-bolometers and specially the intrinsic film sandwich structure devices, have demonstrated better performance characteristics than those of the micro-bolometers reported in literature and available commercially.

E) Micro-bolometer arrays characterization

There are two main materials employed as thermo-sensing films in micro-bolometer arrays, VO_x, [2.14-2.15] and resistive a-Si:H [2.35 – 2.37] or boron doped a-Si:H (a-Si:H,B) [2.10].

The arrays available commercially [2.10, 2.14-2.15, 2.35-2.37], contain a large number of micro-bolometers cells, around 320 x 240 and 640 x 480 cells. The performance characteristics of the micro-bolometers in these arrays are the same than those described in the previous section, for single cell micro-bolometers in Table 5.2.

The modifications made in the micro-bolometer configurations, have gave as a result a significantly increase in the yield of the arrays.

A 1-D image was obtained with the arrays, however the cells in the arrays have non uniformity in their characteristics. The reason of non uniformity in the performance characteristics of the cells of the arrays is not completely clear at the moment. Stress in the SiN_x micro-bridges and therefore in the thermo-sensing films can be the cause of such non uniformities in the electrical properties of the devices.

The arrays studied in this work are small in comparison with those available commercially, however the a-$Si_xGe_yB_z$:H alloys thermo-sensing film micro-bolometer arrays, have demonstrated better performance characteristics than those of the commercial arrays, which are, fast response time τ_{th}, high detectivity, D* and low cell resistance, R_{cell}. These characteristics make boron alloys micro-bolometers suitable for high performance and large micro-bolometer arrays.

CHAPTER 6. CONCLUSIONS

This chapter presents the main conclusions formulated from the analysis of the experimental work performed in this thesis work, which consisted in the study of silicon-germanium-boron thermo-sensing films, the study of the design and fabrication of different structures of micro-bolometers and micro-bolometer arrays.

A) Analysis of the fabrication process of micro-bolometers and arrays

- The modifications proposed and realized in the design and fabrication of single cell micro-bolometers, such as the improvement of dry etching, the use of different metals for the devices, allowing the etching of the Al sacrificial layer at the end of the process flow; resulted in micro-bolometer arrays with yields as large as 90 %. In literature there is no clear information about yield measurements in large IR arrays.
- For first time a sandwich structure micro-bolometer based on silicon – germanium films has been studied: designed, fabricated and characterized. The only sandwich structure micro-bolometer reported in literature [2.20] is based on $Ge_xSi_{1-x}O_y$ films deposited by sputtering over a metal membrane, with very low yield.
- For first time silicon-germanium-boron alloys, a-$Si_xGe_yB_z$:H, have been studied as thermo-sensing films for un-cooled micro-bolometers, resulting in better performance characteristics of the devices, than those reported for the commercially available micro-bolometers.

B) Thermo-sensing film characterization

- The a-$Si_xGe_yB_z$:H films studied in the present work in comparison with the thermo-sensing materials reported in literature, demonstrate better

performance characteristics, which are: moderated values of TCR, reduced resistivity and compatibility with the Si CMOS technology.

- The incorporation of B in the thermo-sensing films, has resulted in an increase on the yield of the devices, suggesting that the B incorporation in the films, make them more resistant to the etching steps during the fabrication process and also more resistant to stress.
- From SIMS we found the solid composition in the thermo-sensing films. We observed a significant increase in the B_z and Ge_y solid content from the gas content, suggesting strong preferential B and Ge incorporation from gas phase. Also the B incorporation in the thermo-sensing films, results in a significantly increase of the deposition rate (around 3 times), in comparison of that of the intrinsic films.
- In general the a-$Si_xGe_yB_z$:H alloys have similar characteristics to those of the a-Si:H,B thermo-sensing film, which is widely used in commercial un-cooled micro-bolometers arrays [2.10], but show one order of magnitude lower values of resistivity, than that of the a-Si:H,B films.

C) Micro-bolometers characterization

- The micro-bolometers with boron alloys as thermo-sensing films have been found to demonstrate superior performance characteristics: large current responsivity, $R_I = 7x10^{-2}$ AW^{-1}, low cell resistance, $R_{cell} \approx 1x10^6$ ohms, and fast thermal response time, τ_{th} = 0.3 – 3 ms, which are better than those observed in the intrinsic film devices and those reported in literature [2.10, 2.14-2.15, 2.35-2.37].
- The sandwich structure micro-bolometer has even a lower cell resistance, by about 1 - 2 orders of magnitude shorter than those of the boron alloy and the commercially available micro-bolometers; without a decrement in the E_a and TCR.

- The problem of impedance mismatching with the readout circuit, presented in intrinsic high resistance micro-bolometers is avoided in both, the boron alloys planar structure and the intrinsic film sandwich structure micro-bolometers.
- For first time a thermal response time in the range of 100 μs has been demonstrated by a micro-bolometer (sandwich structure).
- Systematically study of noise and responsivity has been performed in all the samples fabricated. It has been shown that the sandwich micro-bolometer has the largest current responsivity of the devices studied, around 2 - 3 orders of magnitude larger than those of the planar intrinsic film micro-bolometers and the planar boron alloys devices, respectively. However it has also the largest current NSD, resulting in a detectivity very similar than those of the intrinsic film and boron alloys devices.
- The sandwich structure micro-bolometer has been found to possess two main advantages, a fast thermal response time and a reduced cell resistance, without a reduction on their high TCR. This structure potentially is very promising for large arrays.

D) Micro-bolometer arrays characterization

- There were fabricated 4 different processes of micro-bolometer arrays, in four different wafers, and the yield was systematically studied in these wafers. The total yield of the wafers was in the range of 45 – 60 %, which are larger than that obtained in the previous planar micro-bolometers, which resulted in a wafer yield of 30 %.
- An experimental external readout circuit has been proposed and used for the arrays characterization. Specific arrays characteristics have been measured. 1-D images have been obtained, and the electrical crosstalk in DC regime was not observed in the arrays.
- Non uniformity in the performance characteristics of the cells of the arrays is not completely clear. Stress in the SiN_x micro-bridges and therefore in the

thermo-sensing films can be the cause of such non uniformities in the electrical properties of the devices.

- In comparison with literature [2.10, 2.14-2.15, 2.35-2.37], the boron alloys thermo-sensing film micro-bolometers arrays, have in general better performance characteristics, which are, fast response time, $\tau_{th} \approx 0.3 - 3$ ms, high detectivity, $D^* \approx (2\text{-}6)\ x10^9 \pm 3x10^8$, low cell resistance, $R_{cell} \approx (3\text{-}8)x10^6$ ohms. And as well as sandwich structure micro-bolometer, they can be employed in large micro-bolometer arrays.

LIST OF PUBLICATIONS

International Journals

[1] M. Moreno, A. Kosarev, A. Torres, R. Ambrosio "Fabrication and Performance Comparison of Planar and Sandwich Structures of Micro-bolometers with Ge Thermo-sensing layer". Thin solid films, Vol. 515, pp. 7607-7610, 2007.

[2] M. Moreno, A. Kosarev, A. Torres, R. Ambrosio "Comparison of Three Un-Cooled Micro-Bolometers Configurations Based on Amorphous Silicon-Germanium Thin Films Deposited by Plasma", J. Non Crystaline Solids, 2007 (Accepted for impression).

[3] M. Moreno, A. Kosarev, A. Torres, I. Juarez, "Arrays of Un-cooled Micro-bolometers Based on Amorhous Silicon-Germanium Thin Films Deposited by Plasma", J. Non Crystaline Solids, 2007 (Accepted for impression).

[4] A. Kosarev, M. Moreno, A. Torres, C. Zuniga "IR sensors based on silicon-germanium-boron alloys deposited by plasma: fabrication and characterization", J. Non Crystaline Solids, 2007 (Accepted for impression).

[5] A. Torres, M. Moreno, A. Kosarev, A. Heredia, "Thermo-sensing Germanium-Boron-Silicon Films Prepared by Plasma for Un-cooled Micro-bolometers ", J. Non Crystaline Solids, 2007 (Accepted for impression).

National Journals

[6] M. Moreno, A. Kosarev, A. Torres, "Fabrication and Characterization of Un-cooled Micro-bolometers Based on Germanium Thin Films obtained By Low frequency Plasma Deposition" Revista Mexicana de Física, RMF, (In press).

International proceedings

[7] Mario Moreno, Andrey Kosarev, Alfonso Torres, Roberto Ambrosio: "Study of a Fabrication Process and Characterization of One Dimensional Array of Un-cooled Micro-bolometers Based on Germanium Films Deposited by Plasma", in Amorphous and Polycrystalline Thin-Film Silicon Science and Technology—2007, edited by V. Chu, S. Miyazaki, A. Nathan, J. Yang, H.W. Zan (Mater. Res. Soc. Symp. Proc. Volume 989, Warrendale, PA, 2007), 0989-A19-01.

[8] A. Kosarev, M. Moreno, A. Torres, R. Ambrosio, "Un-cooled micro-bolometer with Sandwiched Thermo-sensing Layer Based on Ge films deposited by Plasma", in Amorphous and Polycrystalline Thin-Film Silicon Science and Technology--2006, edited by H.A. Atwater, Jr., V. Chu, S. Wagner, K. Yamamoto, H-W. Zan (Mater. Res. Soc. Symp. Proc. 910, Warrendale, PA, 2006),A17-05.

LIST OF CONFERENCES

International Conferences

[1] M.Moreno, A.Kosarev, A.Torres, R. Ambrosio, "Comparison of Three Un-Cooled Micro-Bolometers Configurations Based on Amorphous Germanium Thin Films Deposited by Plasma", ICANS 22, in Colorado, USA, 19-24 August, 2007.

[2] M.Moreno, A.Kosarev, A.Torres, I. Juarez, "Arrays of Un-cooled Micro-bolometers Based on Amorhous Germanium Thin Films Deposited by Plasma", ICANS 22, in Colorado, USA, 19-24 August, 2007.

[3] A.Torres, M.Moreno, A.Kosarev, A. Heredia, "Thermo-sensing Silicon-Germanium-Boron Films Prepared by Plasma for Un-cooled Micro-bolometers", ICANS 22, in Colorado, USA, 19-24 August, 2007.

[4] A. Kosarev, M. Moreno, A. Torres, C. Zuniga, "IR sensors Based on Germanium-Boron-Silicon Alloys deposited by Plasma: Fabrication and Characterization", ICANS 22, in Colorado, USA, 19-24 August, 2007.

[5] M.Moreno, A.Kosarev, A.Torres, R. Ambrosio, "Study of a Fabrication Process and Characterization of One Dimensional Array of Un-cooled Micro-bolometers Based on Germanium films deposited by Plasma", Materials research society MRS, in San Francisco CA, USA, April 2007.

[6] A.Kosarev, M.Moreno, A.Torres, R. Ambrosio, "Un-cooled Micro-bolometer with Sandwiched Thermo-sensing Layer Based on Ge films deposited by Plasma", Materials research society MRS, in San Francisco CA, USA, April 2006.

[7] M.Moreno, A.Kosarev, A.Torres, R. Ambrosio, "Fabrication and Performance Comparison of Planar and Sandwich Structures of Micro-bolometers with Ge Thermo-sensing layer". European Material Research Society (EMRS), Nice France, may 29 - june 2, 2006.

[8] R. Ambrosio, A. Heredia, A. Torres, J. Hidalga, A. Kosarev, P. Rosales, M. Moreno, "Amorphous silicon and its alloys obtained by PECVD as sensing elements for IR sensors". ICANS 21, Lisbon Portugal, September 04-09, 2005.

[9] M.Moreno, A.Kosarev, A.Torres, "Fabrication and Characterization of un-cooled micro-bolometers based on germanium thin films obtained by low frequency plasma deposition". XVIII Latin American symposium in solid state physics, SLAFES, in Puebla, Mexico, November 2006.

National Conferences

[10] M.Moreno, A.Kosarev, A.Torres, R. Ambrosio, "Development of a fabrication process of thin film uncooled Infrared Imaging Arrays". In the congress of Sociedad Mexicana de Ciencias de Superficie y Materiales, Playa del Carmen Quintana Roo, Mexico, September 07 – 11, 2004.

[11] M.Moreno, A.Kosarev, A.Torres, R. Ambrosio, " Fabrication Process of 1-D arrays of thin film un-cooled micro-bolometers". In the congress of Sociedad Mexicana de Ciencias de Superficie y Materiales Zacatecas, Mexico, September 26 – 30, 2005.

[12] M. Moreno, A. Kosarev, A.Torres, R. Ambrosio, "Fabrication and Characterization of 1-D Arrays of uncooled micro-bolometers based on a-$Si_xGe_yB_z$:H films", Oaxaca, Oax., Mexico, September 24 - 28, 2007.

LIST OF PROJECTS

CONACyT Project No. D48454-F

Investigation of silicon and germanium semiconductor alloys obtained by plasma, and new structures for uncooled microbolometers, with implementation and development of advanced analytical methods based on SIMS.

CONACyT Project No. U 42367 - K

Thin Film nanomaterials based on silicon and germanium: Fabrication, characterization and applications.

LIST OF FIGURES